nature methods

Focus on fluorescence imaging

Principles and practice of microscope techniques

Central brain hemisphere and eye-antenna disc of *Drosophila melanogaster* at the third larval stage stained with three Alexa dyes and imaged on a Zeiss LSM 510 Meta. Image courtesy of Veta Trunova, The Johns Hopkins University.

Fluorescent proteins. Image courtesy of Roger Tsien, University of California at San Diego.

When Sir George Gabriel Stokes first described the phenomenon of fluorescence in 1852 it is doubtful many people ever considered its potential as a tool for biologists. As often happens with new discoveries, however, scientists figured out a way to exploit this physical process and began to use fluorescent molecules as biological labels. In concert with microscopy this permitted previously undreamt-of possibilities for detection and visualization.

Notably, immunofluorescence techniques became powerful tools for inquisitive biologists. Recently, the description of new imaging modalities such as confocal and two-photon microscopy, the creation of new fluorescent molecules, and the discovery and exploitation of fluorescent proteins have triggered an explosion in fluorescence microscopy techniques. This has also resulted in their use within living systems where they are revolutionizing biological imaging. A sampling of seminal papers documenting this advance is available in the 'Classics Library' on the Focus website.

The application of fluorescence techniques to living specimens presents many challenges to users. There is thus a greater need for users to understand the principles of fluorescence and how different imaging systems work so biologists can fully exploit this revolution. Determining the most suitable equipment and reagents for an application, and properly designing and conducting experiments both require a clear understanding of the basic principles involved. This Focus is intended to present this basic information as well as practical advice that biologists need to use these powerful techniques in their work.

We are pleased to acknowledge the support of Carl Zeiss Microscopy as principal sponsor and Intelligent Imaging Innovations, Inc. as supporting sponsor in producing this focus. As always, *Nature Methods* carries sole responsibility for all editorial content and peer review.

Daniel Evanko

CONTENTS

COMMENTARY

902 Fluorescence microscopy today
Rafael Yuste

PERSPECTIVE

905 A guide to choosing fluorescent proteins
Nathan Shaner, Paul Steinbach & Roger Tsien

REVIEWS

910 Fluorescence microscopy
Jeff Lichtman & José-Angel Conchello

920 Optical sectioning microscopy
José-Angel Conchello & Jeff Lichtman

932 Deep tissue two-photon microscopy
Fritjof Helmchen & Winfried Denk

941 Fiber-optic fluorescence imaging
Benjamin Flusberg, Eric Cocker, Wibool Piyawattanametha, Juergen Jung, Eunice Cheung & Mark Schnitzer

A guide to choosing fluorescent proteins

Nathan C Shaner[1,2], Paul A Steinbach[1,3] & Roger Y Tsien[1,3,4]

The recent explosion in the diversity of available fluorescent proteins (FPs)[1–16] promises a wide variety of new tools for biological imaging. With no unified standard for assessing these tools, however, a researcher is faced with difficult questions. Which FPs are best for general use? Which are the brightest? What additional factors determine which are best for a given experiment? Although in many cases, a trial-and-error approach may still be necessary in determining the answers to these questions, a unified characterization of the best available FPs provides a useful guide in narrowing down the options.

We can begin by stating several general requirements for the successful use of an FP in an imaging experiment. First, the FP should express efficiently and without toxicity in the chosen system, and it should be bright enough to provide sufficient signal above autofluorescence to be reliably detected and imaged. Second, the FP should have sufficient photostability to be imaged for the duration of the experiment. Third, if the FP is to be expressed as a fusion to another protein of interest, then the FP should not oligomerize. Fourth, the FP should be insensitive to environmental effects that could confound quantitative interpretation of experimental results. Finally, in multiple-labeling experiments, the set of FPs used should have minimal crosstalk in their excitation and emission channels. For more complex imaging experiments, such as those using fluorescence resonance energy transfer (FRET)[17] or selective optical labeling using photoconvertible FPs[12,15], additional considerations come into play. General recommendations to help determine the optimal set of FPs in each spectral class for a given experiment are available in Box 1, along with more detail on each issue discussed below.

'Brightness' and expression

FP vendors typically make optimistic but vague claims as to the brightness of the proteins they promote. Purely qualitative brightness comparisons that do not provide clear information on the extinction coefficient and quantum yield should be viewed with skepticism. For example, the newly released DsRed-Monomer (Clontech) is described as "bright," even though in fact, it is the dimmest monomeric red fluorescent protein (RFP) presently available.

The perceived brightness of an FP is determined by several highly variable factors, including the intrinsic brightness of the protein (determined by its maturation speed and efficiency, extinction coefficient, quantum yield and, in longer experiments, photostability), the optical properties of the imaging setup (illumination wavelength and intensity, spectra of filters and dichroic mirrors), and camera or human eye sensitivity to the emission spectrum. Although these factors make it impossible to name any one FP as the brightest overall, it is possible to identify the brightest protein in each spectral class (when more than one protein is available), as this depends only on the intrinsic optical properties of the FP. The brightest proteins for each class are listed in Table 1, with greater detail on the properties of each listed protein available in Supplementary Table 1 online. As discussed below in relation to photostability, the choice of optimal filter sets is critical to obtaining the best performance from an FP.

Generally, FPs that have been optimized for mammalian cells will express well at 37 °C, but some proteins may fold more or less efficiently. We have not done extensive tests in mammalian cells to determine relative efficiency of folding and maturation at 37 °C versus lower temperatures, but expression of proteins in

[1]Department of Pharmacology, [2]Biomedical Sciences Graduate Program, [3]Howard Hughes Medical Institute and [4]Department of Chemistry and Biochemistry, 310 Cellular & Molecular Medicine West 0647, University of California at San Diego, 9500 Gilman Drive, La Jolla, CA 92093, USA. Correspondence should be addressed to R.Y.T. (rtsien@ucsd.edu).

PUBLISHED ONLINE 18 NOVEMBER 2005; DOI:10.1038/NMETH819

bacteria at 37 °C versus 25 °C gives some indication of the relative efficiencies. These experiments suggest that there are several proteins that do not mature well at 37 °C. Indications of potential folding inefficiency at 37 °C should not be taken with absolute certainty, however, as additional chaperones and other differences between mammalian cells and bacteria (and even variations between mammalian cell lines) could have substantial influences on folding and maturation efficiency.

Generally, modern *Aequorea*-derived fluorescent proteins (AFPs, see **Supplementary Table 2** online for mutations of common AFP variants relative to wild-type GFP) fold reasonably well at 37 °C—in fact, several recent variants have been specifically optimized for 37 °C expression. The UV-excitable variant T-Sapphire[6] and the yellow AFP (YFP) variant Venus[1] are examples of these. The best green GFP variant, Emerald[18], also folds very efficiently at 37 °C compared with its predecessor, enhanced GFP (EGFP). The only recently developed AFP that performed poorly in our tests was the cyan variant, CyPet[2], which folded well at room temperature but poorly at 37 °C. All orange, red and far-red FPs (with the exception of J-Red and DsRed-Monomer) listed in Table 1 perform well at 37 °C.

An additional factor affecting the maturation of FPs expressed in living organisms is the presence or absence of molecular oxygen. The requirement for O_2 to dehydrogenate amino acids during chromophore formation has two important consequences. First, each molecule of AFP should generate one molecule of H_2O_2 as part of its maturation process[18], and the longer-wavelength FPs from corals probably generate two[19]. Second, fluorescence formation is prevented by rigorously anoxic conditions (< 0.75 μM O_2), but is readily detected at 3 μM O_2 (ref. 20). Even when anoxia initially prevents fluorophore maturation, fluorescence measurements are usually done after the samples have been exposed to air[21].

Photostability

All FPs eventually photobleach upon extended excitation, though at a much lower rate than many small-molecule dyes (Table 1). In addition, there is substantial variation in the rate of photobleaching between different FPs—even between FPs with otherwise very similar optical properties. For experiments requiring a limited number of images (around 10 or fewer), photostability is generally not a major factor, but choosing the most photostable protein is critical to success in experiments requiring large numbers of images of the same cell or field.

A unified characterization of FP photostability has until now been lacking in the scientific literature. Although many descriptions of new FP variants include some characterization of their photostability, the methods used for this characterization are highly variable and the resulting data are impossible to compare directly. Because many FPs have complex photobleaching curves and require different excitation intensities and exposure times, a standardized treatment of photostability must take all these factors into account.

To provide a basis for comparing the practical photostability of FPs, we have measured photobleaching curves for all of the FPs listed in Table 1 under conditions designed to effectively simulate widefield microscopy of live cells[4]. Briefly, aqueous droplets of purified FPs (at pH 7) were formed under mineral oil in a chamber that allows imaging on a fluorescence microscope. Droplets of volumes comparable to those of typical mammalian cells were photobleached with continuous illumination while recording images periodically to generate a bleaching curve. To account for differences in brightness between proteins and efficiency of excitation in our microscope setup, we normalized each bleaching curve to account for the extinction coefficient and quantum yield of the FP, the emission spectrum of the arc lamp used for excitation, and the transmission spectra of the filters and other optical path components of the microscope

BOX 1 RECOMMENDATIONS BY SPECTRAL CLASS

Far-red. mPlum is the only reasonably bright and photostable far-red monomer available. Although it is not as bright as many shorter-wavelength options, it should be used when spectral separation from other FPs is critical, and it may give some advantage when imaging thicker tissues. AQ143, a mutated anemone chromoprotein, has comparable brightness ($\varepsilon = 90\ (mM \cdot cm)^{-1}$, quantum yield (QY) = 0.04) and even longer wavelengths (excitation, 595 nm; emission, 655 nm), but it is still tetrameric[31].

Red. mCherry is the best general-purpose red monomer owing to its superior photostability. Its predecessor mRFP1 is now obsolete. The tandem dimer tdTomato is equally photostable but twice the molecular weight of mCherry, and may be used when fusion tag size does not interfere with protein function. mStrawberry is the brightest red monomer, but it is less photostable than mCherry, and should be avoided when photostability is critical. We do not recommend using J-Red and DsRed-Monomer.

Orange. mOrange is the brightest orange monomer, but should not be used when photostability is critical or when it is targeted to regions of low or unstable pH. mKO is extremely photostable and should be used for long-term or intensive imaging experiments or when targeting to an acidic or pH-unstable environment.

Yellow-green. The widely used variant EYFP is obsolete and inferior to mCitrine, Venus and YPet. Each of these should perform well in most applications. YPet should be used in conjunction with the CFP variant CyPet for FRET applications.

Green. Although it has a more pronounced fast bleaching component than the common variant EGFP, the newer variant Emerald exhibits far more efficient folding at 37 °C and will generally perform much better than EGFP.

Cyan. Cerulean is the brightest CFP variant and folds most efficiently at 37 °C, and thus, it is probably the best general-purpose CFP. Its photostability under arc-lamp illumination, however, is much lower than that of other CFP variants. CyPet appears superior to mCFP in that it has a somewhat more blue-shifted and narrower emission peak, and displays efficient FRET with YFP variant YPet, but it expresses relatively poorly at 37 °C.

UV-excitable green. T-Sapphire is potentially useful as a FRET donor to orange or red monomers.

(see[4] and Supplementary Discussion online for additional description of bleaching calculations). This method of normalization provides a practical measurement of how long each FP will take to lose 50% of an initial emission rate of 1,000 photons/s. Because dimmer proteins will require either higher excitation power or longer exposures, we believe this method of normalization provides a realistic picture of how different FPs will perform in an actual experiment imaging populations of FP molecules. Bleaching experiments were performed in parallel for several (but not all) of the FPs listed in Table 1 expressed in live cells and gave time courses closely matching those of purified proteins in microdroplets.

Based on our photobleaching assay results, it is clear that photostability can be highly variable between different FPs, even those of the same spectral class. Taking into account brightness and folding efficiencies at 37 °C, the best proteins for long-term imaging are the monomers mCherry and mKO. The red tandem dimer tdTomato is also highly photostable and may be used when the size of the fusion tag is not of great concern. The relative photostability of proteins in each spectral class is indicated in Table 1. Some AFPs, such as Cerulean, had illumination intensity–dependent fast bleaching components, and so photobleaching curves were taken at lower illumination intensities where this effect was less pronounced. The GFP variant Emerald displayed a very fast initial bleaching component that led to an extremely short time to 50% bleach. But after this initial fast bleaching phase, its photostability decayed at a rate very similar to that of EGFP. All YFPs, with the exception of Venus, have reasonably good photostability, and thus, YFP selection should be guided by brightness, environmental sensitivity or FRET performance (see Box 1 for greater detail and for general recommendations for all spectral classes, and Supplementary Fig. 1 online for sample bleaching curves).

Our method of measuring photobleaching has some limitations in its applicability to different imaging modalities, such as laser scanning confocal microscopy. Although we believe that our measurements are valid for excitation light intensities typical of standard epifluorescence microscopes with arc lamp illumination (up to 10 W/cm^2), higher intensity (for example, laser) illumination (typically >>100 W/cm^2) evokes nonlinear effects that we cannot predict with our assay. For example, we have preliminary indications that even though the first monomeric red FP, mRFP1, shows approximately tenfold faster photobleaching than the second-generation monomer mCherry, both appear to have similar bleaching times when excited at 568 nm on a laser scanning confocal microscope. The CFP variant Cerulean appears more photostable than ECFP with laser illumination on a confocal microscope[3] but appears less photostable than ECFP with arc lamp illumination. Such inconsistencies between bleaching behavior at moderate versus very high excitation intensities are likely to occur with many FPs. Single-molecule measurements will be even less predictable based on our population measurements, because our extinction coefficients are averages that include poorly folded or nonfluorescent molecules, whereas single-molecule observations exclude such defective molecules.

It is critical to choose filter sets wisely for experiments that require long-term or intensive imaging. Choosing suboptimal filter sets will lead to markedly reduced apparent photostability owing to the need to use longer exposure times or greater illumination intensities to obtain sufficient emission intensity.

Table 1 | Properties of the best FP variants[a,b]

Class	Protein	Source laboratory (references)	Excitation[c] (nm)	Emission[d] (nm)	Brightness[e]	Photostability[f]	pKa	Oligomerization
Far-red	mPlum[g]	Tsien (5)	590	649	4.1	53	<4.5	Monomer
Red	mCherry[g]	Tsien (4)	587	610	16	96	<4.5	Monomer
	tdTomato[g]	Tsien (4)	554	581	95	98	4.7	Tandem dimer
	mStrawberry[g]	Tsien (4)	574	596	26	15	<4.5	Monomer
	J-Red[h]	Evrogen	584	610	8.8*	13	5.0	Dimer
	DsRed-monomer[h]	Clontech	556	586	3.5	16	4.5	Monomer
Orange	mOrange[g]	Tsien (4)	548	562	49	9.0	6.5	Monomer
	mKO	MBL Intl. (10)	548	559	31*	122	5.0	Monomer
Yellow-green	mCitrine[i]	Tsien (16,23)	516	529	59	49	5.7	Monomer
	Venus	Miyawaki (1)	515	528	53*	15	6.0	Weak dimer[j]
	YPet[g]	Daugherty (2)	517	530	80*	49	5.6	Weak dimer[j]
	EYFP	Invitrogen (18)	514	527	51	60	6.9	Weak dimer[j]
Green	Emerald[g]	Invitrogen (18)	487	509	39	0.69[k]	6.0	Weak dimer[j]
	EGFP	Clontech[l]	488	507	34	174	6.0	Weak dimer[j]
Cyan	CyPet	Daugherty (2)	435	477	18*	59	5.0	Weak dimer[j]
	mCFPm[m]	Tsien (23)	433	475	13	64	4.7	Monomer
	Cerulean[g]	Piston (3)	433	475	27*	36	4.7	Weak dimer[j]
UV-excitable green	T-Sapphire[g]	Griesbeck (6)	399	511	26*	25	4.9	Weak dimer[j]

[a]An expanded version of this table, including a list of other commercially available FPs, is available as **Supplementary Table 1**. [b]The mutations of all common AFPs relative to the wild-type protein are available in **Supplementary Table 3**. [c]Major excitation peak. [d]Major emission peak. [e]Product of extinction coefficient and quantum yield at pH 7.4 measured or confirmed (indicated by *) in our laboratory under ideal maturation conditions, in (mM • cm)–1 (for comparison, free fluorescein at pH 7.4 has a brightness of about 69 (mM • cm)–1). [f]Time for bleaching from an initial emission rate of 1,000 photons/s down to 500 photons/s ($t_{1/2}$; for comparison, fluorescein at pH 8.4 has $t_{1/2}$ of 5.2 s); data are not indicative of photostability under focused laser illumination. [g]Brightest in spectral class. [h]Not recommended (dim with poor folding at 37 °C). [i]Citrine YFP with A206K mutation; spectroscopic properties equivalent to Citrine. [j]Can be made monomeric with A206K mutation. [k]Emerald has a pronounced fast bleaching component that leads to a very short time to 50% bleach. Its photostability after the initial few seconds, however, is comparable to that of EGFP. [l]Formerly sold by Clontech, no longer commercially available. [m]ECFP with A206K mutation; spectroscopic properties equivalent to ECFP.

Oligomerization and toxicity

Unlike weakly dimeric AFPs, most newly discovered wild-type FPs are tightly dimeric or tetrameric[7,9–12,14,22]. Many of these wild-type proteins, however, can be engineered into monomers or tandem dimers (functionally monomeric though twice the molecular weight), which can then undergo further optimization[4,10,12,17]. Thus, even though oligomerization caused substantial trouble in the earlier days of red fluorescent proteins (RFPs), there are now highly optimized monomers or tandem dimers available in every spectral class. Although most AFPs are in fact very weak dimers, they can be made truly monomeric simply by introducing the mutation A206K, generally without deleterious effects[23]. Thus, any of the recommended proteins in Table 1 should be capable of performing well in any application requiring a monomeric fusion tag. Researchers should remain vigiliant of this issue, however, and always verify the oligomerization status of any new or 'improved' FPs that are released. Lack of visible precipitates does not rule out oligomerization at the molecular level.

It is rare for FPs to have obvious toxic effects in most cells in culture, but care should always be taken to do the appropriate controls when exploring new cell lines or tissues. As so many new FPs have become available, it is unknown whether any may be substantially more toxic to cells than AFPs. In our hands, tetrameric proteins can be somewhat toxic to bacteria, especially if they display a substantial amount of aggregation, but monomeric proteins are generally nontoxic. It seems difficult or impossible to generate transgenic mice widely expressing tetrameric RFPs, whereas several groups have successfully obtained mice expressing monomeric RFPs[24,25].

Environmental sensitivity

When images must be quantitatively interpreted, it is critical that the fluorescence intensity of the protein used not be sensitive to factors other than those being studied. Early YFP variants were relatively chloride sensitive, a problem that has been solved in the Citrine and Venus (and likely YPet) variants[1,2,16]. Most FPs also have some acid sensitivity. For general imaging experiments, all FPs listed in Table 1 have sufficient acid resistance to perform reliably. More acid-sensitive FPs, however, may give poor results when targeted to acidic compartments such as the lumen of lysosomes or secretory granules, and may confound quantitative image interpretation if a given stimulus or condition leads to altered intracellular pH. Because of this, one should avoid using mOrange[4], GFPs or YFPs for experiments in which acid quenching could produce artifacts. Conversely, the pH sensitivity of these proteins can be very valuable to monitor organellar luminal pH or exocytosis[26,27].

Table 2 | Recommended filter sets

	Fluorescent protein	Excitation[a]	Emission[a]
Multiple labeling	Cerulean or CyPet	425/20	480/40
	mCitrine or YPet	495/10	525/20
	mOrange or mKO	545/10	575/25
	mCherry	585/20	675/130
	mPlum	585/20	675/130
Single labeling	T-Sapphire	400/40	525/80
	Cerulean or CyPet	425/20	505/80
	Emerald	470/20	530/60
	mCitrine or YPet	490/30	550/50
	mOrange or mKO	525/20	595/80
	tdTomato	535/20	615/100
	mStrawberry	550/20	630/100
	mCherry	560/20	640/100
	mPlum	565/40	670/120

[a]Values are given as center/bandpass (nm). Bandpass filters with the steepest possible cutoff are strongly preferred.

Multiple labeling

One of the most attractive prospects presented by the recent development of such a wide variety of monomeric FPs is for multiple labeling of fusion proteins in single cells. Although linear unmixing systems promise the ability to distinguish between large numbers of different fluorophores with partially overlapping spectra[28], it is possible even with a simpler optical setup to clearly distinguish between three or four different FPs. Using the filter sets recommended in Table 2, one may image cyan, yellow, orange and red (Cerulean or CyPet, any YFP, mOrange or mKO and mCherry) simultaneously with minimal crosstalk. To produce even cleaner spectral separation, one could image cyan, orange and far-red (Cerulean or CyPet, mOrange or mKO, and mPlum)[2,4,5,10].

Additional concerns for complex experiments

For more complex imaging experiments, additional factors come into play when choosing the best genetically encoded fluorescent probe, many of which are beyond the scope of this perspective. For FRET applications, the choice of appropriate donor and acceptor FPs may be critical, and seemingly small factors (such as linker length and composition for intramolecular FRET constructs) may have a substantial role. The recent development of the FRET-optimized cyan-yellow pair CyPet and YPet holds great promise for the improvement of FRET sensitivity[2], and it is the current favorite as a starting point for new FRET sensors but has yet to be proven in a wide variety of constructs. For experiments requiring photoactivatable or photoconvertible tags, several options are available, including photoactivatable GFP (PA-GFP)[15] and monomeric RFP (PA-mRFP)[13], reversibly photoswitchable Dronpa[29], the tetrameric kindling fluorescent protein (KFP)[9], and the green-to-red photoconvertible proteins KikGR[14] and EosFP[12] (the latter is available as a bright tandem dimer) and cyan-to-green photoconvertible monomer PS-CFP[8]. A more detailed (but probably not exhaustive) list of options for these more advanced applications of FPs are listed in Supplementary Table 3 online. In addition, a recent review is available detailing the potential applications of photoactivatable FPs[30].

Future developments

Although the present set of FPs has given researchers an unprecedented variety of high-performance options, there are still many areas that could stand improvement. In the future, monomeric proteins with greater brightness and photostability will allow for even more intensive imaging experiments, efficiently folding monomeric photoconvertible proteins will improve our ability to perform photolabeling of fusion proteins, FRET pairs engineered to be orthogonal to the currently used CFP-YFP pairs will allow imaging of several biochemical activities in the same cell, and the long-wavelength end of the FP spectrum will continue to expand, allowing for more sensitive and efficient imaging in thick tissue and whole animals. By applying the principles put forth here, researchers may evaluate each new development in the field of FPs and make an informed decision as to whether it fits their needs.

Note: Supplementary information is available on the Nature Methods website.

ACKNOWLEDGMENTS

Thanks to S. Adams for helpful advice on choosing filter sets. N.C.S. is a Howard Hughes Medical Institute Predoctoral Fellow. This work was additionally supported by US National Institutes of Health (NS27177 and GM72033) and Howard Hughes Medical Institutes.

COMPETING INTERESTS STATEMENT

The authors declare competing financial interests (see *Nature Methods* website for details).

Published online at http://www.nature.com/naturemethods/
Reprints and permissions information is available online at http://npg.nature.com/reprintsandpermissions/

1. Nagai, T. *et al.* A variant of yellow fluorescent protein with fast and efficient maturation for cell-biological applications. *Nat. Biotechnol.* **20**, 87–90 (2002).
2. Nguyen, A.W. & Daugherty, P.S. Evolutionary optimization of fluorescent proteins for intracellular FRET. *Nat. Biotechnol.* **23**, 355–360 (2005).
3. Rizzo, M.A., Springer, G.H., Granada, B. & Piston, D.W. An improved cyan fluorescent protein variant useful for FRET. *Nat. Biotechnol.* **22**, 445–449 (2004).
4. Shaner, N.C. *et al.* Improved monomeric red, orange and yellow fluorescent proteins derived from Discosoma sp. red fluorescent protein. *Nat. Biotechnol.* **22**, 1567–1572 (2004).
5. Wang, L., Jackson, W.C., Steinbach, P.A. & Tsien, R.Y. Evolution of new nonantibody proteins via iterative somatic hypermutation. *Proc. Natl, Acad. Sci. USA* **101**, 16745–16749 (2004).
6. Zapata-Hommer, O. & Griesbeck, O. Efficiently folding and circularly permuted variants of the Sapphire mutant of GFP. *BMC Biotechnol.* **3**, 5 (2003).
7. Ando, R., Hama, H., Yamamoto-Hino, M., Mizuno, H. & Miyawaki, A. An optical marker based on the UV-induced green-to-red photoconversion of a fluorescent protein. *Proc. Natl. Acad. Sci. USA* **99**, 12651–12656 (2002).
8. Chudakov, D.M. *et al.* Photoswitchable cyan fluorescent protein for protein tracking. *Nat. Biotechnol.* **22**, 1435–1439 (2004).
9. Chudakov, D.M. *et al.* Kindling fluorescent proteins for precise *in vivo* photolabeling. *Nat. Biotechnol.* **21**, 191–194 (2003).
10. Karasawa, S., Araki, T., Nagai, T., Mizuno, H. & Miyawaki, A. Cyan-emitting and orange-emitting fluorescent proteins as a donor/acceptor pair for fluorescence resonance energy transfer. *Biochem. J.* **381**, 307–312 (2004).
11. Matz, M.V. *et al.* Fluorescent proteins from nonbioluminescent *Anthozoa* species. *Nat. Biotechnol.* **17**, 969–973 (1999).
12. Wiedenmann, J. *et al.* EosFP, a fluorescent marker protein with UV-inducible green-to-red fluorescence conversion. *Proc. Natl. Acad. Sci. USA* **101**, 15905–15910 (2004).
13. Verkhusha, V.V. & Sorkin, A. Conversion of the monomeric red fluorescent protein into a photoactivatable probe. *Chem. Biol.* **12**, 279–285 (2005).
14. Tsutsui, H., Karasawa, S., Shimizu, H., Nukina, N. & Miyawaki, A. Semi-rational engineering of a coral fluorescent protein into an efficient highlighter. *EMBO Rep.* **6**, 233–238 (2005).
15. Patterson, G.H. & Lippincott-Schwartz, J. Selective photolabeling of proteins using photoactivatable GFP. *Methods* **32**, 445–450 (2004).
16. Griesbeck, O., Baird, G.S., Campbell, R.E., Zacharias, D.A. & Tsien, R.Y. Reducing the environmental sensitivity of yellow fluorescent protein. Mechanism and applications. *J. Biol. Chem.* **276**, 29188–29194 (2001).
17. Zhang, J., Campbell, R.E., Ting, A.Y. & Tsien, R.Y. Creating new fluorescent probes for cell biology. *Nat. Rev. Mol. Cell Biol.* **3**, 906–918 (2002).
18. Tsien, R.Y. The green fluorescent protein. *Annu. Rev. Biochem.* **67**, 509–544 (1998).
19. Gross, L.A., Baird, G.S., Hoffman, R.C., Baldridge, K.K. & Tsien, R.Y. The structure of the chromophore within DsRed, a red fluorescent protein from coral. *Proc. Natl. Acad. Sci. USA* **97**, 11990–11995 (2000).
20. Hansen, M.C., Palmer, R.J., Jr, Udsen, C., White, D.C. & Molin, S. Assessment of GFP fluorescence in cells of *Streptococcus gordonii* under conditions of low pH and low oxygen concentration. *Microbiology* **147**, 1383–1391 (2001).
21. Zhang, C., Xing, X.H. & Lou, K. Rapid detection of a *gfp*-marked *Enterobacter aerogenes* under anaerobic conditions by aerobic fluorescence recovery. *FEMS Microbiol. Lett.* **249**, 211–218 (2005).
22. Verkhusha, V.V. & Lukyanov, K.A. The molecular properties and applications of *Anthozoa* fluorescent proteins and chromoproteins. *Nat. Biotechnol.* **22**, 289–296 (2004).
23. Zacharias, D.A., Violin, J.D., Newton, A.C. & Tsien, R.Y. Partitioning of lipid-modified monomeric GFPs into membrane microdomains of live cells. *Science* **296**, 913–916 (2002).
24. Long, J.Z., Lackan, C.S. & Hadjantonakis, A.K. Genetic and spectrally distinct *in vivo* imaging: embryonic stem cells and mice with widespread expression of a monomeric red fluorescent protein. *BMC Biotechnol.* **5**, 20 (2005).
25. Zhu, H. *et al.* Ubiquitous expression of mRFP1 in transgenic mice. *Genesis* **42**, 86–90 (2005).
26. Miesenbock, G., De Angelis, D.A. & Rothman, J.E. Visualizing secretion and synaptic transmission with pH-sensitive green fluorescent proteins. *Nature* **394**, 192–195 (1998).
27. Matsuyama, S., Llopis, J., Deveraux, Q.L., Tsien, R.Y. & Reed, J.C. Changes in intramitochondrial and cytosolic pH: early events that modulate caspase activation during apoptosis. *Nat. Cell Biol.* **2**, 318–325 (2000).
28. Hiraoka, Y., Shimi, T. & Haraguchi, T. Multispectral imaging fluorescence microscopy for living cells. *Cell Struct. Funct.* **27**, 367–374 (2002).
29. Habuchi, S. *et al.* Reversible single-molecule photoswitching in the GFP-like fluorescent protein Dronpa. *Proc. Natl. Acad. Sci. USA* **102**, 9511–9516 (2005).
30. Lukyanov, K.A., Chudakov, D.M., Lukyanov, S. & Verkhusha, V.V. Innovation: Photoactivatable fluorescent proteins. *Nat. Rev. Mol. Cell Biol.* (2005); advance online publication, 15 September 2005 (doi:10.1038/nrm1741).
31. Shkrob, M.A. *et al.* Far-red fluorescent proteins evolved from a blue chromoprotein from *Actinia equina*. *Biochem. J.* (2005); advance online publication, 15 September 2005 (doi: 10.1042/BJ20051314).

Fluorescence microscopy

Jeff W Lichtman[1] & José-Angel Conchello[2,3]

Although fluorescence microscopy permeates all of cell and molecular biology, most biologists have little experience with the underlying photophysical phenomena. Understanding the principles underlying fluorescence microscopy is useful when attempting to solve imaging problems. Additionally, fluorescence microscopy is in a state of rapid evolution, with new techniques, probes and equipment appearing almost daily. Familiarity with fluorescence is a prerequisite for taking advantage of many of these developments. This review attempts to provide a framework for understanding excitation of and emission by fluorophores, the way fluorescence microscopes work, and some of the ways fluorescence can be optimized.

Many of the technical improvements in microscopes over the years have centered on increasing the contrast between what is interesting (signal) and what is not (background). Fluorescence microscopy is the quintessential example, as it aims to reveal only the objects of interest in an otherwise black background. Because of its intrinsic selectivity, fluorescence imaging has become the mainstay of microscopy in the service of biology. Over the past several decades, organic chemists have devised many thousands of fluorescent probes that provide a means of labeling virtually any imaginable aspect of biological systems. For example, the Molecular Probes Handbook, tenth edition online (http://probes.invitrogen.com/handbook/), which is perhaps the largest compendia of fluorescence applications for biologists, has 23 chapters, 14 of which describe the 3,000 or so fluorescent probes for a wide range of cell biological questions. The large spectral range of available fluorophores allows simultaneous imaging of different cellular, subcellular or molecular components. In addition, the co-opting of intrinsically fluorescent gene products, most notably green fluorescent protein (GFP) and its variants, has allowed molecular biologists to genetically tag protein components of living systems and usher in a new era for fluorescence. Lastly, the rapidly advancing innovations of laser scanning confocal and two-photon microscopes mean that fluorescence approaches now provide a powerful approach to seeing microscopic structures in three dimensions, even deep within tissues. For these reasons it is difficult to do cell or molecular biology without understanding the basics of fluorescence, and this trend is accelerating. According to PubMed, 127,804 articles used the word 'fluorescence' in their title or abstract in 2004—that is more than the total number of fluorescence papers in the previous five years (1999–2003) combined. Our aim is to describe concepts that underpin fluorescence microscopy and highlight some of the pitfalls frequently encountered. There are several more detailed accounts that focus on specific aspects of this large subject, which we will refer to frequently to guide more in-depth reading.

PRINCIPLES OF FLUORESCENCE

Excitation and emission

Fluorescence microscopy requires that the objects of interest fluoresce. Fluorescence is the emission of light that occurs within nanoseconds after the absorption of light that is typically of shorter wavelength. The difference between the exciting and emitted wavelengths, known as the Stokes shift, is the critical property that makes fluorescence so powerful. By completely filtering out the exciting light without blocking the emitted fluorescence, it is possible to see only the objects that are fluorescent. This

[1]Department of Molecular and Cell Biology, Harvard University, 7 Divinity Avenue, Cambridge, Massachusetts 02138, USA. [2]Molecular, Cell and Developmental Biology, Oklahoma Medical Research Foundation, 825 N.E. 13th Street, Oklahoma City, Oklahoma 73104, USA. [3]Program in Biomedical Engineering, University of Oklahoma, 100 East Boyd Street, Norman, Oklahoma 73019, USA. Correspondence should be addressed to J.W.L. (jeff@mcb.harvard.edu).

PUBLISHED ONLINE 18 NOVEMBER 2005; DOI:10.1038/NMETH817

approach to contrast is superior to absorption techniques in which objects are stained with agents that absorb light. With absorbance dyes, the amount of light absorbed becomes only infinitesimally different from the background for small objects. In fluorescence, however, even single fluorescent molecules are visible if the background has no autofluorescence.

Fluorophores

Molecules that are used by virtue of their fluorescent properties are called fluorophores. The outermost electron orbitals in the fluorophore molecule determine both its efficiency as a fluorescent compound and the wavelengths of absorption and emission. When fluorescent compounds in their so-called 'ground state' absorb light energy (photons), alterations in the electronic, vibrational and rotational states of the molecule can occur. The absorbed energy sometimes moves an electron into a different orbital that is on average farther away from the nucleus. This transition to an 'excited state' occurs very rapidly (in femtoseconds). Usually the excitation process also sets in motion molecular vibrations in which the internuclear distances vary over time. All this absorbed energy is eventually shed. Vibrational relaxation and fluorescence emission are the chief ways a fluorophore returns to its low-energy ground state.

Whereas many organic substances have intrinsic fluorescence (autofluorescence), and a few are useful for specific labeling of components in biological systems, the typical approach to fluorescence microscopy is to take advantage of synthesized compounds that have some degree of conjugated double bonds. Such compounds often have ring structures (aromatic molecules) with pi bonds that easily distribute outer orbital electrons over a wide area. These compounds are optimal for fluorescence microscopy because the energy differences between excited state and ground state orbitals are small enough that relatively low-energy photons in the visible part of the electromagnetic spectrum can be used to excite electrons into excited states. In general, the more conjugated bonds in the molecule, the lower the excited energy requirement and the longer the wavelength (redder) the exciting light can be. The emitted light is shifted in the same direction. In addition, the efficiency, as measured by fluorescent quantum yield, increases with the number of pi bonds.

In GFP, a post-translational alteration of three amino acids, (Ser-Tyr-Gly) located in an α helix running down the center of the barrel-shaped protein forms an imidazolidone ring with conjugated double bonds and planar structure[1]. This ring structure is the chromophore. Mutations in the ring structure that add more conjugated bonds shift the fluorescence excitation and emission to longer wavelengths—as in yellow fluorescent protein (YFP).

Jablonski diagrams

A useful approach to understand the details of the excitation and emission process is to render the process in the form of a diagram first conceived by Alexander Jablonski in the 1930s (Fig. 1a). Those interested in a more rigorous treatment of this subject might read the first few chapters in several excellent texts[2–4]. On the left side of the diagram are the singlet states. These states maintain the paired + ½ and – ½ spin states of the electrons as they are normally, with each electron in a pair having opposite spins (see **Box 1** for useful

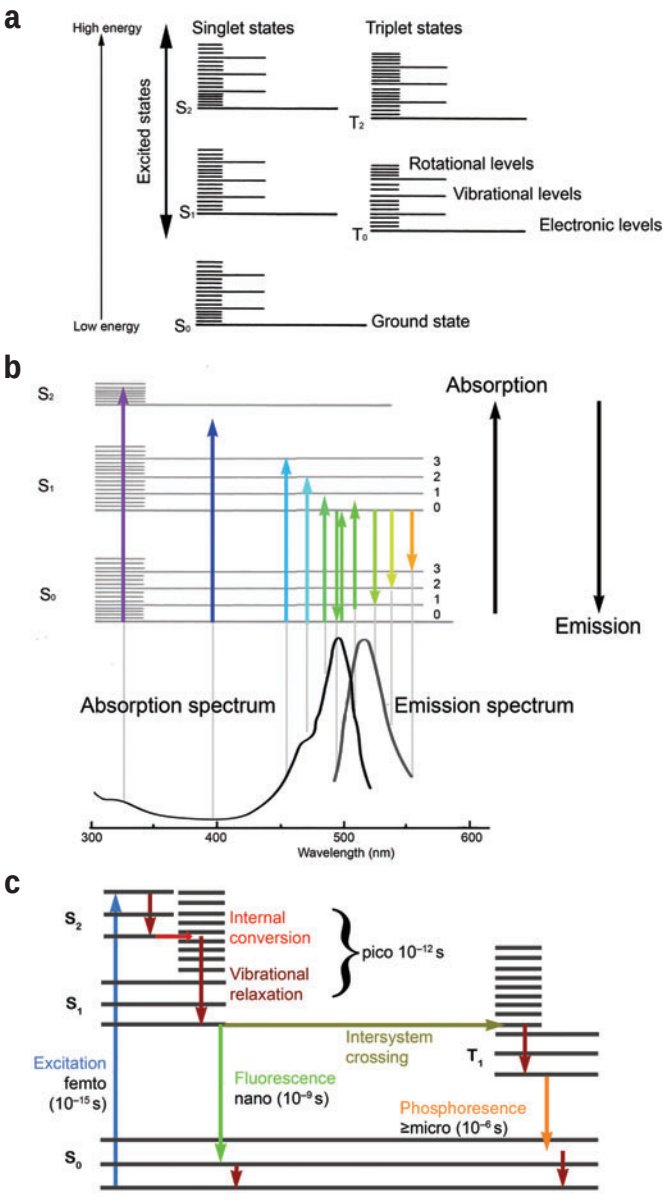

Figure 1 | Fluorescence fundamentals. (**a**) Jablonski diagram displaying the energy states of a molecule. Molecules not absorbing energy are mainly confined to the lowest vibrational states of the ground state S_0. (**b**) The spectral characteristics related to absorption and emission of energy by a molecule can be related to the size of the energy steps needed to bring a molecule from one energy level to another. The absorption and emission spectra of the common fluorophore FITC are shown below a Jablonski diagram. Each vertical gray line aligns the spectra with the energy of the absorbed (arrows pointing up) or emitted (arrows pointing down) photons. The arrows are colored to represent the wavelength of the photons. For example, the purple arrow to the left represents the energy of an ultraviolet photon that can cause the molecule to transition from the ground state to the second singlet excited state. The orange arrow on the right represents the lowest energy photon that can be emitted by this molecule as it drops back from the lowest energy state of S_1 to a high vibrational state of S_0. Note in the region of overlap of the absorption and emission spectra, some photons (for example, the green, up-pointing arrow) are absorbed when the vibrational level is not at its lowest level. Also note the symmetry between the absorption and emission curves owing to the similarity of transitions to vibrational states in S_0 and S_1. (**c**) The times that the various steps in fluorescence excitation and emission and phosphorescence take.

definitions). S_0 is the ground state and represents the energy of a molecule that is not being excited by light. S_1 and S_2 are excited singlet states in which an outer electron is boosted into a different orbital. S_2 contains more energy than S_1 and S_1 more energy than the ground state, S_0. On the right of the diagram are the triplet states in which an outer electron, boosted to a new orbital, has also undergone a subsequent reversal in spin so that a former pair of electrons are now parallel. From quantum theory, it is forbidden that an electron be in any spin state other than the two that exist in the paired electrons (+½ or –½); thus, for the electron to reverse spin it must go through a 'forbidden' transition, which is relatively unlikely. Nonetheless electrons can undergo 'intersystem crossing' between singlet and triplet states. This has important consequences, which will be discussed later.

Excitation spectra

When a fluorophore absorbs light, all the energy possessed by a photon is transferred to the fluorophore. This energy is inversely related to the photon's wavelength ($E = h \times c / \lambda$, where h is Plank's constant and c and λ are the speed and wavelength of light in vacuum, respectively). If the absorbed photon's energy is greater than that needed to exactly transition from the ground state to the lowest energy level of S_1, the molecule will also undergo a change in vibration, rotation and/or move into an even higher electronic orbital (S_2). Thus, there is a range of wavelengths that can excite a molecule. The minimum energy required for fluorescence, however, is from a photon that can cause the transition of an electron into a higher electronic excited state (that is, S_0 to S_1).

The time it takes a molecule to transition from the ground state to an excited state is extremely brief, on the order of femtoseconds (roughly equal to the time over which a photon of a particular wavelength traveling at the speed of light takes to cross paths with a molecule). Whereas one photon of the appropriate energy typically causes this transition, it is also possible for multiple photons to add their energy to bring a molecule to the excited state. For example, if two photons with half the energy (that is, twice the wavelength) of that needed to reach the excited state impinge on a molecule at the same time, their energies can sum and provide for two-photon excitation. Given the brevity of the absorption process, only enormously high light intensities provide sufficient probability for multiple low-energy (infrared) photons to be in the same place at nearly the same time.

The excitation spectrum of a fluorophore can be determined empirically by measuring the fluorescence yield by shining light of various wavelengths on a cuvette containing the fluorophore and recording the amount of fluorescent Stokes-shifted light that is produced at the peak wavelength of the fluorescence spectrum. The peaks and valleys in the excitation spectrum reflect the energy levels in the molecule's Jablonski diagram (Fig. 1b). For example, for many molecules there are only few vibrational or rotational states between the highest energy level of S_1 and the lowest level of S_2, hence for many fluorophores the absorption spectrum shows a dip between the longer wavelength peak related to exciting to an S_1 level and the shorter wavelength absorption to an S_2 level. Not surprisingly, given the threshold energy needed to get excitation, the energy for excitation has a sharper cutoff on the low-energy–long-wavelength side of the spectrum than the short-wavelength–high-energy side where there is no sharp cutoff; although practically speaking, the optical opacity of glass to ultraviolet light limits excitation in a fluorescent microscope beyond the near UV.

The probability that a fluorophore will absorb a photon is called its molar extinction coefficient, ε, in units of $M^{-1}cm^{-1}$. This property, which measures the probability of absorption of light as it passes through a solution containing the fluorophore, is similar (although the units are different) to the dye's 'cross-section', implying that the molecule can be imagined as a target and the bigger the cross-section, the more likely it is that it will catch a photon. The value of ε is specified for the wavelength that is the absorption maximum, which is where its cross-section is largest. Useful small organic fluorophores have ε values between ~25,000 and ~200,000 (the higher, the better the absorber). So-called 'enhanced' GFP (EGFP) has an excitation maximum shifted to 488 nm and an ε of approximately 60,000, which is five times higher than wild-type GFP with an excitation maximum of 470 nm. Dyes with high extinction coefficients tend to be useful when light intensity needs to be kept to a minimum, such as when imaging living tissues or when there are very few fluorophore molecules[5]. All

BOX 1 ELECTRONIC STATES

Spin. Spin is the amount of angular momentum associated with an elementary particle or a nucleus. Electrons have an intrinsic and invariable internal motion that corresponds to a spin of ½ and provides the electron with directional orientation. The electron also has an intrinsic magnetic moment directed along its spin axis. In the case of an atomic electron, the magnetic moment will be oriented parallel or antiparallel, with respect to the magnetic field, to the rest of the atom, which is indicated by the associated spin quantum number with values of +½ or –½.

Singlet state. Electrons normally reside as pairs with opposite spins within a single orbital; this results in a cancellation of their magnetic moments to produce a so-called singlet state.

Triplet state. A pair of nonbonding electrons may exist in two separate orbitals with the electron spins parallel to each other. Atoms or molecules with such a configuration will have an overall magnetic moment that may be parallel, perpendicular or antiparallel to the direction of a magnetic field. These three possible alignments correspond to three forms of slightly different energy, so the atom or molecule can exist in all three forms and is said to be in a triplet state. Triplet states tend to be relatively long-lived.

Ground state. This is the normal, nonexcited state of a molecule. When talking about the ground electronic state, a molecule may still have excess vibrational and rotational energy.

Excited state. When an electron absorbs sufficient energy, it can transition to a higher energy level (higher orbital) and thus create an atom or molecule in an excited state. Excited states tend to be relatively short-lived and return to electronic states of lower energy, ultimately to the ground state, by losing their excess energy. This energy loss may involve radiationless transitions—such as internal conversion, intersystem crossing or vibrational relaxation—or radiative transitions—such as fluorescence and phosphoresence.

other things being equal, a dye with a higher extinction coefficient will also give a greater signal for the same amount of light-induced background than a dye with a lower extinction coefficient.

Emission spectra

Once excited, the molecule uses several different pathways to ultimately lose the absorbed energy and return to the ground state (Fig. 1c). 'Internal conversion' is a transition between electron orbital states (such as S_2 to S_1). Strictly speaking, internal conversion allows isoenergetic transitions from low vibrational energies of one electronic state to high vibrational modes of a lower electronic state, so no energy is lost during this transition but the extra energy is eventually shed through vibrational relaxation. During vibrational relaxation the vibrational energy in the fluorophore is transferred to nearby molecules via direct interactions. In aqueous medium, water is the likely energy recipient. Notably, vibrational relaxation does not lead to any emitted photons. Internal conversion and vibrational relaxation takes picoseconds and typically bring the molecule back to the lowest energy level of S_1. Internal conversion sometimes transitions excited molecules all the way to the ground state S_0 but for most fluorophores the energy difference between the ground state vibrational modes and first singlet excited state is large enough that this path is not preferred. The excited molecule now has a similar vibrational state as it did in the ground state but the outer electron orbital still contains extra energy.

In good fluorophores, the preferred final energy path back to the ground state is the expulsion of a photon whose energy covers the gap between the lowest vibrational state of S_1 and any one of the vibrational or rotational states of S_0. The emission spectrum of a fluorophore is just the range of wavelengths this emitted photon can have (Fig. 1b). This spectrum can be empirically determined by exciting the fluorophore (typically at its peak absorbance wavelength) and using a device to measure the fluorescence spectrum. Given the nonradiative drop back to the lowest level of S_1, the wavelength of the emitted light is not related to the particular wavelength of the exciting light; thus one cannot shift the emission spectrum by changing the color of the exciting light. In most cases the outgoing emitted light is also not related to the incoming direction of the exciting photons so photons can be emitted in the opposite direction of the incoming photons, as occurs in standard epifluorescence microscopes described below.

Because the emission starts from the lowest level of S_1, the energy of the emitted photon is typically less than the absorbed photon as vibrational relaxation and internal conversion remove the excess energy—this is the origin of the Stokes shift. The magnitude of the Stokes shift varies considerably from one fluorophore to another. Generally large shifts have the advantage of easier separation of the exciting and emitted light. But not all fluorescent emission occurs at longer wavelengths than the exciting light. Often a minority the ground state fluorophores is in one of the higher vibrational states of S_0 when they are excited. In these cases a photon can drop back in a larger energy jump than was needed to reach S_1, accounting for the overlap of the emission and excitation spectra (Fig. 1b).

A more serious overlap concern relates to imaging multiple fluorophores in the same sample. Given the broad excitation and emission spectra of each fluorophore, even spectrally shifted fluorophores can be excited by the same wavelength and exhibit overlapping emission. These overlaps can cause confusing crosstalk or bleed-through between signals associated with different fluorophores in the same sample. This difficulty has been ameliorated by organic synthesis of ever wider spectral ranges of fluorophores (by adding more conjugated bonds) that now permit a user to choose fluorophores with little overlap in excitation and/or emission spectra (Fig. 2a,b). Crosstalk, however, remains a serious problem with fluorescent proteins that have very broad excitation and emission spectra relative to small organic chemical fluorophores (Fig. 2c). Here too, new wavelength-shifted variants may come to the rescue[6].

Although shifted to longer wavelengths, the spectrum of the emitted fluorescence has mirror symmetry with the main part of the spectrum of the absorbed light (Fig. 1b). This symmetry is related to final drop back to the ground state from the lowest vibrational state of S_1. The vibrational transitions going back to the ground state are the same as those that occurred during absorbance. In each case the molecule is beginning typically in the '0' vibrational state and moving to either

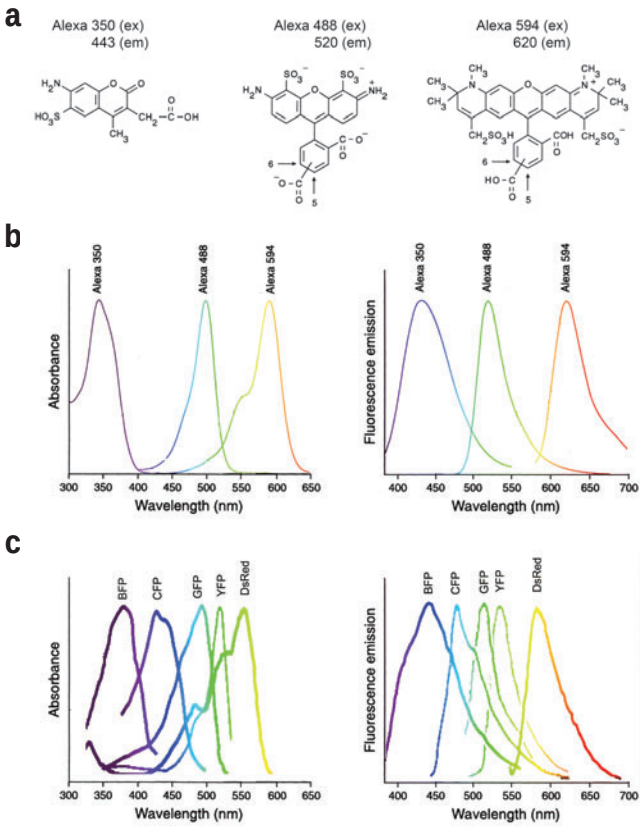

Figure 2 | The spectral and structural properties of fluorophores. (**a**) Three Alexa fluorescent molecules have conjugated double bonds but the excitation and fluorescence emission characteristics shift to longer wavelengths in proportion the degree of conjugated bonds. The 17 Alexa Fluor dyes, sold by Invitrogen's Molecular Probes span the near-UV, visible and near infrared. Along with the wavelength shift, the cross-section of the dyes increases. Alexa 350 has an extinction coefficient of 19,000 $cm^{-1}M^{-1}$, whereas for Alexa Fluor 750 it is 240,000 $cm^{-1}M^{-1}$. (**b**) The absorption spectra and emission spectra are largely nonoverlapping for these particular Alexa fluorophores. (**c**) In contrast, the mutated spectral variants of fluorescent protein from the *Aequorea* species of jelly fish and *Discosoma* species of reef coral have substantial overlap in both excitation and emission spectra. Recent attempts to generate more red-shifted fluorescent proteins have raised the possibility that eventually cross-talk will not be a major problem for fluorescent proteins either[6]. Data in **a** from[32]; **b**, from the Invitrogen pamphlet on Alexa Fluor Dyes; **c**, from the Clontech website.

the same or a higher vibrational state, for example, 0, 1, 2 or 3. These vibrational transitions have the same likelihood in either direction. For example, S_0 level vibrational level 0 to S_1 level 3 is comparable in likelihood to S_1 vibrational level 0 to S_0 level 3. Hence the absorption peaks and the emission peaks are the same but shifted to longer wavelengths for the emission. Knowing the absorbance and the emission spectrum for a fluorophore helps decide which filters are optimal, which lasers in scanning microscopes to excite dyes with, and how best to get excitation of one dye without crosstalk from another.

Intersystem crossing

Unfortunately, fluorescence emission is not the only way fluorophores in the excited state can lose energy. Another pathway of energy loss occurs after intersystem crossing by means of a forbidden transition to the triplet state (Fig. 1a,c). In many fluorophores, triplet state vibrational energy levels overlap with the lowest energy level in S_1. This overlap favors intersystem crossing followed by internal conversion to the lowest energy of T_1. The triplet state molecule now has no easy path back to the lower-energy singlet ground state, as this transition requires the triplet outer electron to again undergo a forbidden transition. Although some triplet-state molecules reach the ground state without light emission, in many cases light emission termed phosphorescence does occur, but it can take microseconds as it depends on the unlikely forbidden transition. In the meantime triplet-triplet transitions can move the molecule into higher triplet states if another photon is absorbed, further delaying any light emission. In laser scanning microscopes where the fluorescence is measured serially in rapid succession from one point to the next, the delay of the phosphorescent photon is often too long to allow it to be counted for the correct pixel, thus weakening the fluorescent signal. Furthermore, as molecules in the triplet state are unable to cycle through absorbance and emission rapidly, the state temporarily removes potentially fluorescent molecules from the total pool. Last, and perhaps the most problematic issue, is that triplet-state molecules can undergo photochemical reactions that cause irreversible bleaching and phototoxicity.

Quantum yield and fluorescence intensity

The quantum yield of a fluorophore is a measure of the total light emission over the entire fluorescence spectral range. It is measured as the ratio of fluorescence emission to nonradiative energy losses. With very intense light sources, such as lasers used in laser scanning microscopes, the quantum yield provides an accurate measure of the maximum intensity that can be obtained with a fluorophore. With dimmer light sources, the intensity depends critically on the product of the extinction coefficient and the quantum yield.

A fluorescent dye such as fluorescein has a high quantum yield of about ~0.9 and GFP has a quantum yield of ~0.8. Higher quantum yield not only increases fluorescence intensity but also means alternative competing photochemical processes associated with intersystem crossing, such as bleaching and free radical formation, are less likely. Except in situations where one is trying to do some photochemistry with a dye, the closer the quantum yield is to 1 the better. For example, eosin, a brominated derivative of fluorescein, has a quantum yield that is one-fifth that of fluorescein, but a 20-fold greater yield of a reactive intermediate (singlet oxygen) from interactions between its triplet state and oxygen. Eosin excitation can be used to photoconvert diamino benzidine into an electron-dense product to mark sites of fluorescence for electron microscopic work[7].

Excited state lifetime, energy transfer and photochemistry

The time the molecule remains excited before yielding a photon is called the excited state lifetime. This time is dominated by the duration the molecule spends in the lowest level of S_1, which is typically several nanoseconds before spontaneous decay to the ground state. The lifetime can be made briefer if another molecule nearby can absorb the energy. Such intermolecular interactions both reduce the fluorescent lifetime and the quantum yield. Fluorescence lifetime imaging microscopy (FLIM) probes alterations in the milieu in the immediate vicinity of a fluorescent molecule and is thus an important tool for studying molecular interactions between fluorescently labeled molecules and their interacting partners[8,9]. If the interacting partner is itself a fluorophore, the energy in an excited state molecule can excite the nearby fluorophore. This phenomenon, known as fluorescence resonance energy transfer (FRET) occurs when a very nearby fluorophore's absorption spectrum overlaps with the emission spectrum of the excited fluorophore. The donor's energy is absorbed by the acceptor, which then emits a photon shifted to a longer wavelength[10]. The strong distance dependence of this energy transfer allows FRET to assay changes in intramolecular distances that are far below the resolution of the light microscope.

Excited state molecules can also participate in a wide range of photochemical reactions[4]. Photouncaging, for example, is widely used in biology to release biologically active compounds after light induced release of a blocking group. Some fluorescent proteins can also undergo a change in structure and spectral properties with light. Notably, the red chromophore in Kaede, a fluorescent protein from a coral is generated from a green form of this protein that is converted by exposure to ultraviolet light[11,12].

PHYSIOLOGICAL FLUOROPHORES

At present, there are many probes that assay some aspect of physiological processes by accumulating in organelles such as mitochondria, endoplasmic reticulum, nucleus or synaptic vesicles[13,14]. Fluorophores have also been developed to take advantage of the fact that a fluorophore's absorption and emission properties can be highly sensitive to a changing milieu. Fluorescent sensors change their absorbance and/or emission spectra when bound to calcium ions[15,16] hydrogen ions[17] or other molecules of interest. Although many sensors allow only an estimation of the change in concentration of their target by undergoing a simple increase or decrease in fluorescence, some of these fluorophores can be used in 'ratiometric' assays that provide a quantitative way to measure concentration. By taking the ratio of the dye's behavior at two emission or absorption wavelengths—one being the wavelength sensitive to the target molecule and the other being one that is insensitive to the target—it is possible to normalize for changes unrelated to a change in target concentration, such as the distance through a cell, an inhomogeneous milieu or local dye concentrations that might make local absorbance or emission intensity vary for reasons other than changes in the local concentration of the molecule being studied. Doing ratiometric imaging correctly requires a full understanding of the sources of measurement errors and how the calculations are made. Fortunately there are a number of excellent reviews of this powerful quantitative technique (see[18]).

Genetically encoded fluorescent probes that monitor calcium and a variety of other intracellular signals are rapidly evolving, and are beginning to provide windows into intracellular metabolism in intact systems[19–21]. Some dyes are sensitive to electrical fields, and thus, when located in a membrane separating two compartments at different

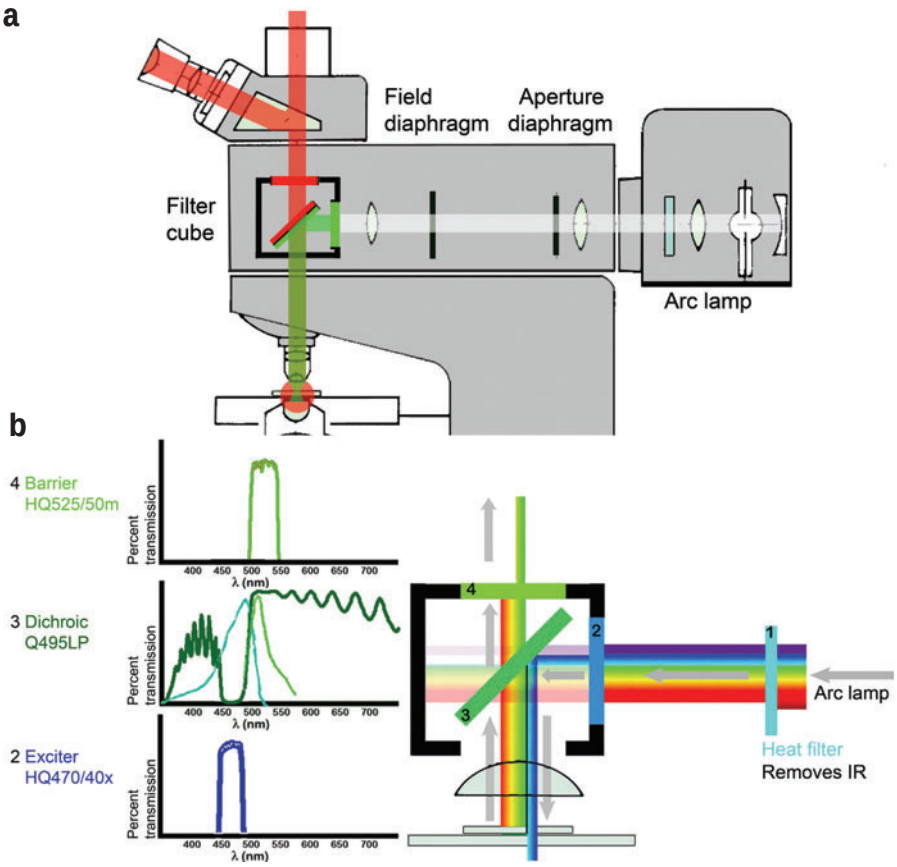

Figure 3 | The fluorescence microscope. (**a**) Epi-illumination fluorescence microscopes use the objective both to illuminate and image the specimen. Shown is an upright microscope with the slide at the bottom. The light source, in this case an arc lamp, sends full-spectrum light to the specimen by way of a fluorescence 'cube' that selectively illuminates the specimen with a wavelengths that excite a particular fluorophore (shown, green light to excite rhodamine). The red fluorescence that is excited sends photons in all directions and a fraction are collected by the objective and sent through the cube to the eye or camera port above. The cube has two filters, the dichroic mirror and barrier filter, to prevent the exciting wavelengths from reaching the detector. (**b**) The details of a cube designed by Chroma Technologies to excite and detect EGFP. The three main components (labeled 2, 3 and 4) have specific spectral features that are ideal for GFP. Note that the dichroic mirror[3] splits between reflection and transmission right between the absorption and emission peaks of the GFP, which are superimposed in blue and green, respectively.

potentials, they can provide an optical signal of transmembrane voltage[22,23]. Fluorescent proteins that sense membrane potential by coupling to voltage-sensitive ion channels offer the possibility of someday monitoring neural activity in many neurons simultaneously in living animals[24].

Clearly the evolution of fluorescence indicators of physiological functions is one of the triumphs of modern cell and molecular biology. The key point to their use, however, requires looking over time as well as space. Such multidimensional imaging requires highly efficient detectors and sometimes rapid switching of filters, and overcoming the many challenges of imaging living cells[14,18,25].

THE FLUORESCENCE MICROSCOPE

Given the Stokes shift, it is easy to imagine how one might build a fluorescence microscope: illuminate the specimen with one wavelength and filter the return light to only see longer wavelength–shifted fluorescence. Indeed this is similar to the way Sir George Gabriel Stokes first noted fluorescence: purportedly, a purple stained glass window filtered sunlight onto a flask of quinine water, which he then observed to emit blue light through a glass filled with white wine that blocked the purple light[3]. The preferred approach in modern fluorescence microscopes is epi-illumination (Fig. 3a). In this configuration the microscope objective not only has the familiar role of imaging and magnifying the specimen, but also serves as the condenser that illuminates it. The advantage of this approach over transmission, or diascopic, fluorescence microscopes (in which the exciting light comes through the condenser and the emission is collected by the objective) is that whereas the excitation of the fluorophore is equivalent in both epi- and transmitted microscopes, only the small percentage of the exciting light that is reflected off the sample needs to be blocked in the return light path in the epi-illumination mode. The main technical hurdle with this approach is that the exciting light and fluorescence emission overlap in the light path requiring a special kind of beam splitter, a dichroic mirror, to separate the excitation from the emission. The dichroic beamsplitter mirror is designed to be used in light paths at 45°. In ordinary fluorescence microscopes, the dichroic reflects shorter wavelength light originating from the light source and transmits the longer wavelengths of the emitted fluorescence. Each dichroic is designed to have a transition from reflection to transmission that resides between the excitation and emission peaks of the fluorophore it is designed to be used with (Fig. 3b). Dichroics are rarely used without two additional filters: the excitation filter, which preselects the exciting wavelengths, and a barrier filter that only allows passage of the longer wavelength light back to the detector. All three types of filter are typically interference filters which have very specific wavelength selectivity. These are marvels of engineering composed of many stacks of thin materials that alternate in index of refraction (Reichman, J. *Handbook of optical filters for fluorescence microscopy*. Chroma Technology Corp. (http://www.chroma.com/resources/PDF_files/handbook4.pdf; 2000). With these three elements, the exciter, beamsplitting dichroic and barrier, the separation of the exciting light from the emitted light can be very good. For example, a modern filter set might pass only one photon in 10,000 of the wrong excitation color to the specimen, and there is a similar ratio in the return light. Such high ratios are absolutely required for imaging small numbers or single fluorescent molecules.

Filter cubes

Many fluorescence microscopes provide a convenient way of selecting the precise wavelength bands for excitation and emission related to particular fluorophores by means of small block-shaped filter holders that are composed of the exciter, dichroic mirror and barrier filter

BOX 2 FACTORS THAT REDUCE THE QUALITY OF FLUORESCENCE IMAGES

There are many different reasons fluorescence imaging is sometimes not sufficiently good to provide useful data. Many of the issues have been touched upon above. In the following list, we itemize some of the most common factors that decrease the quality of fluorescence imaging and what can be done to improve the situation.

Choice of fluorophore. Maximize the absorption coefficient and quantum yield (http://probes.invitrogen.com/handbook/).

Concentration of the fluorophore. Especially when staining thick tissue blocks, it is sometimes difficult to get sufficient fluorophore inside the block. The potential solution of staining longer or with a higher concentration (for example, of a fluorescent secondary antibody) sometimes does not help as the background increases faster than the signal. Optical sectioning microscopes such as confocal can provide some help by removing background fluorescence from the image. In other cases the epitope or structure being labeled is just in low abundance, so the signal will be intrinsically dim. Brighter signals can be obtained by amplification methods[34].

Excitation intensity. With arc lamps, the brighter the light, the brighter the signal (and background). Unlike with a laser, it is not possible to saturate the fluorescence with an arc. The most intense arcs are the ones with the highest mean luminous density[26].

Arc lamp alignment. If the arc is not focused sharply on the back aperture, the specimen plane will be unevenly illuminated. Ask a microscope company representative to show you how to align and focus the arc. Alternatively, you may consider a liquid light guide–based light source, which provides even illumination and no moving parts to get out of alignment once properly set up.

Wavelength of the exciting light. Another way to increase the intensity of fluorescence is to use a wide-band exciter—in this way more photons that are capable of exciting the fluorophore are impinging on it. Narrow-band exciters are only useful when there is potential cross-talk with another fluorophore (see http://www.chroma.com/ or http://www.omegafilters.com/ for further details).

Emission filters. Broad-band emission will give a larger signal and should always be used except when there is cross-talk with the emission of another fluorophore in the same sample.

NA of the objective. Fluorescence intensity dramatically increases with the objective's NA[26,27]. For low-NA objectives that are used both to illuminate and collect the light (the standard epi-illumination microscope), the amount of light reaching the detector is proportional to $(NA)^4$. For high-NA, the light excitation and collection efficiency is actually a bit better.

Magnification. The magnification of an image spreads the light out and decreases the intensity per pixel in proportion to 1/magnification squared . Sometimes in order to get a high resolution image that matches the optical characteristics of the objective (that is, a diffraction-limited image) with the pixel size of the detector, it is necessary to zoom beyond the magnification of the objective. The price for getting a diffraction-limited image may be a very dim image with insufficient signal to see the resolution. There is no simple solution other than being sure that there is no 'empty' magnification that magnifies more than is necessary to get to twice the diffraction limit (the Nyquist limit). It is worth noting that light loss caused by magnification is not an issue with laser scanning 'zoom', which concentrates more light over a smaller area—but bleaching can be almost instantaneous.

Ionic milieu (quenching). It is worth making sure that iodine and several other metal ions are not contaminating your samples.

Bleaching. Keep samples in the dark when not in use. Use only enough light to get the image you need. Use antifade agents. Keep oxygen tension low.

Background fluorescence. Autofluorescence background is progressively reduced at higher wavelengths. Several companies offer red and infrared dyes to mitigate background problems (Atto fluorophores from Sigma-Aldrich, and Alexa fluors from Molecular Probes). Long-wavelength fluorescence has its own challenges, however[35]. Fixatives often increase autofluorescence. Glutaraldehyde, which is used in electron microscopy fixation, is a great fixative but is totally unusable for fluorescence imaging as the background is huge. Use of 4% or even 2% paraformaldehyde has low autofluorescence and for many applications is often adequate. A simple way to reduce background is to use the field diaphragm on the epi-illumination port (**Fig. 3a**) to limit the illumination to the small region of interest. Sometimes fluorescence that is totally invisible can be revealed by stopping the field aperture to a very small spot. Of course this limits the field of view. The index of refraction mismatch between the immersion medium between the coverslip and the objective versus the sample medium can cause a blurry image with extra background glow owing to spherical aberration. Objectives such as the Leica AS MDW 60×, 1.3 NA that provide the opportunity to use the same proportions of water and glycerol on both sides of the objective can dramatically remove this background artifact.

Light passing properties of optical path. UV dyes are difficult to excite with ordinary glass objectives that are opaque to light <350 nm.

Degradation of fluorophore. If possible, store slide boxes in refrigerator or freezer.

Path length. Blue and near-UV emitting fluorophores are harder to see the deeper they are located within a thick tissue block owing to Rayleigh scattering. Since scattering is inversely proportional to λ^4 a red-shifted dye can help dramatically.

Detector sensitivity. Digital cameras are potentially very useful for detecting signals that seem too dim for the 'naked' eye. Two technical approaches for different applications are available. When exposure time can be long, a cooled charge-coupled device (CCD) is probably the best option. Recent improvements in CCDs make the quantum efficiency very high so that more exotic thinned, back illuminated CCDs are no longer typically required. Large pixel size or binning increases sensitivity further. When the signal needs to be obtained quickly, an intensifier in front of the CCD is the better alternative[26].

Membrane fluorescence optical artifact. The edges of membrane labeled cells that are orthogonal to the image plane are always brighter than membranes parallel to the plane. This artifact is due to the fact that within the optical thickness of an image plane there can be many more fluorescent molecules contributing to a pixel if the membrane is vertical than when the membrane is horizontal.

(Fig. 3b). The cube fits into a circular carousel or linear block that can hold from three to nine separate cubes. These cubes can be moved into position either manually or by a computer driven motor. Thus, to switch between imaging a red fluorescing fluorophore like TRITC, a green fluorescing dye such as fluorescein, and a blue fluorescing dye such as DAPI, is as easy and rapid as moving from one cube to another. One point of caution should be remembered. Because the cubes are not necessarily perfectly aligned (especially the 45° angle of the dichroic), the images with the various cubes may be slightly offset, requiring care when overlapping two images taken with different cubes. The cubes can be selected based on not only spectral matching to particular fluorophores, but also whether they are broad or narrow band. Broad-band cubes attempt to give the largest signal for a dye based on its excitation and emission spectra. Such cubes are preferred when one is looking for a signal from a single dye and you are not concerned with crosstalk. Alternatively, there are many situations in which the location of different fluorophores in the same sample is essential. In these cases, it is useful to use narrow-band cubes. In determining what is the right cube for a particular application the user must have access to the excitation and emission curves of the fluorophore as well as the spectral filtering properties of the three elements of the cube. An example, shown in Figure 3b, is of a cube that is designed to image EGFP.

It is also possible to use a dichroic mirror with filter wheels that rapidly switch between different exciting and barrier filters. This approach offers the user the possibility of rapid switching between fluorescence channels, and the alignment of the images is better because the same dichroic beamsplitter is used for each fluorophore. For this approach, the dichroic mirror must be more sophisticated. One may use a double, triple or even quadruple dichroic; these mirrors selectively reflect the exciting wavelengths for two, three or four fluorophores while at the same time transmitting the fluorescence for each of these dyes. Such dichroics are useful when scanning to find sites of overlap of two different fluorophores or for situations where filter wheels allow rapid switching in the excitation wavelengths. Given the large number of colors that are passed by such cubes, the background may appear more gray than black. Several companies (for example, Omega Optical and Chroma Technology) will even generate custom filter cubes and dichroics if you have a particular unconventional fluorophore.

Light sources

There are several different strategies for fluorescence illumination. Traditionally the intensities needed for comfortable viewing by eye or rapid camera exposure come from arc lamps. Mercury and xenon arc lamps are expensive, potentially dangerous, and require special lamp houses and power supplies. These two types of arc lamps differ in several important ways. Depending on your requirements xenon or mercury is the better choice. Xenon has the advantage of being relatively even in the coverage of wavelengths throughout the UV, visible and near infrared. Mercury, however, is a spectrally peaky light source with several extremely intense lines[26]. If these lines coincide with the excitation spectrum of the fluorophores you are using, it provides brighter light. Mercury is not a good light source for some ratiometric dyes, such as fura 2, for which comparisons between the signal at two nearby excitation wavelengths are confounded by the fact that one of the wavelengths overlaps with a mercury peak but the other does not. With such exceptions in mind, the most intense fluorescence usually comes from the 100-W mercury. The reason why this is the brightest source is that the mean luminous flux per surface area is highest.

Because the image of the arc is focused onto the back aperture of the objective in Kohler-style illumination, the key to bright illumination is the intensity of the image of the arc. The surprising fact is that whereas arcs with higher power (wattage) produce more light, they are larger, and their image needs to be reduced below its actual size to fit in the objective's back aperture, and this minification causes the image to be less intense. For this reason a small highly intense arc provides more intense excitation light.

With time, arcs will not ignite easily owing to blunting of the cathode and anode. The bulb will also begin to show variations in intensity and slight movements in arc position that cause flickering. Thus once a bulb has reached its useable lifetime (200 h for mercury and 400 h for many xenon), the bulb should be replaced. It is also possible for the alignment to drift so that the image of the arc is not centered on the objective's back aperture, requiring adjustment of the alignment every week or so. This requires setting a number of adjustments on the lamp house and requires a bit of practice, but ignoring this step will lead to uneven illumination and often unacceptably dim images.

The most even illumination comes when a sharp image of the arc is placed on the back aperture of the objective lens. Although this sharp image means that there will be regions without light, that absence only has the effect of removing some potential angles of illumination of the specimen. Because fluorescence emission is typically not sensitive to the angle of illumination, the inhomogeneity in the angles of illumination is invisible. Conversely, when the arc is not well focused on the back aperture there can be inhomogeneities in the intensity at various positions on the sample. This artifact causes brighter and dimmer fluorescence within the image. Recently these issues have been tackled by the development of liquid light guides coupled to new ultrahigh pressure 120-W mercury halide bulbs similar to those used in LCD projectors. Some of these systems have been specifically developed for fluorescence microscopy illumination (for example, X-Cite 120 from Exfo Photonic Solutions). The emission spectra of these bulbs are similar to traditional mercury arc lamps but have some additional spectral broadening owing to the high-pressure collisions that alter the vibrational energy of the excited atoms in the arc. This broadening, especially in the fluorescein excitation region, makes these bulbs superior to traditional mercury arcs. Such systems, although expensive, provide much longer time between arc replacement (>1,000 h versus 200 h), the convenience of not having the lamp house attached directly to the microscope, no alignment problems and uniform illumination in the microscope field. The recent development of bright light–emitting diodes (LEDs) raises the possibility that arc lamps will someday be replaced by these lightweight, inexpensive light sources.

Objectives

Because the microscope objective is both the source of light that excites the fluorescence in the specimen and the optical element that collects the fluorescence, its properties have a large impact on the fluorescence image. The design of objectives is beyond our scope and is nicely described in other reviews[27]. It is important, however, to understand that because the design of microscope objectives has in the past centered on features that improve the quality of brightfield color images, much effort has been put into correcting chromatic aberrations. These corrections are somewhat less important to the fluorescent microscopist who is more typically concerned with excitation and collection efficiency, resolution, and contrast.

The ideal fluorescence microscope objective has a high numerical aperture (NA). The NA of an objective is a critical parameter and can be found on the barrel of the objective. It is more important than the magnification, as it sets both the resolving power and light efficiency of the objective. The value of the NA is derived by multiplying the sine of the 'half angle' (the angle between the vertical and most extremely angled ray that can be collected by the objective) with the index of refraction of the medium between the objective and the coverslip. The larger the half angle, the greater number of photons that can be collected and the greater the amount of light that can be used to excite the specimen. For this reason the amount of exciting light through an objective is roughly proportional to $(NA)^2$, and at the same time the amount of the fluorescence emission collected is also proportional to $(NA)^2$. The intensity observed is thus proportional to the $(NA)^4$. In addition, oil immersion lenses (in which the oil matches the index of refraction of the coverslip) prevent light losses owing to reflections and refraction off the coverslip and thus improve excitation and collection efficiency. Image intensity is also related inversely to magnification squared, so the most intense images will come from relatively low magnifications. High NA also increases the resolving power of the objective. The minimal resolvable distance is $0.61\ \lambda$ / NA. Additionally, the ideal fluorescence objective will have relatively few lens elements to reduce losses owing to reflection and glare from stray light. The lens elements and cements ideally have very low intrinsic fluorescence so the field appears absolutely black in the absence of fluorescence signal. Lastly, the ideal fluorescence objective will pass exciting wavelengths in the UV, visible and near infrared. All of this information is available (albeit, with some digging) from manufacturers.

It is fair to say that objectives designed particularly for the special needs of the fluorescence microscopist are becoming more common but that no objective is ideal in all circumstances. Users whose samples are thick may want to consider lenses that also have a correction collar for spherical aberrations, as these aberrations cause blurring and loss of contrast when samples have a different index of refraction than the material between the coverslip and the objective. If one is routinely dealing with thin sections, one may want a 'plan' lens that images a flat field in the specimen—otherwise the edges may be blurry. If the main aim is perfect alignment between blue, green and red fluorescent material in one sample plane, an apochromatic lens should be considered. It is appropriate to try out an expensive objective on your own sample before purchase to make sure it provides the kind of image you are expecting.

BLEACHING

The phenomenon of bleaching

Although in principle a fluorophore can cycle between ground and excited states an unlimited number of times, the conditions in which organic fluorophores are used usually limit the number of cycles. Estimates of 10,000–40,000 cycles are often cited as the limit before permanent bleaching occurs for good fluorophores. Bleaching is a generic term for all of the processes that cause the fluorescent signal to fade permanently. Quenching on the other hand, is a reversible loss of fluorescence owing to noncovalent interactions between a fluorophore and its molecular milieu. FRET, mentioned above, is an example of collisional or dynamic quenching of the excited state fluorophore. Static quenching occurs when the ground-state fluorophore associates with another molecule (sometimes other identical fluorophores: self-quenching).

At the molecular level there are several different ways bleaching can occur, and it is fair to say that the photochemistry is not well worked out for most fluorophores. What is clear is that the long-lived triplet state provides more opportunities for a molecule with an excited electron to interact with other molecules than the briefer singlet states. Hence, most bleaching is thought to be associated with triplet states. It also appears that one of the important ingredients in bleaching is an interaction between a triplet state fluorophore and molecular oxygen. The triplet state can transfer its energy to oxygen (which is itself a triplet in the ground state), exciting oxygen to its singlet excited state. Singlet oxygen is a reactive molecule that can participate in may kinds of chemical reactions with organic molecules. These chemical reactions can covalently alter the fluorophore to inactivate its ability to fluoresce (that is, bleaching it). In addition, the singlet oxygen can interact with other organic molecules causing phototoxicity for living cells.

Dealing with bleaching

There are many reasons why fluorescence signals are not as bright as one might hope (see Box 2 for a list of problems and potential solutions), but bleaching is perhaps the most serious. One way to reduce bleaching is to use no more light than absolutely necessary to image a sample. If the microscope has an aperture diaphragm on the epi-illumination port (Fig. 3a), use it to titrate the light level to a low value. The field diaphragm can also be stopped down to illuminate only a small region to minimize general bleaching and also improve contrast. In fixed samples, the amount of bleaching appears to be directly related to the number of excitation emission cycles a fluorophore goes through, so dim light does not automatically eliminate bleaching. Slides that contain fluorescence samples should therefore always be stored in the dark when not in use because ambient light of long enough duration can bleach them.

It is important to realize that fluorophores with similar excitation and emission spectra can have dramatically different bleaching rates. Companies, like Invitrogen's Molecular Probes or Sigma-Aldrich, sell new-generation fluorophores that have greater photostability than previous well-known dyes such as fluorescein, rhodamine and Texas red. The Alexa dyes are one such example (Fig. 2), with bleaching rates that are several-fold slower than older dyes[28]. Not surprisingly, the relative lack of bleaching of newer fluorophores comes with another benefit; their intensity is high owing to their high quantum yield because efficient fluorescence emission antagonizes the tendency of molecules to end up in the triplet state.

Unfortunately even with the best dyes, it is sometimes necessary to use intensities that will cause bleaching, as for example when taking an image with a camera or prolonged time lapse imaging. In fixed samples, immersing a sample on a slide with a mounting medium that is designed to reduce bleaching is an effective strategy. A number of antifade agents can be made up in the lab rather inexpensively or purchased ready to use. All of these are designed only for fixed specimens for which there are a variety of options[29]. *p*-Phenylenediamine is very effective for FITC and rhodamine, but discolors with exposure to light, so slides must be stored in a dark container. Also, it is a reactive chemical that needs to be used with care to minimize contact[30]. DABCO ('Slow Fade' is the commercial version from Molecular Probes) is a bit less effective but has greater light resistance and less toxicity[31]. *N*-propylgallate is better than the previous two for rhodamine[32]. In addition, there are several proprietary antifade mounting media (Vectashield from Vector Labs, ProLong Gold from Molecular Probes).

It is worth emphasizing that not all dyes are equally susceptible to all anti-fade agents. An agent that works quite well for one dye may be almost useless for another, whereas the reverse may be true for another antifade agent. All of these antifade mountants typically contain a water-glycerine mix plus a chemical designed to reduce fading by reducing the generation of singlet oxygen or its lifetime. The water glycerin mix has a refractive index that is between water and oil. Thus several companies are now making objectives for immersion media between the objective and the coverslip to match the refractive index of the mountant on the other side of the coverslip. Index matching mitigates spherical aberration in the sample images. For living specimens, antifade agents are still not perfected although ascorbic acid, vitamins C and E, beta-carotene and low oxygen tension might provide some relief.

In all imaging applications, high-quality optical filters that provide efficient passage of all or nearly all of the emitted wavelengths can also decrease the bleaching. Use of fast film or cameras with high quantum efficiency or low noise allow for shorter exposures and less bleaching[14,26]. Of course, fluorescent probes that don't bleach would be the best solution. This seemingly unlikely proposition has now been realized with the development of Quantum dots[33]. These complex three-layered nanocrystals use cadmium salt semiconductors as the equivalent of the fluorophore. The outer shell of the dot provides a convenient chemical substrate to attach the dots to biological ligands like avidin. They have many remarkable properties both in terms of an enormous range of absorption and wavelengths based in part on the particular cadmium salt and partly on their size. Because they can be small (nanometers) they are useful for a variety of labeling techniques. Their resistance to bleaching also makes them ideal for single molecule detection.

CONCLUSIONS

The use of fluorescence to probe biological phenomena is rapidly expanding into all fields of cell and molecular biology. The underlying principles in photophysics and chemistry that underlie fluorescence and fluorophores may seem far removed from biology but understanding them are central to good fluorescence microscopy. Moreover, many new modalities such as confocal, multiphoton, stimulated emission depletion (STED), structured illumination, total internal reflection fluorescence (TIRF), FRET, FLIM, fluorescence recovery after photobleaching (FRAP) and fluorescence correlation spectroscopy (FCS). Lastly, the genetic engineering of fluorescent proteins to monitor living cellular activities is among the most powerful new windows into biology. Thus for the foreseeable future, biology and fluorescence will be deeply intertwined.

COMPETING INTERESTS STATEMENT

The authors declare that they have no competing financial interests.

Published online at http://www.nature.com/naturemethods/
Reprints and permissions information is available online at http://npg.nature.com/reprintsandpermissions/

1. Tsien, R.Y. The green fluorescent protein. *Annu. Rev. Biochem.* **67**, 509–544 (1998).
2. Valeur, B. *Molecular Fluorescence: Principles and Applications.* (Wiley-VCH, Weinheim, 2002).
3. Lakowicz, J.R., ed. *Principles of Fluorescence Spectroscopy*. 2nd ed. (Plenum Press, New York, 1999).
4. Turro, N.J. *Modern Molecular Photochemistry*. (University Science Books, Sausalito, California, 1991).
5. Irvine, D.J., Purbhoo, M.A., Krogsgaard, M. & Davis, M.M. Direct observation of ligand recognition by T cells. *Nature* **419**, 845–849 (2002).
6. Wang, L., Jackson, W.C., Steinbach, P.A. & Tsien, R.Y. Evolution of new nonantibody proteins via iterative somatic hypermutation. *Proc. Natl. Acad. Sci. USA* **101**, 16745–16749 (2004).
7. Deerinck, T.J. *et al.* Fluorescence photooxidation with eosin: a method for high resolution immunolocalization and in situ hybridization detection for light and electron microscopy. *J. Cell Biol.* **126**, 901–910 (1994).
8. Suhling, K., French, P.M. & Phillips, D. Time-resolved fluorescence microscopy. *Photochem. Photobiol. Sci.* **4**, 13–22 (2005).
9. Elson, D. *et al.* Time-domain fluorescence lifetime imaging applied to biological tissue. *Photochem. Photobiol. Sci.* **3**, 795–801 (2004).
10. Jares-Erijman, E.A. & Jovin, T.M. FRET imaging. *Nat. Biotechnol.* **21**, 1387–1395 (2003).
11. Mizuno, H. *et al.* Photo-induced peptide cleavage in the green-to-red conversion of a fluorescent protein. *Mol. Cell* **12**, 1051–1058 (2003).
12. Ando, R., Hama, H., Yamamoto-Hino, M., Mizuno, H. & Miyawaki, A. An optical marker based on the UV-induced green-to-red photoconversion of a fluorescent protein. *Proc. Natl. Acad. Sci. USA* **99**, 12651–12656 (2002).
13. Mason, W.T., ed. *Fluorescent and Luminescent Probes for Biological Activity: A Practical Guide for Quantitative Real-Time Analysis.* (Academic Press Harcourt Brace and Co., Boston, 1993).
14. Periasamy, A., ed. *Methods in Cellular Imaging* (Oxford University Press, Oxford, 2001).
15. Rudolf, R., Mongillo, M., Rizzuto, R. & Pozzan, T. Looking forward to seeing calcium. *Nat. Rev. Mol. Cell Biol.* **4**, 579–586 (2003).
16. Tsien, R.Y. Fluorescent indicators of ion concentrations. *Methods Cell Biol.* **30**, 127–156 (1989).
17. Bassnett, S., Reinisch, L. & Beebe, D.C. Intracellular pH measurement using single excitation-dual emission fluorescence ratios. *Am. J. Physiol.* **258**, 171–178 (1990).
18. Yuste, R. & Konnerth, A., eds. *Imaging in Neuroscience and Development: A Laboratory Manual*. (Cold Spring Harbor Laboratory Press, New York, 2005).
19. Zhang, J., Campbell, R.E., Ting, A.Y. & Tsien, R.Y. Creating new fluorescent probes for cell biology. *Nat. Rev. Mol. Cell Biol.* **3**, 906–918 (2002).
20. Griesbeck, O. Fluorescent proteins as sensors for cellular functions. *Curr. Opin. Neurobiol.* **14**, 636–641 (2004).
21. Ohmichi, T. *et al.* DNA-based biosensor for monitoring pH *in vitro* and in living cells. *Biochemistry* **44**, 7125–7130 (2005).
22. Grinvald, A. & Hildesheim, R. VSDI: a new era in functional imaging of cortical dynamics. *Nat. Rev. Neurosci.* **5**, 874–885 (2004).
23. Kuhn, B., Fromherz, P. & Denk, W. High sensitivity of Stark-shift voltage-sensing dyes by one- or two-photon excitation near the red spectral edge. *Biophys. J.* **87**, 631–639 (2004).
24. Reiff, D.F. *et al.* In vivo performance of genetically encoded indicators of neural activity in flies. *J. Neurosci.* **25**, 4766–4778 (2005).
25. Goldman, R.D. & Spector, D.L., eds. *Live Cell Imaging: A Laboratory Manual.* (Cold Spring Harbor Laboratory Press, New York, 2004).
26. Inoué, S. & Spring, K.R. *Video Microscopy*. 2nd edn. (Plenum Publishing, New York, 1997).
27. Abramowitz, M., Spring, K.R., Keller, H.E. & Davidson, M.W. Basic principles of microscope objectives. *Biotechniques* **33**, 772–781 (2002).
28. Panchuk-Voloshina, N. *et al.* Alexa dyes, a series of new fluorescent dyes that yield exceptionally bright photostable conjugates. *J. Histochem. Cytochem.* **47**, 1179–1188 (1999).
29. Ono, M. *et al.* Quantitative comparison of anti-fading mounting media for confocal laser scanning microscopy. *J. Histochem. Cytochem.* **49**, 305–331 (2001).
30. Johnson, G.D. & Nogueira Araujo, G.M. A simple method of reducing the fading of immunofluorescence during microscopy. *J. Immunol. Methods* **43**, 349–350 (1981).
31. Johnson, G.D. *et al.* Fading of immunofluorescence during microscopy: a study of the phenomenon and its remedy. *J. Immunol. Methods* **55**, 231–242 (1982).
32. Giloh, H. & Sedat, J.W. Fluorescence microscopy: reduced photobleaching of rhodamine and fluorescein protein conjugates by n-propyl gallate. *Science* **217**, 1252–1255 (1982).
33. Alivisatos, A.P., Gu, W. & Larabell, C. Quantum dots as cellular probes. *Annu. Rev. Biomed. Eng.* **7**, 55–76 (2005).
34. van Gijlswijk, R.P. *et al.* Fluorochrome-labeled tyramides: use in immunocytochemistry and fluorescence *in situ* hybridization. *J. Histochem. Cytochem.* **45**, 375–382 (1997).
35. Cullander, C. Imaging in the far-red with electronic light microscopy: requirements and limitations. *J. Microsc.* **176**, 281–286 (1994).

Optical sectioning microscopy

José-Angel Conchello[1,2] & Jeff W Lichtman[3]

Confocal scanning microscopy, a form of optical sectioning microscopy, has radically transformed optical imaging in biology. These devices provide a powerful means to eliminate from images the background caused by out-of-focus light and scatter. Confocal techniques can also improve the resolution of a light microscope image beyond what is achievable with widefield fluorescence microscopy. The quality of the images obtained, however, depends on the user's familiarity with the optical and fluorescence concepts that underlie this approach. We describe the core concepts of confocal microscopes and important variables that adversely affect confocal images. We also discuss data-processing methods for confocal microscopy and computational optical sectioning techniques that can perform optical sectioning without a confocal microscope.

One problem with fluorescence microscopy is that, regardless of where the microscope is focused vertically in a specimen, illumination causes the entire specimen thickness to fluoresce. Thus, it is not unusual that in a given two-dimensional (2D) image more than 90% of fluorescence is out-of-focus light that can completely obscure the in-focus detail and greatly reduce the contrast of what remains. For example, a fluorescent cell might be 5 to 15 μm thick, whereas the depth of focus (that is, thickness of the imaging plane) of a high numerical aperture (NA) objective (NA ≥ 1.3) is only about 300 nm or less. Thus the vast majority of the cell volume is out of focus. In addition to light that is out of focus the contrast in fluorescence images is adversely affected by scatter. Scattered light comes from fluorescent emission that may be diffracted, reflected and refracted by the specimen on its way to the objective lens and thus it appears to have been emitted from the last point of scattering and not from the actual location of the fluorophore that emitted it. Because imaging deeper into the specimen increases the chances of scatter, more light will appear to be coming from planes closer to the surface of the specimen than from those deeper inside it, thus producing an image that is more consistent with a specimen preparation in which the concentration of fluorescent dye decreases with specimen depth.

A general approach to improve this problem is to use techniques capable of optical sectioning. Confocal scanning microscopy is presently the most widely used optical sectioning technique for fluorescence imaging, whereas computational optical sectioning techniques allow sectioning using a conventional widefield fluorescence microscope. Multiphoton fluorescence excitation microscopy is an important and very powerful technique for optical sectioning microscopy. This technique is described in detail elsewhere[1], and thus we will not cover it here.

CONFOCAL MICROSCOPY

Optical sectioning acquires images of thin slices of a thick specimen by removing the contribution of out-of-focus light in each image plane. This removal of unwanted light provides greater contrast and permits three-dimensional (3D) reconstructions by computationally combining the image data from a stack of images. Confocal scanning microscopy has an added benefit too: the in-plane or *x-y* resolution of the image can be improved beyond what is possible with conventional widefield fluorescence microscopy. Whereas confocal microscopy can

[1]Molecular, Cell, and Developmental Biology, Oklahoma Medical Research Foundation, Oklahoma City, Oklahoma 73104, USA. [2]Program in Biomedical Engineering, University of Oklahoma, Norman, Oklahoma 73019, USA. [3]Molecular and Cell Biology Department, Harvard University, Cambridge, Massachusetts 02138, USA. Correspondence should be addressed to J.-A.C. (jose-conchello@omrf.ouhsc.edu).

PUBLISHED ONLINE 18 NOVEMBER 2005; DOI:10.1038/NMETH815

be implemented in many different ways, all of the approaches are based on the same concept. This idea was first described in a patent application by M. Minsky[2] and subsequently described by him in a delightful memoir[3]. Minsky, who is perhaps better known as the founder of the field known as artificial intelligence, as a young man built a confocal microscope to improve reflected-light images of brains in which the Golgi apparatus was stained in hopes of seeing more clearly the connections within a thick tissue block. Whereas his design and theoretical analysis was exactly correct, there was little interest in his idea at the time. He never published a paper using the technique and received no royalties over the 17-year life of the patent.

Subsequent rediscoveries of the confocal idea have led to two rather different implementations, those in which an optical image is directly formed in the retina, film or camera faceplate, and those that must make the images electronically. All confocal techniques, however, share the same fundamental attribute: they are scanning microscopes. 'Scanning' means that the image of each section is built up by adding information from regions that are sampled in sequence. The main drawback of scanning is that image acquisition is not as rapid as wide-field techniques in which the entire image is acquired simultaneously. Thus some implementations aim to speed the process with some potential loss of quality. Other confocal techniques are slower but in principle do not sacrifice any of the potential benefits.

In all confocal microscopes the central concept is to do two things simultaneously (Fig. 1): scan the image by illuminating individual regions in sequence (scanning the illumination) and at the same time mask all but the illuminated regions from providing return light to the detector (scanning the detection). The magnitude of the confocal improvement is inversely related to the size of the region(s) that are sampled at any one moment. To explain why this small scan area is necessary and why the dual scan approach is so effective, we need to dissect the two scanning processes.

CONFOCAL PRINCIPLES

Scanning the illumination and detection

A confocal microscope illuminates one region after another until the whole field of view is sampled. In most confocal microscopes the aim is to illuminate with light that is focused to the very small-

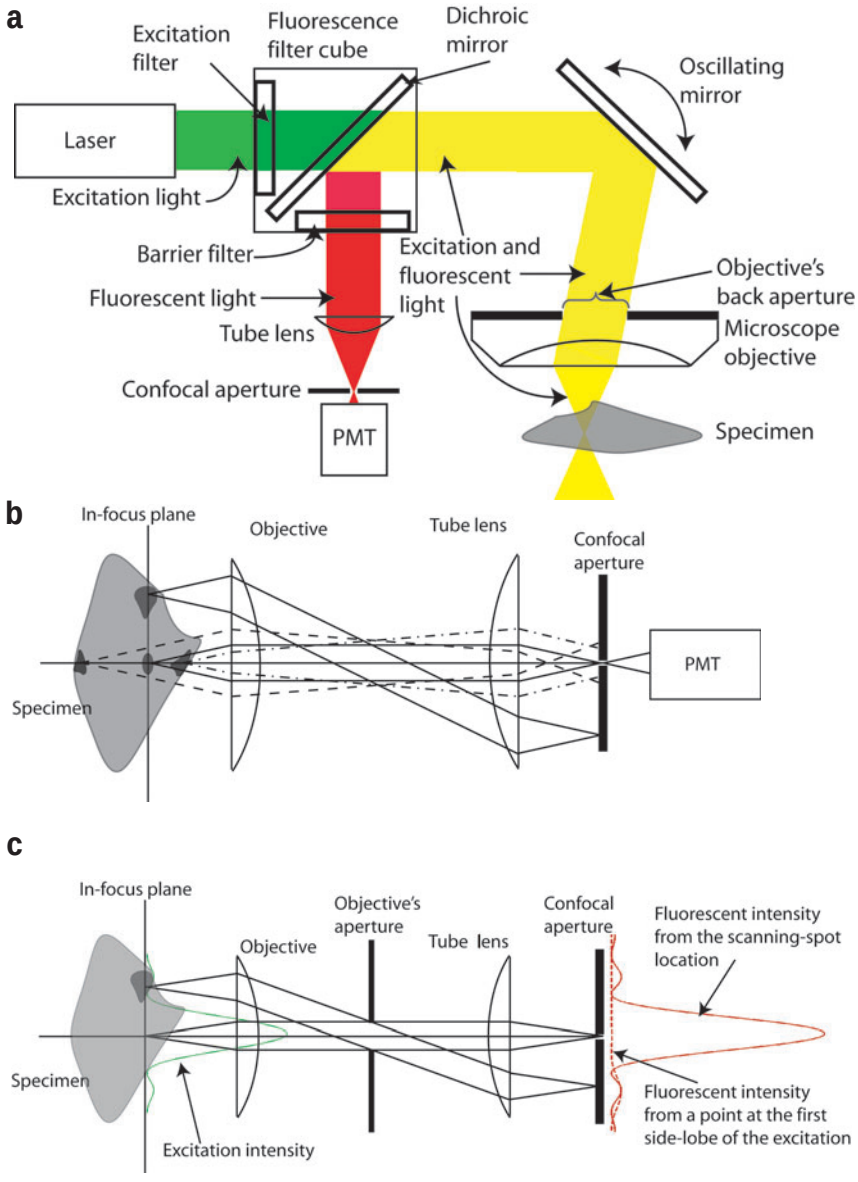

Figure 1 | The confocal principle. (**a**) Layout of the confocal microscope. The excitation light is directed by the scanning mirror and focused into the specimen. The fluorescent emission is separated from the excitation by the dichroic mirror and the barrier filter. Light emitted from the location of the scanning spot goes through the pinhole in front of the detector. (**b**) Path of the fluorescent light with the excitation and scanning not shown. The scanning spot is at the center of the in-focus plane. Light emitted from the in-focus plane (solid lines) is focused into the image plane where the confocal pinhole aperture is located. Light not emitted from the location of the scanning spot focuses on the opaque portions of the pinhole aperture and thus does not reach the PMT detector. Out-of-focus light emitted from points deeper (dashed line) or less deep (dash-dot line) than the in-focus plane come to focus in front or behind the aperture plane, respectively, and thus only a small portion of this light passes through the pinhole aperture. (**c**) The scanning spot (green intensity profile) excites fluorescence. Fluorescent molecules at the location of this spot emit strongly and produce an Airy diffraction pattern at the plane of the confocal pinhole (red solid-line profile), whereas molecules away from this spot weakly fluoresce producing a dimmer Airy diffraction pattern whose peak intensity does not coincide with the pinhole aperture (red dashed-line profile) and, furthermore, their peak intensity does not coincide with the pinhole aperture. As a result, the fluorescence detected from these spots is greatly reduced relative to that coming from the location of the scanning spot.

est spot possible in the plane of focus. This diffraction-limited spot of illumination is created by sending a collimated plane wave into the back of the objective where it is transformed into a converging spherical wave by the lens. Thus the full NA of the lens (Fig. 1a) is used to focus the light sharply at a single point at the so-called 'waist' of an hourglass-shaped beam. A laser beam is an ideal light source for this task as it contains all of its energy in a collimated coherent plane wave. In the absence of scattering, the cone of light will focus to its narrowest at the waist of the hourglass-shaped beam (Fig. 2), but because of diffraction, the cone will not evenly illuminate the specimen. This distribution is called the point spread function (PSF) because the image of a small luminous point-object has the exact same pattern. The higher the NA and the shorter the wavelength, the smaller the beam waist will be (diameter = 1.22 λ/ NA, where λ is the wavelength of the excitation light). If the specimen does not absorb light as it passes through the sample, the total amount of illumination is of course the same in all levels of the sample. As the light travels to the waist of the beam, the same amount of light is concentrated into a smaller area, thus the irradiance increases and is highest at the waist. This form of illumination does not selectively illuminate the plane of interest or prevent scattering. Thus, scanning the illumination is insufficient to remove unwanted light, and it is necessary to add some mechanism by which light from out-of-focus sources does not reach the detector. This is achieved by placing a pinhole aperture in front of the detector at a plane that is conjugate to the in-focus plane, such that the illumination spot and the pinhole aperture are simultaneously focused at the same spot (Fig. 1a). Because this microscope requires scanning the illumination spot and having this spot always remain in focus with the pinhole aperture, the instrument is called a confocal scanning microscope (CSM).

Effect on contrast

A measure of the contrast in an image is given by the brightness difference between the signal and the background relative to the background brightness. In widefield fluorescence microscopy the specimen is being illuminated by light converging at every spot in the focal plane simultaneously, and this induces two kinds of background that lower contrast: scatter within the plane of focus and contributions of out-of-focus fluorescence to the in-focus image. Excessive background is the bane of many microscope images. These sources of background are largely removed by confocal imaging.

To get a better idea of how these sources of background arise and why confocal microscopy eliminates them, it is useful to think about what happens with illumination of a single spot with one focused converging spherical wave. In the plane of focus where the light is most intense, some of the exciting light is scattered by particles in the specimen to excite fluorescence out of the region where the focused spot is. This gives a glowing cloud of fluorescence excitation around the waist of the beam. In addition, the return light is scattered on its way out of the tissue, making a fuzzy image of the spot that has the brightest fluorescence. Above and below the plane of focus, the exciting light is less intense but covers a wider area. The net effect is that a uniformly fluorescent sample with negligible absorption and scattering will have the same amount of fluorescence excitation at all depths. Because all but one of these depths is out of focus, the fluorescence from these planes appears as a diffuse background. Scattering in these other planes only makes matters worse. If the sample is thick, the vast majority of the fluorescence signal elicited by illuminating a spot comes from the out-of-focus components.

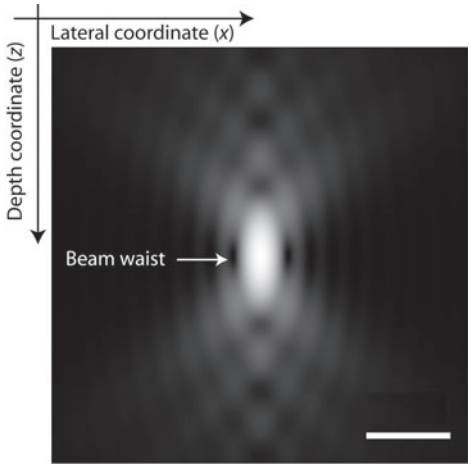

Figure 2 | The PSF. Light distribution near the location of the confocal scanning spot for a 100×, 1.4 NA oil-immersion lens and an excitation wavelength of 530 nm (brightness in log-scale with three decades). Bar, 0.5 μm.

So how can all this background be removed? In the CSM, the pinhole in front of the detector allows the light from the focused spot to reach a detector on the other side of the pinhole (Fig. 1b). At the same time, the pinhole rejects the scattered halo of light around the illuminated spot. It also rejects much, although not all, of the out-of-focus light collected by the objective. This light either is focused before reaching the plane of the pinhole and thus has re-expanded at the pinhole plane, or is on its way to converging to a focused spot but is largely blocked by the pinhole. The pinhole's effectiveness is clearly related to its size, and it might seem that the background would become infinitesimal when the pinhole is very small—even smaller than the projected image of the diffraction-limited spot. The loss of signal, however, eventually outpaces the loss of background, so the optimal pinhole size is between 60% and 80% of the diameter of the diffraction-limited spot[4,5].

The pinhole has no effect at rejecting out of focus background when the sample is illuminated all at once rather than by an hourglass shaped beam because in this case out of focus light getting through the pinhole is no less intense than the in-focus light. The image will be identical to that seen in a widefield fluorescence microscope.

As a result of the selective illumination with an hourglass-shaped beam of only one spot in the plane of focus and an aligned pinhole in a conjugate image plane in the return light path, the light originating from one spot in one plane is selectively detected. This provides excellent contrast because if the exciting light is focused on a spot that does not contain any fluorophores, the detector sees a dark area, and if it contains fluorophores, it sees the light emitted from those fluorophores only. Of course the arrangement just described would only provide the light from one spot. To make an image the scope needs to sample each spot on the specimen plane the same way (the scanning methods for doing this are described below). The accumulated result is a dramatic improvement in contrast and a thin optical section.

Effect on resolution

An important but rarely used property of the CSM is its ability to improve the resolving power of a microscope beyond what is

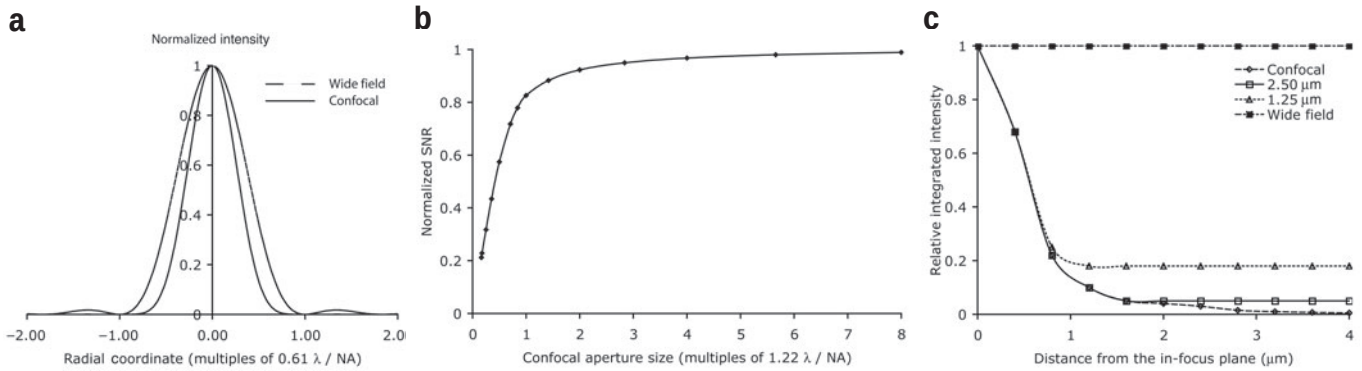

Figure 3 | PSF, SNR and background rejection. (**a**) PSF of the wide-field and confocal microscopes. (**b**) SNR in the confocal microscope with finite aperture normalized such that with a fully open–aperture SNR = 1. (**c**) Background rejection in multiple-aperture confocal scanning microscopy. Graph of overall intensity due to a horizontal thin layer of fluorescence as a function of the distance from focus. For the wide-field microscope the intensity does not change with the distance from the in-focus plane. For the single-aperture confocal microscope it decreases in inverse proportion to the square of the distance from focus. The spinning-disk confocal microscope shows a hybrid behavior. Close to the in-focus plane, the intensity decreases as in the confocal microscope. At more distant planes, the intensity remains constant as in the wide-field microscope. The figure shows this behavior for apertures that are 1.25 μm and 2.5 μm apart (when projected to the specimen). The further apart the apertures are, the stronger the background rejection.

achievable with even the highest-NA objectives. This improvement only occurs if the pinhole is stopped down below the size of the central disk of the Airy pattern (< 1.2 λ / NA). To understand why this improvement occurs, consider a confocal beam scanning across a very small fluorescent bead that is itself smaller than the diffraction-limited spot of the scanning beam. The beam itself will project an Airy pattern onto the specimen plane, which in the focal plane will appear as a center bright disc surrounded by concentric rings of progressively lower intensity. As this light approaches the small bead, the first interaction will be between a segment of an outer ring of the illumination spot and the bead. This will give rise to very weak excitation of the bead, whose dim image (also an Airy pattern) will be projected to the site of the pinhole aperture. The pinhole is always aligned with the center of the illumination Airy pattern so only a portion of an outer ring of the image of the bead will be passed through the aperture (Fig. 1c). Given that the bead is being weakly excited and only a small part of the emission is being collected, only an extremely dim part of the fluorescence emitted by the bead will be collected at this point. As the illumination beam moves closer to the bead, the intensity of the excitation of the bead increases and the collection is now from a region of the bead's Airy pattern that contains more emitted light. Finally, when the Airy pattern of the illumination coincides with the bead, the brightest part of the illumination excites the bead, and the brightest part of the emission is collected through the pinhole. The result is that the scanning and pinhole aperture in combination attenuate the Airy pattern of the bead image so that more of the detected intensity is related to the actual position of the bead and not the side rings, which are typically no longer detectable. In addition, the intensity distribution of the central Airy disc is also narrowed for the same reason. In more technical terms, the PSF of the confocal microscope is the product of the PSFs of the objective lens at the excitation and emission wavelengths.

The effect of reducing the rings and also the central disc is that beads that are close together are more easily resolved. In Figure 3a we plotted the intensity profile of the in-focus PSF of a conventional and a confocal scanning microscope. Because the PSF of the confocal microscope is 'pushed down' relative to the PSF of the wide-field-illumination microscope, the PSF is also narrower. This means that the two-point resolution of the CSM is approximately 1.4× better than in a wide-field microscope.

One question that confronts all users of laser scanning confocal microscopes is what is the appropriate size of the pinhole aperture, an easily adjusted parameter in all commercial devices. Based on experimental and theoretical measures of the signal-to-noise ratio (SNR) and optical sectioning (Fig. 3), it is clear that there is a substantial gain in SNR by opening the pinhole aperture to be about the size of the projected image of the diffraction-limited spot (1.22 λ / NA) with little degradation of the depth discrimination[4]. But further increasing the aperture radius marginally increases the SNR but drastically reduces the depth discrimination power of the microscope. The actual optimal size of the pinhole will depend on the magnification of the objective and any relay optics in the path. For example, the optimal pinhole sizes for a 100×, 1.4 NA and a 60×, 1.4 NA objective are in a ratio of 100:60. For the former, the optimal pinhole size is 1.67 times larger than for the latter. In some laser confocal microscopes, the software will give you information about the pinhole diameter in Airy units, with 1 unit being the diameter of the Airy disk. In others, the numbers are measured in millimeters or in arbitrary units, making it a bit more difficult to know exactly what the size is relative to the diameter of the Airy disc requiring you to ask the technical staff of the manufacturer what is the relation for their microscope. This is an important variable and definitely worth knowing.

CONFOCAL SCANNING IMPLEMENTATIONS

Specimen scanning versus illumination scanning

Thus far we have not mentioned how scanning the illumination and collection is achieved. One simple albeit impractical solution is to align the focused light source and the pinhole on the same spot and then raster scan the specimen by moving it with a motorized stage. Whereas such a scheme is used in certain industrial settings, biological samples, especially living ones, will not tolerate the shaking from fast scanning. The main advantage of specimen scanning is that it

avoids off-axis aberrations and thus can be used with a variety of objectives, including those that are not 'plan' and thus suffer from field curvature. In confocal implementations for use in biology, however, the illumination is scanned while the specimen remains still. In illumination scanning, the scanning spot is typically moved in a raster-scan fashion over the specimen. The illumination-scanning mechanism is often away from the stage and thus its vibration, if any, does not affect the location of the specimen relative to the objective. There are several different approaches for illumination scanning. In all implementations, however, if the lens suffers from off-axis aberrations (astigmatism, coma and field curvature), this will degrade the image. Specifically, coma spreads the excitation light away from the location of the aberration-free scanning spot, thus decreasing the amount of fluorescence from this location that reaches the detector. Astigmatism and curvature both move the scanning spot away from the nominal plane of focus, thus exciting light that would otherwise be out of focus.

Laser scanning

The most common method for illumination scanning used by the first commercial CSM designed at the MRC (Biorad MRC 600), and still used today, is based on using two oscillating mirrors to deflect the angle of the light beam going into the specimen (called scanning) and deflecting the angle of emitted light in the return light path (called descanning). One mirror scans the illumination and detection along the 'fast axis' (for example, the horizontal direction), and the other mirror scans the 'slow axis' (for example, the vertical direction). This process continues until an entire 2D image is collected, and it can be repeated at the same focus to generate a time series of images or the focus can be vertically stepped up or down to generate a 3D image stack. The speed of this method is limited by the mechanical characteristics of the fast-axis mirror. It is difficult to drive this mirror to oscillate fast enough to scan at video rates: 30 frames per second, at 512 lines per frame, means that the mirror has to oscillate at $30 \times 512 = 15{,}360$ times per second. It is possible to achieve close to video-rate scanning by using 'resonant' oscillating mirrors (see below). In addition to the mechanical limitation, the time the scanning spot dwells over a pixel is a limitation of the CSM. If a 512×512 image is collected in one second, it means that the spot dwells for $1\ s / (512 \times 512) \approx 4\ \mu s$ on each pixel, although it is possible to scan substantially faster ($<<1\ \mu s$ per pixel). In reference 6, it is calculated that to excite detectable fluorescence in such a short time with a typical sample, it is necessary to deliver about 80 microWatt (μW) of light to each pixel. For brightly fluorescent samples less power can be used, but this still requires laser illumination.

The slow acquisition time derives from the fact that the laser scanning approach builds an image sequentially one pixel at a time. The detector is typically a photomultiplier tube (PMT), which has low noise and a fast response. PMTs are ideal for detecting weak signals, even single photons. Unfortunately PMTs are not very efficient. They detect 10% or less of the fluorescence signal that gets through the pinhole. Thus as scanning speeds increase, the number of detected photons per pixel may drop to such a low number that noise from the PMT will limit the quality of the image. Slow scanning speed is not only an inconvenience, but it also limits the utility of the instrument, especially when rapidly changing signals are being studied. In some cases users do 'line scans' to essentially bypass the slower 2D image for the more rapid speeds possible by using just the fast-scan mirror.

Spinning-disk

One way to decrease the scan time without compromising the SNR is to multiplex: illuminate several pixels simultaneously and collect light from all of them at the same time. One successful method is to use a disc with a series of pinhole apertures. Each aperture illuminates a different spot on the specimen and the emitted fluorescence is then focused onto another pinhole aperture on the disk[7,8] or through the same one[9,10]. In the most common form, the fluorescent image of the illuminated spots coincide with the location of the pinholes on the disk, thus the pinholes serve both to focus spots of light on the specimen and also as the confocal pinholes. The light that passes through the apertures is then imaged on a detector. In this case the detector is either the retina or a camera, typically a charge-coupled device (CCD) or intensified CCD camera. The arrangement of the pinhole apertures over the disk is such that as the disk rotates, the illumination spots scan the entire field of view of the microscope.

A notable advantage of the spinning-disk CSM is that, because many spots can be illuminated simultaneously (typically hundreds or more over the field of view) and rapid rotation of the disc illuminates the same spot several times within a frame time (for example, within the 33 ms exposure required for video rate), the total dwell time can be much larger than for the CSM with a single pinhole aperture. This increase in dwell time allows for much faster frame rates. A variation of this spinning-disk CSM that affords potentially faster frame rates has slit apertures on the disk, but its principle is otherwise similar, that is, rotation of the disk makes the slits illuminate the entire specimen (a simple and inexpensive plan for a such a microscope can be found in[11,12]).

One disadvantage of the spinning-disk CSM as described is its rather inefficient use of the excitation light. For example, if the pinholes occupy only 1% of the disc area 99% of the illumination of the disc is wasted. A new design for the spinning-disk CSM ('Yokogawa' design) was introduced in which another disk with an array of microlenses is placed on top of the pinholes on the illumination side of the disk. These lenses are illuminated by a collimated laser beam, which the lenses focus into the pinholes, thus greatly increasing the illumination efficiency of the spinning-disk CSM to about 60% or more. Because it is difficult and expensive to build a microlens array that does not suffer from chromatic aberration, two disks need to be used, one for the apertures and the other for the microlenses. A fluorescence filter cube is placed between the two disks so the microlenses are not in the fluorescent return-light path[13,14].

The spinning-disk CSM presents a trade-off between resolution and SNR in terms of the aperture size. In commercially available spinning-disk CSMs, the aperture size is fixed during manufacturing and cannot be adjusted. The size, type and spacing of the aperture on the disc control the background rejection capabilities of the microscope.

In CSMs, the brightness of the out-of-focus excitation decreases with the square of the distance from the in-focus plane. This is because, as already mentioned, the excitation light has an hourglass shape with the waist at the in-focus plane and with the total amount of light the same in each plane. The area over which it is distributed is the area of the circle resulting from the intersection of the cone with the out-of-focus plane. Since this area increases with the square of the out-of-focus distance, the excitation that a pixel receives decreases with the square of this distance. This inverse square law holds as long as out-of-focus structures are illuminated by a single aperture on the disk, but in the spinning-disk CSM, many apertures are used

Table 1 | Useful spectral lines for lasers available for confocal microscopy

Laser	Useful lines (nm)
Argon ion (Ar)	257, 488, 514
Kripton ion (Kr)	531, 568, 647
Ar-Kr	488, 568, 647
Helium-neon (He-Ne)	543, 594, 612, 633
Helium-nadmium (He-Cd)	442
Zinc-Selenium (Zn-Se) diode	430
Neodymium–yttrium aluminum garnet (Nd-YAG)	532, 355, 266
Neodymium–yttrium lithium fluoride (Nd-YLF)	527, 349, 262

to illuminate the specimen. Each of these apertures produces a two cone–shaped illumination about the specimen. Close to the in-focus plane, the cones from different apertures in the disk are distant from each other so that out-of-focus material is illuminated by at most one cone. As the distance from the in-focus plane increases, however, the cones from apertures adjacent in the spinning disc come closer to each other until at some distance (which depends on the NA of the lens and the distance between the apertures[15]), the cones from different apertures cross and more than one cone (and thus by more than one aperture) excite fluorescence. It can be shown that from that distance on, the excitation intensity does not decrease with the out-of-focus distance but remains constant, although at a much lower level than in the wide-field illumination microscope[15].

Figure 3c compares the background discrimination capabilities of the spinning-disk CSM against those of the wide-field and the single-pinhole aperture confocal microscopes. The closer the apertures are, the larger the constant background intensity and the closer to the in-focus plane it remains constant.

Line scanning

Another method to increase the dwell time without decreasing the frame rate is to illuminate an entire line of the specimen simultaneously and focus the fluorescence into a linear CCD array (that is, a row of CCD wells). The use of line illumination obviates the need for scanning the fast axis using an oscillating mirror. Currently, there is one commercial line-scan CSM, the Zeiss LSM 5 Live. This CSM achieves video frame rates by exciting with a line illumination and using a slit confocal aperture. In addition, the microscope can have more than one fluorescent channel and thus can simultaneously detect more than one fluorophore. A slit-confocal-aperture microscope, however, does not afford the resolution improvement of a spot scanning system.

Other scanning approaches

Over the years there have been ingenious attempts to increase the speed of the fast axis scan such as a rotating mirrored polygon[16], or a series of holographic or curved mirrors mounted on a rotating disk, such that each mirror illuminates a different pixel in the specimen[17]. Another method is to drive the fast-axis mirror at its resonance oscillating frequency. In this approach, the fast-axis oscillating mirror and the galvanometer that controls its position are designed such that their resonant frequency is fast enough for video rate scanning, then the electronics drive the mirror at that frequency. One notable custom-built version of this microscope has been described[18]. In a conventional CSM, the raster scan is such that the time between adjacent pixels along the fast scan axis is the same across the scanned field. With the resonant-mirror approach, however this no longer holds. This is because when the mirror is driven at its resonant frequency, the position of the scanning spot across the scan field changes with time according to a sinusoid. This has the potential problem of non-uniform bleaching.

Lasers

Confocal microscopes come with a wide range of options concerning lasers. A purchaser needs to decide which laser lines will be needed to excite the fluorophores in use. The recent advent of solid state lasers adds more choices. The most common workhorse is the multiline argon-ion laser which can emit from the UV (230 nm) to the green (514 nm) with useable power at 257, 477 and 514 nm. Helium-neon (He-Ne) lasers are inexpensive and although they are single-line, they provide useful coverage from the green to the red with useful lines at 534, 567, 594 and 612 nm. Although they have less power than most lasers, power is rarely the limitation that prevents good confocal imaging. Krypton-ion lasers also provide a good selection of lines from the green to the red. When combined with argon; (Ar-Kr laser), it provides lines from the blue to the red. Users who need blue light for CFP use either a helium-cadmium (He-Cd) at 440 nm, a finicky laser, or solid state lines of the zinc-selenium (Zn-Se) diode laser. Users interested in DAPI or some calcium-indicator dyes require UV excitation. At the moment these wavelengths are possible mainly from large argon lasers that sometimes need water cooling. Recently, diode-pumped or lamp-pumped semiconductor lasers that emit in the infrared, such as the neodymium-yttrium aluminum garnet (Nd-YAG) and neodymium-yttrium lithium fluoride (Nd-YLF), have been combined with nonlinear crystals that generate second-, third- or fourth- harmonics. This combination gives lines in the green, UV and deep UV[19]. The lines for different lasers are summarized in Table 1.

POTENTIAL PROBLEMS

Bleaching

The use of the CSM brings with it several potential problems that do not apply to the wide-field microscope. Foremost among them is the increased risk of bleaching. The probability that a molecule bleaches depends on its exposure to the excitation light. This is the product of the irradiance a molecule receives and the time it receives it. Thus, a molecule that receives irradiance I_1 of duration t_1 is as likely to bleach as one that receives twice the irradiance ($2I_1$) for half the time ($t_1/2$). In a CSM, the excitation light is spread over an area that increases with the square of the out-of-focus distance. Consequently, the irradiance decreases in proportion to the square of the distance. Conversely, the time a pixel is exposed is proportional to the area of the excitation and thus to the square of the out-of-focus distance. Therefore, the product of the time an out-of-focus molecule is exposed and the irradiance it receives is almost the same at every depth if the effects of scattering and absorption are negligible. As a result, in-focus and out-of-focus molecules bleach at almost the same rate. With the high irradiance and low per-frame rates typical of the CSM, photobleaching is a serious drawback for many specimens.

When the scanning mechanism uses oscillating mirrors, bleaching occurs not only while the microscope is collecting data, but also during the retrace when the scanning spot is moving back to the beginning of the next image line. During the retrace time, the laser is exciting fluorescence that is not being collected but nonetheless is

bleaching the fluorophore. Placement of a shutter that closes at the end of each line and opens at the beginning of the next, adds to the already long frame scan time of the CSM. Another approach, used in the Zeiss 510 CSM, is to use an acousto-optic tunable filter (AOTF) to prevent fluorescence excitation during the retrace. Because the AOTF has no moving parts, it can be tuned very quickly to block or to pass the excitation light and thus does not increase the scan time.

SNR, NA and magnification

The processes of photon absorption, emission and detection are random and thus the numbers of photons measured from two pixels with equal amounts of fluorophore are similar but not equal. This random variation gives the image a grainy appearance that is stronger for lower image irradiance. Ideally, one would attempt to maximize the number of photons per pixel to increase the SNR. In practice, however, there are limitations and trade-offs to balance (Box 1). The characteristics of the CSM that have the largest effects on image SNR are the size of the pinhole and the NA of the objective.

The light-gathering efficiency of a microscope is proportional to the square of the objective's NA. When also used for illumination, as in confocal scanning microscopy, the overall sensitivity of the CSM is proportional to $(NA)^4$ and is unaffected by magnification power because in the CSM the pinhole aperture size can be adjusted according to the NA and magnification of the objective to obtain the same resolution and SNR with both objectives. For example, the PSF in front of the pinhole for a 100×, 1.4 NA objective is 100 / 60 = 1.67 times larger than the PSF of a 60×, 1.4 NA objective at the same wavelength. Thus, opening the pinhole aperture by a factor of 1.67 will achieve the same resolution and SNR with both objectives. In addition, the CSM has the advantage of an electronic zoom that allows a user to obtain additional (even if empty) magnification by scanning a smaller area with the same number of pixels. Although the electronic zoom does not degrade the SNR, it causes faster photobleaching because the closer the pixels are in the specimen, the longer the excitation dwells over neighboring pixels and thus bleaches them faster.

BOX 1 TROUBLESHOOTING AND CAVEATS

LOW SIGNAL

Effective signal strength measured by the SNR is impacted by many different factors as discussed below.

NA of the objective. The NA of the objective is one of the most critical variables that impacts signal quality in a CSM. Because resolution is determined by the NA and the pinhole size, but is independent of magnification, the best image is obtained by using an objective with a higher NA rather than a higher magnification.

Pinhole size. Reducing the pinhole size rejects more background light and thus increases the depth discrimination. But it also produces a grainy appearance in the image owing to the reduction in the signal compared to random variations recorded by the detector. The optimal pinhole size is between 60% and 80% of the diffraction-limited spot. In practice, larger pinholes must often be used when imaging dim samples or fluorophores that bleach easily. Alternatively, increasing the pinhole beyond (1.22 λ / NA when projected to the specimen) reduces effective imaging depth. With newer bleach-resistant fluorescent quantum dots, however, it may be easier to image with smaller pinhole diameters. Pinholes smaller than 60% of the diffraction limited spot, however, actually worsen the grainy appearance of the image.

PMT gain. Increasing the gain on the PMT will increase the signal but also results in higher shot noise. Such a trade-off may be necessary if bleaching is a problem. This increase in signal and noise is different than the increase that results from 'brightness' control in that the latter increases signal and noise by the same amount and thus has no effect on the grainy appearance of the recorded image.

Laser power. Increasing the laser power is a simple way of increasing the apparent signal but greatly increases the risk of sample bleaching and, more importantly, fluorescence saturation as well as other deleterious effects, so all other optimizations should be attempted first.

Decreasing graininess. The grainy appearance can also be ameliorated by increasing the signal by a larger factor than the random variations that cause the grainy appearance. This can be accomplished by increasing the dwell time at the risk of increased bleaching. It is also possible to increase the scanning speed and reduce the laser power while using filtering methods to combine data from multiple scans.

Fluorophore concentration. The fluorescent emission intensity is proportional to the concentration of fluorescent dye, but there are practical limitations to this concentration. A very high concentration could have toxic effects on the organism under study, interfere with the process being observed, or leave a large amount nonspecific fluorescence. To avoid these pitfalls, the concentration of fluorescent dye is usually kept low with a resulting low fluorescence intensity that brings a low SNR. Quantum dots and other new fluorophores with improved characteristics can help reduce these problems.

SLOW IMAGING

For users of fluorescence widefield microscopes in which video-rate or faster imaging is relatively straightforward, the slow rate of data flow in laser scanning confocal microscopes can be frustrating. Thus, for moving the stage and finding objects of interest, many users still resort to direct viewing of the widefield fluorescence image by eye and then initiating a scan. Most modern laser scanners, however, have a 'focus' mode with scans of 5 or more frames per second. Although these images are noisy and severely undersample the data, they may serve to speed the process of finding a particular spot to image. When data itself must be sampled quickly, 'line scans' are an option.

BLEEDTHROUGH

It is becoming increasingly common to simultaneously use two or more fluorescent dyes for imaging different properties or structures of the specimen. If more than one dye is present, however, a channel designed for a particular dye will collect fluorescence from other dyes whose excitation and fluorescence spectra overlap with the dye of interest. When this is not taken into account and compensated for, the recorded images for a given dye are artifactual because of contributions from other dyes. The linear unmixing methods described in the text can effectively separate the different dyes.

Conversely, in the wide-field microscope, the objective magnification has a strong effect on the image SNR. Given two objectives with the same NA and using the same camera, the objective with the larger magnification spreads the light over a larger area in proportion to the square of the magnification.

Too much scatter (deep imaging)

When a CSM is used to image detail within a relatively thick layer of tissue, the excitation and the emission photons must travel through the tissue where molecular interactions will change their direction. As a result, the excitation light is spread over a volume much larger than the diffraction-limited spot and thus the excitation is weaker over a larger volume. The fluorescence emitted from a molecule within this volume can be scattered on its way to the objective so that it no longer seems to come from the scanning spot. Thus, out-of-focus light might appear to come from the location of the scanning spot whereas in-focus light is rejected because it is scattered by out-of-focus tissue. The resulting image has two major degradations, namely, it is severely blurred and has a very low SNR. For deep imaging in tissue, two-photon fluorescence microscopy may be more suitable[1].

DATA PROCESSING

Averaging approaches

Despite the marked improvement in contrast owing to rejection of out-of-focus light, images from CSMs have low SNR because of the small number of photons that can be excited from each pixel in the short time the pixel is under the scanning spot. This problem is obvious in the graininess of many confocal images. Some users attempt to correct this problem by increasing the laser power during the scan, but this is generally a mistake. The laser intensity possible in most commercial laser scanning confocals far exceeds that necessary to saturate the fluorophore in the focal plane. In other words, the fluorescent molecules at the waist of the hourglass-shaped beam are cycling between excited state and ground state as fast as they can, and greater illumination irradiance provides no additional fluorescence. On the other hand, increased illumination will cause increasing amounts of out-of-focus light to percolate through the pinhole, causing the image to loose resolution in all dimensions. If one keeps the laser power low (that is, $<\sim$1.5 mW for a scanning spot 0.5 μm across[20]) one can still improve the SNR by collecting several images of the same plane and averaging or adding them. The two most widely used methods are a simple average and the Kalman filter, which is an auto-regressive moving-average filter (for a detailed description of the Kalman filter see[21,22]). Each pixel of the final image is obtained from measurements of the same pixel at different times. As these averaging approaches operate in time, not space, they have little or no effect on the resolution (strictly speaking, there is a degradation in resolution because the scanning mechanism may not place the scanning spot precisely enough during repeated scans).

In the simple average filter all the 2D images are simply averaged. This increases the SNR in direct proportion to the square root of the number of frames that are averaged. That is, averaging four frames doubles the SNR, whereas averaging 16 increases the SNR by a factor of $(16)^{1/2} = 4$. The Kalman filter is a more elaborate statistical filter that uses auto-regression of prior measurements to predict the present measurement and then corrects the estimate with a moving average as soon as the present measurement is available. The strongest advantage of the Kalman filter over simple filtering is that it requires very few frames (typically less then 5) to reach a steady value for each pixel, whereas the simple average requires more frames. The disadvantage of the Kalman filter is that it assumes that noise is additive. Although not strictly correct, this assumption has little effect on the results when the number of photons per pixel is above ~20. In cases with a lower number of photons, simple averaging might be a better choice of method.

Another approach to noise reduction is to increase the dwell time by slowing the scan speed. Most commercial laser scanners allow the user to adjust the scan time over a wide range. This approach has one drawback: as a population of fluorophores are excited they tend to progressively partition into the long-lived triplet state where they are no longer able to fluoresce and are subject to bleaching. Thus, with a long duration exposure of each pixel, the laser excitation will first initiate good fluorescence but within several hundred nanoseconds the same laser intensity will become less effective[20]. In summary, fast scanning with low power and averaging is probably the best way to obtain a good image, although the ability of the scanning mirrors to accurately go to exactly the same position may tend to blur these images a bit. Some trial and error is required to find the best noise reduction method for a particular device.

Linear unmixing

The large cadre of fluorescent probes available at different wavelengths provides both unprecedented opportunities for multispectral imaging and a problem: crosstalk between different fluorescent signals. The most straightforward approach to disambiguating fluorescence signals is to sequentially record images at the emission wavelengths of the different fluorescent dyes. Sequential scanning gives excellent separation of fluorophore images because both the excitation and emission can be altered (as with standard filter cubes). The problem with sequential imaging is that if one wishes to take a stack of images the time of imaging increases in proportion to the number of images. A stack of 100 images with three fluorophore sequential imaging in which each image is averaged three times to remove noise will take ~15 min. A second problem with sequential imaging is that it is sometimes unable to remove crosstalk because the dyes' absorption and emission spectra overlap too much. This is a considerable problem with fluorescent proteins that typically have wide emission and absorbance spectra[23], though newer variants are helping to reduce this problem[24]. CSMs offer the possibility of simultaneous scanning because the emitted light can routinely be beam-split to different detectors to collect different emission wavelengths. The wavelengths can be separated by color filters (for example, dichroic or interference filters) or spatially by a prism that takes advantage of dispersion to produce a rainbow-colored pattern. This dispersion is used by Leica spectral confocal microscopes, to bring different colors of light to different detectors.

One serious drawback of trying to image more than one fluorescent dye at a time, however, is that the overlap of excitation and emission spectra make it difficult or even impossible to find an emission wavelength that detects one fluorophore and none of another. A solution is to record what is sometimes called a λ scan, which is a fluorescence excitation spectrum of all the dyes while exciting with one or more wavelengths. Unlike a typical spectrum done at one point, this scan is done spatially on a whole image plane. The number of spectral points in the scan must equal or exceed the number of dyes one is trying to separate. Taking images at several wavelengths takes time. In the Zeiss version of this approach (Meta) a prism is used to

obtain the spectral images simultaneously. In the Olympus configuration the λ scan is done sequentially. In both cases, however, the narrowness of the spectral bands reduces the SNR, requiring averaging and more time. Conversely, the λ scan does provide access to the full fluorescence emission of a fluorophore and using the emission spectra of each different fluorophore to identify the contribution of each provides a means of eliminating crosstalk[24–28].

To see how this method works, assume that a specimen is stained with three different fluorescent dyes (Fig. 4a). Cyan fluorescent protein (CFP; triangles) has a peak emission at 477 nm, fluorescein isothiocyanate (FITC; squares), at 535 nm, and tetramethyl rhodamine isothiocyanate (TRITC; circles), at 575 nm. The rectangles in Figure 4a represent the ideal response of barrier filters commonly used for the three dyes. It is clear that there is substantial overlap of the three spectra and that none of the filters completely rejects fluorescence from another dye. The superposition of images collected with the three filters is shown in Figure 4b. We have circled and labeled three spots that have different concentrations of the three fluorescent dyes. Spot 1 has 10% CFP, 30% FITC and 60% TRITC. Spot 2 has 10% CFP, 60% FITC and 30% TRITC. Finally, Spot 3 has 70% CFP, and 15% each FITC and TRITC. The individual images collected with the three filters show that the three labeled spots appear in more than one image not only because of the mixture of dyes but also because of the overlap of the three spectra (Fig. 4c–e). Emission curves show the λ scan at each of the three fluorescent spots and the vertical bars show the readings obtained using the barrier filters for each of the three dyes assuming that each filter collects all the fluorescence within its passband (Fig. 4f–h). Using these profiles and the spectra in Figure 4a, it is possible to write a set of linear equations that relate the relative concentrations of the three dyes to the amount of light measured by each detector. Using the measured intensities from the detectors the linear equations can be solved to obtain the amount of each of the fluorescent dyes at each of the spots. This is called linear unmixing, and it is not restricted to unmixing three dyes. By using at least as many channels and filters as there are fluorescent dyes in the sample, it is possible to unmix more dyes, and additional channels will reduce the effects of noise.

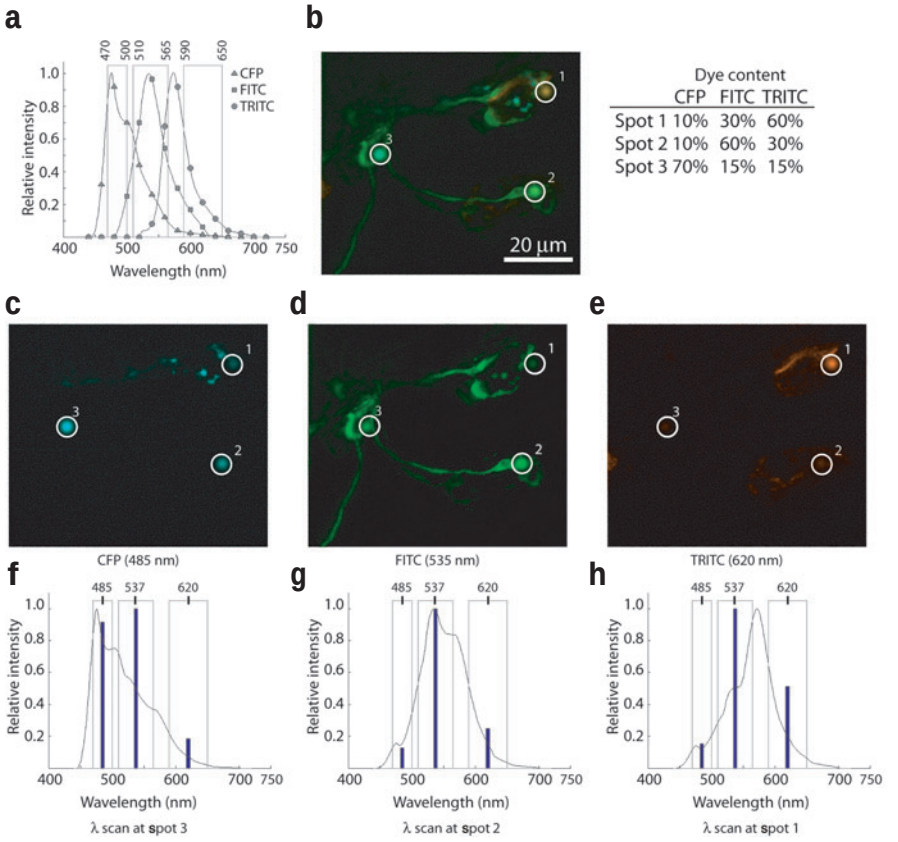

Figure 4 | Linear unmixing. (**a**) Emission spectra for CFP, FITC and TRITC. The rectangles represent the ideal response of barrier filters commonly used for the three dyes. The numbers on top of the rectangles are the cut-off wavelengths for each of the filters. (**b**) Color composite made with the images recorded at the peaks of the three dyes. The three spots marked with circles have known mixtures of the three dyes. (**c**–**e**) Images obtained with each of the three barrier filters. (**f**–**h**) λ scans at each of the three spots circled in **c**–**e** collected with ideal narrow-band barrier filters. As in **a**, the rectangles are ideal responses of the three barrier filters commonly used for the three dyes. The vertical bars indicate the response collected by the detector with each of the three filters at each of the three spots (the bars are placed at the mean wavelength of each filter; this wavelength is indicated at the top of each rectangle).

OTHER OPTICAL SECTIONING TECHNIQUES

Deconvolution (computational optical microscopy)

A method that has steadily gained acceptance as an alternative as well as a complement to confocal scanning and two-photon fluorescence excitation microscopy is computational optical sectioning microscopy (COSM), also known as deconvolution microscopy and sometimes as 'digital confocal' (although the latter is a misnomer because in COSM with a widefield microscope, the specimen is under Köhler illumination and thus excitation is maximally out of focus at the specimen, whereas the term confocal means excitation and detection are in focus at the same point). In COSM, as with a CSM, a 3D image is collected as a series of 2D images (or optical slices), each with the microscope focused at a different plane through the specimen. If a wide-field microscope is used, each of the 2D images has the in-focus information plus substantial contributions from out-of-focus material. In COSM, a computational method derived from information about the process of image formation and recording is used to remove the out-of-focus light from each optical slice. Several methods have been derived for COSM whose differences stem from the different mathematical models used for the process of image formation and recording. Because a very accurate model for the process of image formation and recording would be mathematically and computationally intractable, different models rely on different simplifying assumptions. Better models of the process of image formation and recording lead to better results, usually at the expense of higher computational cost. The earliest models were heavily simplified and led to methods with very low computational demands. As comput-

ing power increased, it allowed the use of methods based on more exact formulations of the imaging process, and algorithm developers tapped into the increased computer power to derive methods based on more precise models. Here we will briefly touch on the results and limitations of some methods (Fig. 5). For a more thorough review see reference 29.

Nearest neighbors deconvolution. One of the first COSM methods, called nearest neighbors subtraction (NNS), is based on a simple model of image formation, namely that out-of-focus light from a given optical slice is relevant only in the two adjacent slices. To undo this degradation, the method blurs the adjacent slices with a 2D PSF calculated for a miss-focus distance equal to the distance between adjacent optical slices and subtracts them from the optical slice of interest to remove the out-of-focus light. The result can be filtered with a Wiener-type filter to remove some of the in-focus blur. This process is repeated for all the optical slices. Although the method is based on a very simplified model, it applies when the fluorescent light rapidly decreases away from the focus, as for small puncta, thin filaments, or a combination of them. For example, in a single optical slice of fluorescently labeled actin filaments extracted from a 3D image stack (Fig. 5a) the NNS method effectively removes the out-of-focus blur (Fig. 5b). For specimens in which the fluorescence covers larger areas (for example, cell membranes) or volumes (for example, neuromuscular junctions), the simple model does not apply and a different approach is necessary.

Frequency-based deconvolution. One such different approach is based on how the microscope images periodic structures. Given a periodic structure, such as a diffraction grating, the contrast in the image greatly depends on the frequency of the structure (measured, for example, in cycles per μm). For small frequencies, the image shows very good contrast, but as the frequency of the grating is increased (the distance between adjacent stripes reduced), the contrast is reduced until it vanishes completely when the frequency of the grid reaches 2 NA / λ. Frequencies higher than this cut-off frequency are not passed by the microscope to the image. The way the microscope images periodic structures is mathematically described by the optical transfer function (OTF). This is the Fourier transform of the PSF of the microscope. Any image can be analyzed into a series of periodic structures of different frequencies, amplitudes and phases that, when superimposed, give rise to the image. These series of structures are called the frequency components of the image. It is computationally straightforward to obtain the frequency components of an image by using a Fourier transform.

Because the frequency components of the image are the frequency components of the specimen multiplied by the OTF, the frequency components of the specimen can be obtained by dividing the image frequency components by the OTF. This simple operation, however, is not possible because the OTF is zero for all frequencies above the cut-off frequency. The two most widely-used approaches to avoid this division by zero are the Moore-Penrose pseudo-inverse (MPPI; Fig. 5c)[30] and the Wiener or, more properly, Wiener-Helstrom filter (WHF, Fig. 5d). Each of these methods introduces a small arbitrary correction factor ε, thus avoiding the division by zero, but use different methods of doing so. For a thorough description see reference 31. The choice of ε controls the tradeoff between the resolution and the amount of noise in the resulting specimen estimate. Small ε results in finer resolution but more noise. The MPPI and WHF operate on the whole 3D stack, not on each optical slice as the NNS, and thus they can remove out-of-focus light from more distant planes. An optical slice from a 3D image of fluorescently labeled membranes of *Hystoplasma capsulatum* is shown in Figure 5e. The NNS not only does not remove the out-of-focus light inside the membrane, but results in a grainy appearance that gives the impression of a specimen made of small puncta (Fig. 5f). Both the MPPI and the WHF, however, remove the out-of-focus light and do not 'break' the cell membrane into a series of spots (Fig. 5g,h).

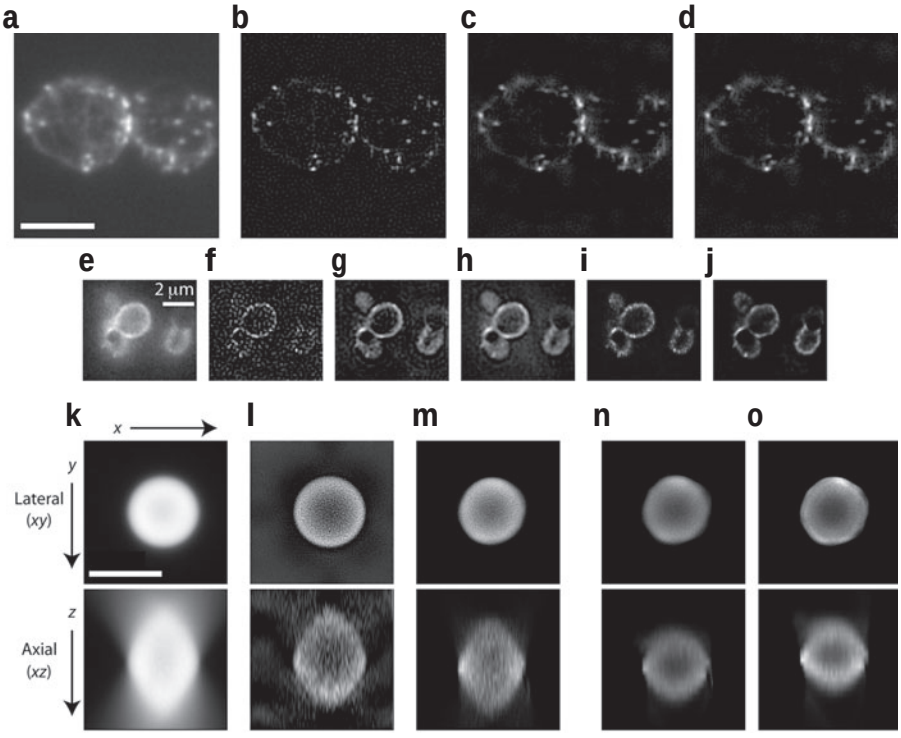

Figure 5 | Deconvolution results. (**a**–**d**) A specimen consisting mostly of puncta and thin filaments (images courtesy of T. Karpova, National Cancer Institute). The original image slice (**a**) and deconvolutions obtained using NNS (**b**), MPPI (**c**) and WHF (**d**) methods. Bar, 5 μm. (**e**–**j**) *H. capsulatum* with the cell membrane fluorescently labeled (images courtesy of W. Goldman, Washington University School of Medicine). The original image slice (**e**) and deconvolutions obtained using NNS (**f**), MPPI (**g**) and WHF (**h**), JvC (**i**) and the expectation-maximization maximum-likelihood (**j**) methods. Bar, 2 μm. (**k**–**o**) Sections through the center of a 3D image stack of a 10-μm diameter polystyrene microsphere (images courtesy of J.G. McNally, National Cancer Institute). Top, lateral section; Bottom, axial section. The original image slice (**k**) and deconvolutions obtained using a MPPI (**l**), JvC (500 iterations, smoothing every 10 iterations; **m**), constraint maximum-likelihood expectation maximization (3,000 iterations; **n**) and gradient-based method (100 iterations; **o**). Bar, 10 μm.

Constraint deconvolution. One serious drawback of the methods described above is that they cannot estimate frequency components of the specimen at frequencies that are not passed by the objective. These frequencies, however, are often necessary for the correct estimation of the specimen. For example, image sections through the center of a 3D image stack of a 10-µm-diameter polystyrene microsphere with a thick superficial fluorescent layer 1 to 2 µm thick are shown in Figure 5i. This image has two problems. (i) There is no fluorescent dye in the core of the microsphere but the image shows a bright core and (ii) although the specimen is a sphere, the *xz* section has a diamond shape in addition to dimmer 'butterfly wings'. We have demonstrated that the diamond shape results from the lack of important frequency components[32]. Because the image lacks frequency components, the MPPI can not recover the spherical shape of the specimen and only partially removes the 'butterfly wings' from the image (Fig. 5j). The results from the WHF (not shown) are similar. Because these frequency components are not in the image, it is necessary to derive algorithms that use information about the specimen known *a priori*. This information might be the fact that fluorescence is neither negative nor infinite or that the specimen has a finite size. Prior knowledge about the specimen is used to enforce constraints that the specimen estimate must satisfy. Incorporating these constraints into the algorithm usually leads to iterative methods that perform several operations over and over until certain criteria are satisfied.

The most widely used methods for constraint deconvolution are the Jansson-van Cittert (JvC) method of repeated convolution[33] as modified in reference 34 and commercially distributed by Applied Precision; the constrained least squares method developed by Carrington[35,36] and distributed by Scanalitics; and the maximum-likelihood image estimation independently developed by Holmes[37,38] and by Conchello[4,39,40] from the expectation maximization formalism[41]. The Holmes method is commercially distributed by AutoQuant Imaging and the Conchello method is freely available online (http://www.omrfcosm.omrf.org). Although the JvC method does correctly find the dark core of the microsphere and removes the 'butterfly wings' it still shows the diamond shape in the axial section (Fig. 5m). The expectation maximization–maximum likelihood method recovers the spherical shape of the specimen albeit at the expense of a large number of iterations (Fig. 5n). The maximum-likelihood estimation method, however, can be improved by using a different method than expectation maximization to find the maximum of the likelihood function. In fact, by using a gradient-based algorithm we found a substantial increase in speed with little or no degradation in performance (Fig. 5o)[42].

New wide-field techniques

In recent years, new methods for optical sectioning microscopy have been developed for wide-field illumination, which do not use uniform illumination. Instead, these methods give some spatial structure to the illumination. The most notable ones are aperture-correlation microscopy[43–46] and sine-modulated illumination microscopy. The former method, however, required a large number of images to be collected at each focal plane and thus found little application. The latter, which is more often called structured illumination microscopy (SIM), is a simpler and more powerful method for optical sectioning microscopy[47–55]. In SIM, a sinusoidal illumination pattern is focused by the objective into the in-focus plane of the specimen and an image I_1 is collected. The pattern is then shifted laterally by a third of the cycle of the pattern, and a second image I_2 is collected. The illumination pattern is shifted a second time a third of its cycle and a third image is recorded. Each of these images contains both in-focus and out-of-focus information. The in-focus information, however, is modulated by the sinusoidal illumination pattern, whereas the out-of-focus information is much less affected by the structure of the illumination. There are two simple ways to remove the sinusoidal illumination pattern from the images. One is by simply averaging of the three images. The result, however, is the image that would have been obtained with a conventional wide-field microscope. That is, it contains the out-of-focus light. The other is to calculate

$$I_p = \frac{\sqrt{2}}{3}\sqrt{(I_1 - I_2)^2 + (I_1 - I_3)^2 + (I_3 - I_2)^2}\ .$$

The pairwise subtraction of images removes the parts that are common to the images in the pair. This is mostly out-of-focus light that was not affected by the structure of the illumination. Thus, the resulting image contains little out-of-focus light. In fact the depth resolution possible with the SIM is similar to that achievable with the CSM. To our knowledge, there is currently only one commercial version of the SIM, namely the Zeiss Apotome (Karl Zeiss). Because the price of the Apotome is much less than that of a laser CSM, the SIM is sometimes called a 'poor-man's confocal microscope'.

CONCLUSIONS

Optical sectioning microscopy is a powerful tool for biological investigation, and confocal microscopy is often the method of choice. As explained above, CSMs have the capability to record 3D images that are not affected by out-of-focus light, thus increasing the contrast and resolution of the recorded image. In addition, the wide selection of available fluorescent probes, lasers and filters makes the CSM a powerful tool for multispectral imaging when aided by linear unmixing. In addition to the CSM, the 'digital confocal microscope' and the 'poor-man's confocal microscope' provide alternative methods for 3D microscopy that have image collection times much shorter than those typical of the CSM. The interested user is encouraged to read available literature [56–68].

COMPETING INTERESTS STATEMENT
The authors declare that they have no competing financial interests.

Published online at http://www.nature.com/naturemethods/
Reprints and permissions information is available online at http://npg.nature.com/reprintsandpermissions/

1. Helmchen, F. & Denk, W. Deep tissue two-photon microscopy. *Nat. Methods* **2**, 932–940 (2005).
2. Minsky, M. (US patent 3013467, 1961).
3. Minsky, M. Memoir on inventing the confocal scanning microscope. *Scanning* **10**, 128–139 (1988).
4. Conchello, J-A., Kim, J.J. & Hansen, E.W. Enhanced 3D reconstruction from confocal scanning microscope images. II: depth discrimination vs. signal-to-noise ratio in partially confocal images. *Appl. Opt.* **33**, 3740–3750 (1994).
5. Sandison, D.R., Piston, D., Williams, R.M. & Webb, W.W. Quantitative comparison of background rejection, signal-to-nose ratio, and resolution in confocal and full-field laser scanning microscopes. *Appl. Opt.* **34**, 3576–3588 (1995).
6. Tsien, R.Y. & Waggoner, A. Fluorophores for confocal microscopy. In *Handbook of biological confocal microscopy* (ed. Pawley, J.B.) 267–279 (Plenum Press, New York, 1995).
7. Petràn, M., Hardvsky, M., Egger, M.D. & Galambos, R. Tandem scanning reflected-light microscope. *J. Opt. Soc. Am.* **58**, 661–664 (1968).
8. Petràn, M., Boyde, A. & Hardvsky, M. Direct view confocal microscopy. In *Confocal Microscopy* (ed. Wilson, T.) 245–284 (Academic Press, New York, 1990).

9. Kino, G.S. & Xiao, G.Q. Real-time scanning microscopes. In *Confocal Microscopy* (ed. Wilson, T.) 361–388 (Academic Press, London, 1990).
10. Lichtman, J.W. Confocal microscopy. *Sci. Am.* **271**, 30–35 (1994).
11. Lichtman, J.W. High-resolution imaging of synaptic structure with a simple confocal microscope. *New Biol.* **1**, 75–82 (1989).
12. Lichtman, J.W. & Sunderland, W.J. (Washington Univeristy; US patent 4884880, 1990).
13. Inoué, S. & Inoué, T. Direct-view high-speed confocal scanner: The CSU-10. In *Cell biological applications of confocal microscopy* (ed. Matsumoto, B.) 88–128 (Academic Press, New York, 2002).
14. Tanaami, T. *et al.* High-speed 1-frame/ms scanning confocal microscope with a microlens and a Nipkow disk. *Appl. Opt.* **41**, 4704–4708 (2002).
15. Conchello, J-A. & Lichtman, J.W. Theoretical analysis of a rotating-disk partially confocal scanning microscope. *Appl. Opt.* **33**, 585–596 (1994).
16. Stutz, G.E. Laser scanning system design. *Photonics Spectra* **24**, 113–116 (1990).
17. Tsien, R.Y. & Bacskai, B.J. Video-rate confocal microscopy. In *Handbook of biological confocal microscopy* (ed. Pawley, J.B.) 459–478 (Plenum Press, New York, 1995).
18. Callamaras, N. & Parker, I. Construction of a confocal microscope for real-time x-y and x-z imaging. *Cell Calcium* **26**, 271–279 (1999).
19. Gratton, E. & vande Ven, M. J. Laser sources for confocal microscopy. In *Handbook of biological confocal microscopy* (ed. Pawley, J.B.) 69–97 (Plenum Press, New York, 1995).
20. Sandison, D.R., Williams, R.M., Wells, K.S., Stricker, J. & Webb, W.W. Quantitative fluorescence confocal laser scanning microscopy (CLSM). In *Handbook of biological confocal microscopy* (ed. Pawley, J.B.) 39–53 (Plenum Press, New York, 1995).
21. Srinath, M.D. & Rajasekaran, P.K. *Statistical Signal Processing with Applications* (John Willey and Sons, New York, 1979).
22. Kay, S.M. Fundamentals of statistical signal processing (Prentice Hall, 1993).
23. Lichtman, J. & Conchello, J.-A. Fluorescence microscopy. *Nat. Methods* **2**, 910–919 (2005).
24. Shaner, N.C., Steinbach, P.A. & Tsien, R.Y. A guide to choosing fluorescent proteins. *Nat. Methods* **2**, 905–909 (2005).
25. Zimmermann, T. Spectral imaging and linear unmixing in light microscopy. In *Microscopy techniques advances in biochemical engineering/biotechnology* **95**, 245–265 (2005).
26. Zimmermann, T., Rietdorf, J. & Pepperkok, R. Spectral imaging and its applications in live cell microscopy. *FEBS Lett.* **546**, 87–92 (2003).
27. Zimmermann, T., Rietdorf, J., Girod, A., Georget, V. & Pepperkok, R. Spectral imaging and linear un-mixing enables improved FRET efficiency with a novel GFP2-YFP FRET pair. *FEBS Lett.* **531**, 245–249 (2002).
28. Hiraoka, Y., Shimi, T. & Haraguchi, T. Multispectral imaging fluorescence microscopy for living cells. *Cell Struct. Funct.* **27**, 367–374 (2002).
29. Conchello, J.-A. An overview of three-dimensional and four-dimensional microscopy by computational deconvolution. In *Cell Imaging-Methods Express* (ed. Stevens, D.) 181–204 (2005).
30. Preza, C., Miller, M.I. & Thomas, L.J. Jt. & McNally, J. G. Regularized linear method for reconstruction of three-dimensional microscopic objects from optical sections. *J. Opt. Soc. Am. A* **9**, 219–228 (1992).
31. Frieden, B.R. *Probability, statistical optics, and data testing.* 206–210 (Springer-Verlag, Berlin, Germany, 1982).
32. McNally, J.G., Preza, C., Conchello, J-A. & Thomas, L.J., Jr. Artifacts in computational optical sectioning microscopy. *J. Opt. Soc. Am. A* **11**, 1056–1067 (1994).
33. Frieden, B.R. Image enhancement and restoration. In *Picture processing and image filtering* (ed. Huang, T.S.) 179–248 (Springer-Verlag, New York, 1975).
34. Agard, D.A. Optical sectioning microscopy. *Annu. Rev. Biophys. Bioeng.* **13**, 191–219 (1984).
35. Carrington, W.A. Image restoration in 3D microscopy with limited data in *Bioimaging and two-dimensional spectroscopy* (ed. Smith, L.C.) 72–83 (SPIE Press, Bellingham, Washington, 1990).
36. Carrington, W.A. & Fogarty, K.E. (US patent 5047968, 1991).
37. Holmes, T.J. Maximum-likelihood image restoration adapted for noncoherent optical imaging. *J. Opt. Soc. Am. A* **5**, 666–673 (1988).
38. Holmes, T.J. & Liu, Y-H. Richardson-Lucy/maximum likelihood image restoration algorithm for fluorescence microscopy: further testing. *Appl. Opt.* **28**, 4930–4938 (1989).
39. Conchello, J-A. Super-resolution and convergence properties of the expectation maximization for maximum-likelihood deconvolution of incoherent images. *J. Opt. Soc. Am. A* **15**, 2609–2619 (1998).
40. Conchello, J-A. & Hansen, E.W. Enhanced 3D reconstruction from confocal scanning microscope images I: Deterministic and maximum likelihood reconstructions. *Appl. Opt.* **29**, 3795–3804 (1990).
41. Dempster, A. P., Laird, N. M. & Rubin, D. B. Maximum likelihood from incomplete data via the EM algorithm. *J. R. Stat. Soc. B* **39** 1–38 (1977).
42. Markham, J. & Conchello, J-A. Fast maximum-likelihood image restoration algorithms for three-dimensional fluorescence microscopy. *J. Opt. Soc. Am. A* **18**, 1062–1071 (2001).
43. Hanley, Q.S., Verveer, P.J. & Jovin, T.M. Optical sectioning fluorescence spectroscopy in a progammagle array microscope. *Appl. Spectrosc.* **52**, 783–789 (1998).
44. Verveer, P.J., Hanley, Q.S., Verbeek, P.W., van Vliet, L.J. & Jovin, T.M. Theory of confocal fluorescence imaging in the programmable array microscope (PAM). *J. Microsc.* **189**, 192–198 (1998).
45. Wilson, T., Juskaitis, R., Neil, M.A.A. & Kozubek, M. Confocal microscopy by aperture correlation. *Opt. Lett.* **21**, 1879–1881 (1996).
46. Dixon, T. Microscopy - Random mask brightness image. *Nature* **383**, 760–761 (1996).
47. Neil, M.A.A., Juškaitis, R. & Wilson, T. Method for obtaining sectioning by using structured light in a conventional microscope. *Opt. Lett.* **25**, 1361–1363 (1997).
48. Wilson, T., Neil, M.A.A. & Juškaitis, R. Optically Sectioned images in wide-field fluorescence microscopy. In *Three-dimensional and multidimensional microscopy: Image Acquisition and Processing V* (eds. Cogswell, C.J., Conchello, J.-A., Lerner, J.M., Lu, T. & Wilson, T.) 4–6 (SPIE Press, Bellingham, Washington, 1998).
49. Gustafsson, M.G.L., Agard, D.A. & Sedat, J.W. Doubling the lateral resolution of wide-field fluorescence microscopy using structured illumination. In *Three-dimensional and multidimensional microscopy: image acquisition and processing VII* (eds. Conchello, J.-A., Cogswell, C.J. & Wilson, T.) 141–150 (SPIE Press, Belingham, WA, 2000).
50. Gustafsson, M.G.L., Agard, D.A. & Sedat, J.W. Surpasing the lateral resolution by a factor of two using structured illumination microscopy. *J. Microsc.* **198**, 82–87 (2000).
51. Neil, M.A.A., Juškaitis, R. & Wilson, T. Real time 3D fluorescence microscopy by two beam interferece illumination. *Opt. Commun.* **153**, 1–4 (1998).
52. Neil, M.A.A., Juškaitis, R. & Wilson, T. A light efficient optically sectioning microscope. *J. Microsc.* **189**, 114–117 (1998).
53. Wilson, T., Neil, M.A.A. & Juškaitis, R. Real-time three-dimensional imaging of macroscopic structures. *J. Microsc.* **191**, 116–118 (1998).
54. Gustafsson, M.G.L. Extended resolution fluorescence microscopy. *Curr. Opin. Struct. Biol.* **9**, 627–634 (1999).
55. Fedosseev, R., Belyaev, Y., Frohn, J. & Stemmer, A. Structured light illumination for extended resolution in fluorescence microscopy. *Opt. Lasers Eng.* **43**, 403–314 (2005).
56. Conn, P.M. (ed.) *Confocal Microscopy* (Academic Press, New York, 1999).
57. Diaspro, A. (ed.). Confocal and two-photon microscopy: Foundations, applications and advances. (John Wiley and Sons, New York, 2001).
58. Inoué, S. & Spring, K.R. *Video Microscopy. The Fundamentals* (Plenum Press, New York, 1997).
59. Matsumoto, B. (ed.). *Cell biological applications of confocal microscopy* (Academic Press, New York, 2003).
60. Murphy, D.B. Fundamentals of light microscopy and electronic imaging (Wiley-Liss, New York, 2001).
61. Pawley, J.B. (ed.). *Handbook of biological confocal microscopy* (Plenum Press, New York, 1995).
62. Paddock, S. (ed.). *Confocal Microscopy* (Oxford University Press, Oxford, 2001).
63. Periasamy, A. (ed.). *Methods in Cellular Imaging* (Oxford University Press, Oxford, 2001).
64. Sheppard, C.J.R. & Shotton, D.M. *Confocal Laser Scanning Microscopy* (BIOS Scientific Publisers, Oxford, 1997).
65. Stevens, J.K., Mills, L.R. & Trogadis, J.E. *Three-dimensinoal confocal microscopy: Volume investigation of biological systems* (Academic Press, New York, 1994).
66. Toomre, D. & Manstein, D.J. Lighting up the cell surface with evanescent wave microscopy. *Trends Cell Biol.* **11**, 298–303 (2001).
67. Tsien, R.Y. Imagining imaging's future. *Nat. Rev. Mol. Cell. Biol.* **4** (Suppl.), SS16–SS21 (2003).
68. Yuste, R., Lanni, F. & Konnerth, A. (eds.) *Imaging neurons: A laboratory manual* (Cold Spring Harbor Laboratory Press, Cold Spring Harbor, 2000).

Deep tissue two-photon microscopy

Fritjof Helmchen[1] & Winfried Denk[2]

With few exceptions biological tissues strongly scatter light, making high-resolution deep imaging impossible for traditional—including confocal—fluorescence microscopy. Nonlinear optical microscopy, in particular two photon–excited fluorescence microscopy, has overcome this limitation, providing large depth penetration mainly because even multiply scattered signal photons can be assigned to their origin as the result of localized nonlinear signal generation. Two-photon microscopy thus allows cellular imaging several hundred microns deep in various organs of living animals. Here we review fundamental concepts of nonlinear microscopy and discuss conditions relevant for achieving large imaging depths in intact tissue.

Microscopists have always desired to look inside various organ tissues to study structure, function and dysfunction of their cellular constituents. In the past, this has frequently required tissue extraction and histological preparation to gain access. Traditional optical microscopy techniques, which use linear (one-photon) absorption processes for contrast generation, are limited to use near the tissue surface (less than 100 μm) for high-resolution imaging because at greater depths strong and multiple light scattering blurs the images. Scattering particularly strongly affects signal strength in confocal microscopy, which achieves three-dimensional resolution and optical sectioning with a detection pinhole that rejects all light that appears not to originate from the focus.

During the past two decades new optical microscopy techniques have been developed that use nonlinear light-matter interactions to generate signal contrast (reviewed in[1–7]). Nonlinear optical microscopy techniques have special features that make them less sensitive to scattering and thus are well suited for high-resolution imaging in tissues. In particular, two photon–excited fluorescence laser-scanning microscopy (2PLSM)[8], combined with *in vivo* fluorescence labeling techniques, has opened a rapidly expanding field of imaging studies in intact tissues and living animals. Specimens as diverse as lymphatic organs[9,10], kidney[11], heart[12], skin[13] and brain[2,4] can now be examined in detail at depths of up to one millimeter[14], while leaving the tissue intact. Moreover, 2PLSM is used as a tool to study the development, progression and potential treatment of pathological conditions such as tumors[15] and Alzheimer disease[16].

Although 2PLSM by now is a well-established technique, using turn-key laser sources and commercial microscope systems, it remains important to understand the underlying principles and key technical aspects, especially when optimizing a microscope system to achieve large imaging depths. In this review, we discuss physical principles, with special emphasis on imaging-system parameters important for deep imaging, and summarize technical issues regarding the application of 2PLSM for high-resolution imaging in living animals.

NONLINEAR OPTICAL MICROSCOPY

In optical microscopy one can distinguish between linear and nonlinear excitation. Traditional techniques, including confocal microscopy, generate contrast from light-matter interactions, in which the elementary process involves a single photon and which therefore depend linearly on the incident light intensity. Nonlinear techniques are fundamentally different in that they use 'higher-order' light-matter interactions involving multiple photons for contrast generation. The nonlinear nature of these interactions leads to qualitatively new imaging properties.

[1]Department of Neurophysiology, Brain Research Institute, University of Zurich, CH-8057 Zurich, Switzerland. [2]Department of Biomedical Optics, Max Planck Institute for Medical Research, D-69120 Heidelberg, Germany. Correspondence should be addressed to F.H. (helmchen@hifo.unizh.ch) or W.D. (winfried.denk@mpimf-heidelberg.mpg.de).

PUBLISHED ONLINE 18 NOVEMBER 2005; DOI:10.1038/NMETH818

Multiphoton absorption

Several different nonlinear processes can occur when light interacts with matter (Fig. 1). Most widely used in biological imaging is fluorescence excitation by two-photon absorption[17]. Two photons that arrive 'simultaneously' (within ~0.5 fs) at a molecule combine their energies to promote the molecule to an excited state, which then proceeds along the normal fluorescence-emission (or photochemical-reaction) pathway[1,17]. Similarly, three or more photons can combine to cause excitation.

The efficiency of multiphoton absorption depends on physical properties of the molecule (the 'multiphoton absorption cross-section')[5,18], and on the spatial and temporal distribution of the excitation light. Most nonlinear processes have in common that the transition probabilities are extremely low at 'normal' light intensities. To generate sufficient signal, excitation light has to be concentrated in space and time. High spatial densities are (cheaply) generated by focusing a laser beam through a high numerical aperture (NA) objective. Concentration in the time domain requires the use of (expensive) lasers that emit 'ultrashort' pulses (less than a picosecond long) with correspondingly high peak intensities. For laser pulses of width τ occurring at a rate f_R, the signal is enhanced by a factor of $1 / (\tau f_R)^{n-1}$ compared to continuous-wave illumination, where n is the number of photons involved in the elementary process. Lasers typically used in 2PLSM provide 100-fs pulses at about 100 MHz, with a 'two-photon advantage'[1] of about 10^5.

Other nonlinear effects

Multiphoton absorption is but one of several possible nonlinear interactions[7]. Another is optical-harmonic generation, in which two or more photons are 'simultaneously' scattered, generating a single photon of exactly twice (thrice, and so on) the incoming quantum energy (Fig. 1a). Harmonic generation requires no actual absorption but is enhanced near a resonance, albeit at the expense of parasitic absorption[6]. It also differs from multiphoton absorption in that it is a coherent, that is, phase-preserving process, which causes speckles, possible cancellation, predominantly forward-directed emission and supralinear dependence on the chromophore density. In practice, only second-harmonic[6] and third-harmonic generation[19,20] have been used. Second-harmonic (but not third-harmonic) generation depends on the absence of inversion symmetry, which not only requires that individual molecules are inversion-asymmetric (as most biological molecules are) but also that they are spatially ordered. Second-harmonic generation has, therefore, been useful for investigating ordered structural protein assemblies such as collagen fibers[21]or microtubuli[22]. Similarly, dyes that are incorporated preferentially in one leaflet of the plasma membrane can be used to detect membrane voltage[23,24]. A further process used for microscopy is 'coherent anti-Stokes Raman scattering' (Fig. 1a), which is sensitive to molecular vibration states and can be used to detect the presence of specific chemical bond types[25,26].

Why nonlinear is more than linear

All nonlinear microscopy techniques require expensive pulsed laser systems to achieve sufficient excitation rates. Two major advantages make the investment worthwhile. First, because multiple excitation photons combine their quantum energies in nonlinear microscopy, the photons generated (or the transitions excited) have higher energies than the excitation light making emission 'bluer' than the excitation, which is different from traditional fluorescence. For commonly used fluorescent markers, multiphoton absorption occurs in the near-infrared wavelength range (700–1,000 nm), whereas emission occurs in the visible spectral range. Near-infrared light not only penetrates deeper into scattering tissue (Box 1) but is also generally less phototoxic owing to the lack of significant endogenous (one-photon) absorbers in most tissues[27].

The second major advantage of two-photon absorption and, in fact, of all nonlinear contrast mechanisms, is that the signal (S) depends supralinearly ($S \propto I^n$) on the density of photons, that is, the light intensity (I). As a consequence, when focusing the laser beam through a microscope objective, multiphoton absorption is spatially

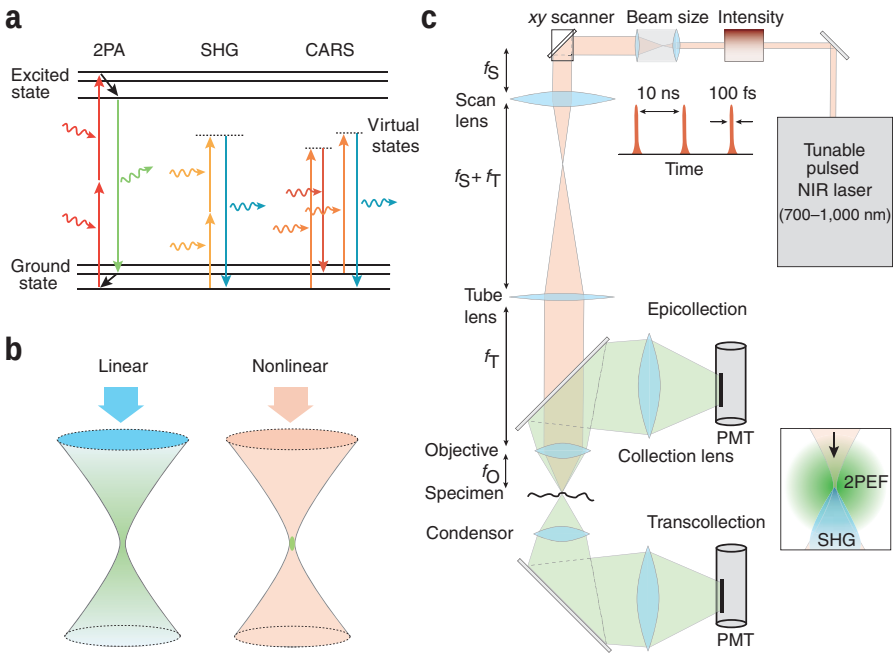

Figure 1 | Nonlinear optical microscopy. (**a**) Jablonski diagram, illustrating two-photon absorption (2PA), second-harmonic generation (SHG) and coherent anti-Stokes Raman scattering (CARS). Note that in second-harmonic generation and Raman scattering no actual electronic excitation takes place. (**b**) Spatial confinement of signal generation with nonlinear excitation. Visible ('blue-ish') light is used for excitation in single-photon microscopy, whereas near-infrared ('red-ish') light is used in 2PLSM. In single-photon microscopy an entire cone of fluorescence light (green) is generated, whereas nonlinear signal production is localized to the vicinity of the focal spot. (**c**) Generic nonlinear laser-scanning microscope. A laser source provides near-infrared ultrashort pulses; intensity and beam size are adjusted before coupling the laser beam to the microscope. The focal lengths of the scan lens (f_S), the tube lens (f_T) and the objective (f_O) are indicated. Two-photon excited fluorescence (2PEF), which is isotropically emitted (inset), can be collected in epi- and/or trans-collection mode, using whole-area detection by photomultiplier tubes (PMTs). Forward-directed optical-harmonic and Raman signals are detected in transcollection mode in transparent samples. For *in vivo* experiments epicollection is used exclusively.

confined to the perifocal region (Fig. 1b). The absence of multiphoton absorption in out-of-focus planes contrasts with confocal microscopy, where (single-photon) absorption occurs within the entire excitation light cone. The lack of out-of-focus excitation in nonlinear microscopy further reduces photodamage and thus increases tissue viability, which is crucial for long-term imaging[28]. Localization of excitation also provides excitation-based three-dimensional resolution with no need for spatially resolved detection through a confocal pinhole. By the same token, multiphoton absorption allows highly localized photomanipulations, such as photobleaching and photolytic release of caged compounds, within femtoliter volumes[29–31], which, however, is beyond the scope of this review.

Localization of excitation is maintained even in strongly scattering tissue because the density of scattered excitation photons generally is too low to generate significant signal, making nonlinear microscopy far less sensitive to light scattering than traditional microscopy (Fig. 2). This is of paramount importance for deep imaging, because it means that all fluorescence photons are known to originate from near the focus and thus can provide useful signal. The best detection strategy therefore becomes: collect as many photons as possible, wherever they seem to come from, but look at their color. Scattering does, however, increase the spatioangular range (the phase space) within which fluorescence light emerges from the tissue so that special detection optics is needed to optimize fluorescence collection from deep foci.

BOX 1 LIGHT SCATTERING IN BIOLOGICAL TISSUE

In most biological tissues absorption of light is negligible compared to scattering, particularly in the near-infrared wavelength range. Scattering is the deflection of a light 'ray' from its original direction; if the photon energy stays unchanged, it is termed 'elastic'. Elastic scattering depends on refractive index inhomogeneities, which are present even in glass but are much stronger in tissue because cells are a heterogeneous mixture of molecules and supramolecular structures with varying molecular polarizabilities. The strength of scattering is described by the 'mean free path' (l_s), the average distance between scattering events. The likelihood and angular distribution of scattering depend on refractive index variation, object size and wavelength λ. For very small objects (such as isolated atoms or molecules in a gas) scattering is nearly isotropic and strongly wavelength-dependent ($\propto \lambda^{-4}$; 'Rayleigh scattering'). For objects comparable in size to the wavelength (as in cells) scattering is directed mostly in the forward direction. This can be quantified by the anisotropy parameter (g) or by the 'transport mean free path', $l_t = l_s / (1 - g)$, which is the distance after which 'direction memory' is lost. Measurements in brain gray matter yielded values for l_s of 50–100 µm at 630 nm in extracted tissue[50,51] and of about 200 µm at 800 nm *in vivo*[43,53]. Scattering decreases with wavelength albeit less than expected for Rayleigh scattering[43]. The anisotropy parameter generally is high (≈0.9) in brain tissue[51].

In nonlinear optical microscopy only ballistic (non-scattered) photons contribute to signal generation in the focal volume. The ballistic power follows a Lambert-Beer–like exponential decline with imaging depth z

$$P_{\text{ball}} = P_0 \, e^{-z/l_s} \quad (1)$$

with length constant l_s and surface power P_0. Because of the quadratic intensity-dependence in 2PLSM, the fluorescence signal declines as

$$F_{\text{2PE}} \propto (e^{-z/l_s})^2 = e^{-2z/l_s} \quad (2)$$

Conversely, we need an exponentially increasing laser power entering the surface ($P_0 \propto e^{z/l}$) to maintain the same ballistic intensity at the focus. The reduction in focal intensity depends on l_s and not l_t, because even a small deflection from the original path causes a ray to miss the focus (**Fig. 2**). In contrast, the forward-directed angular distribution of scattering is important for the calculation of the near-surface background[103] (P. Theer and W.D., unpublished data). Both l_s and g depend not only on tissue type but can change substantially with age and upon removal of the tissue from the animal[43]. Surface scattering can become important if the beam crosses between media with substantially different refractive indices, for example when imaging through the skull.

Scattering of fluorescence photons is important for the detection process. Because of the short mean free path of visible light, the ballistic fraction becomes quickly irrelevant with increasing focal depth. For sufficient depth, multiply scattered fluorescence light leaves the sample from a diffusely radiating region on the surface, which has a full-width-at-half-maximum intensity (FWHM) of about 1.5× the focal depth, independent of the scattering length[44].

A TWO-PHOTON MICROSCOPE SETUP

In many respects, a 2PLSM is similar to a confocal microscope. The main differences are the excitation laser and the detection pathway. Commercial confocal microscopes can be converted into multiphoton microscopes[8], but major modifications and partial rebuilding may be required to achieve optimal performance, especially for deep imaging. Alternatively, the microscope can be custom built, which is cheaper but requires technical expertise or help from specialized companies. Custom-built microscopes typically lack a microscope corpus, a design that is advantageous for *in vivo* imaging because it provides space for placing the animal, and imposes fewer constraints on the size and position of the detectors. The availability of laser-scanning software[32,33] facilitates such custom designs. Here we only describe the basic microscope design; detailed instructions are available elsewhere[5,33–35].

A multiphoton microscope requires a pulsed laser source (Fig. 1c). Historically, the use of nonlinear light-matter interactions in a microscope only became possible after the development of ultrafast pulsed lasers (for a collection of reprints see 36). Whereas the first two-photon images[8] were taken using a lab-built laser system, suitable near-infrared femtosecond laser systems have now been commercially available for more than a decade. Most widely-used is the Titanium-sapphire (Ti:sapphire) oscillator, with a repetition rate (~100 MHz) that matches typical fluorescence lifetimes, thus balancing excitation efficiency and onset of saturation. The wavelength can

be tuned over a large range (670–1,070 nm), allowing the excitation of many fluorophores used in biology[18]. Key parameters that have to be considered when choosing a laser system are available power at the desired wavelength and pulse length. An optimal pulse length, however, cannot be strictly defined. Depending on the microscope design, relatively short pulses (<100 fs) at the laser output may end up as longer pulses at the sample than initially longer pulses will end up because they are broadened by dispersive optical glass components in the excitation path to a larger extent. Dispersive broadening can be precompensated by a prism or grating arrangement[37,38], thus restoring the initial pulse width at the sample and maximizing two-photon absorption. Another complicating factor is that, at least at high power, photobleaching and photodamage depend more-than-quadratically on excitation intensity[39–41]. Hence, for a given microscope setup and specimen, an optimal pulse length (or even pulse shape[42]) may have to be empirically determined, requiring a compromise between fluorescence yield and photodamage.

Compact Ti:sapphire laser systems are now available, no longer requiring user adjustments and providing computer-controlled wavelength tuning over a broad range. Although these laser systems are more user-friendly than a mercury arc lamp, it is still helpful to understand the characteristics of the laser beam, in particular if one aims to optimize the system for deep imaging. The available output power is one of the limiting factors for the maximum imaging depth but the average power (~1W) provided by these commercial systems over the central portion of the tuning range is sufficient for most applications, even with losses in the optical pathway.

The excitation pathway of a typical multiphoton microscope is as follows (all optics should be optimized for near-infrared light). Starting from the laser, the beam is expanded using a telescope (using either curved mirrors or lenses) followed or preceded by a laser intensity modulator (Fig. 1c). Because the laser beam is linearly polarized, the intensity can be adjusted easily, albeit slowly, by using a $\lambda/2$ waveplate and a polarizer. Alternatively, acousto- or electro-optical devices can be used, providing high extinction ratios and permitting rapid intensity changes. Such devices can also be used to automatically compensate for power loss with depth if the scattering length in the tissue is known (Box 1). The beam is then scanned by a *xy*-deflection module (usually a pair of galvanometric scanners) and further expanded by the combination of scan and tube lens in order to 'fill' the back aperture of the microscope objective, which focuses the light into the sample.

Although the descanned confocal detector pathway (not shown in Fig. 1c) can be used to obtain two photon–excited fluorescence images in clear specimens, clipping at the pinhole will decrease the available signal by several orders of magnitude deep in scattering specimens. Hence a simpler but better detector arrangement is used in nonlinear microscopy to capture as many of the potentially highly scattered signal photons as possible. In most systems a 'whole-area' epi-detection scheme is used, with all light that is collected by the objective also guided onto the detector[1,33,34,43,44]. For small or transparent specimens *trans*-collection through a high-NA condensor can be used instead or, better, in addition, capturing even more light (Fig. 1c). Because of the preferentially forward-directed signal, trans-collection is the principal detection mode in optical-harmonic generation and Raman scattering. In deep, scattering specimens, however, no light will penetrate, and epicollection is the only mode that can be used. Epicollection results in surprisingly little signal loss provided the detector's field of view is large enough because most signal photons eventually leave the tissue surface after multiple scattering events. For optical-harmonic generation and Raman scattering, the detection field of view needs to be especially large because the initially forward-propagating light has to 'turn around' first (Fig. 2).

OPTIMIZATION FOR DEEP IMAGING

We now consider how fluorescence generation and detection can be optimized for deep imaging and what fundamentally limits the imaging depth.

Excitation wavelength

To look deep inside tissue sufficient signal needs to be generated, which means that sufficient light needs to reach the focus without being scattered (the 'ballistic' fraction). Less-scattering long-wavelength light thus should allow deeper penetration (Box 1). The optimal wavelength for deep tissue imaging is, however, also affected by the two-photon absorption spectrum of the fluorophores used and by the fact that less power is available at the extremes of the laser tuning range.

Beam size

Loss of excitation power, for example, by clipping at apertures in the light path, lowers the achievable maximum depth. Although many of the lenses in the beam path will allow the passage of larger beams than specified, this is not true for the back aperture of the objective lens, which defines the NA and thus determines the achievable spatial resolution (Box 2). Because the radial intensity profile of a laser beam is Gaussian-shaped, an exact match to an aperture is impossible, and a compromise between resolution and transmitted power has to be found[33]. The width of a Gaussian beam is often defined

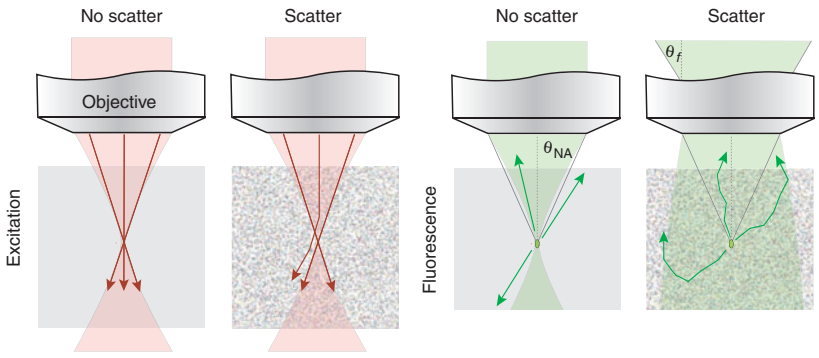

Figure 2 | Signal generation and fluorescence collection in clear tissue (no scatter) and in scattering tissue (scatter). In clear tissue all excitation light reaches the focus, but in scattering tissue, scattering (even by a small angle) causes light rays to miss the focus and be lost to signal generation. This leads to a roughly exponential decrease in excitation with depth. In clear tissue only fluorescence light rays initially emitted into the collection cone, determined by the objective's NA, can be detected, but in scattering tissue fluorescence light is (multiply) scattered and may even 'turn around'. Fluorescence light apparently originates from a large field of view but a larger fraction than in the nonscattering case is actually within the angular acceptance range θ_f of the objective.

BOX 2 IMAGE FORMATION AND SPATIAL RESOLUTION

Image formation in a microscope is described using the image of a point (for example, of a fluorophore), the so-called point-spread function (PSF). The image of any object is obtained convolving the object intensity distribution with the PSF. The three-dimensional PSF depends on the wavelength and the NA and, for an aberration-free lens of circular aperture, is given by[104]

$$\mathrm{PSF}(v,u) = \left| 2\int_0^1 P(\rho)\, J_0(v\rho)\exp(iu\rho^2/2)\rho\, d\rho \right|^2 \qquad (3)$$

J_0 denotes the zero-order Bessel function and $v = k(\mathrm{NA})r$ and $u = k(\mathrm{NA})^2 z$ are radial and axial normalized optical coordinates with the wave number $k = 2\pi / \lambda$. For a confocal microscope the detection pinhole adds a second PSF for the detection side. Assuming an ideal pinhole and similar wavelengths for illumination and fluorescence the effective PSF is

$$\mathrm{PSF}_{\mathrm{confocal}} = \mathrm{PSF}_{\mathrm{illumination}} \times \mathrm{PSF}_{\mathrm{detection}} \approx \mathrm{PSF}^2(v,u) \qquad (4)$$

For 2PLSM with whole-area detection the effective PSF is the square of the illumination PSF

$$\mathrm{PSF}_{\mathrm{two\text{-}photon}} = (\mathrm{PSF}_{\mathrm{illumination}})^2 \approx \mathrm{PSF}^2(v/2, u/2) \qquad (5)$$

with $v/2$ and $u/2$ indicating an about doubled illumination wavelength compared to confocal. Spatial resolution can be quantified using the width of the effective PSF (approximate expressions for PSF widths in 2PLSM are available[5]). Because of the longer excitation wavelength used in 2PLSM, the theoretical PSF width is larger in 2PLSM than in confocal microscopy. In practice, however, the achievable spatial resolutions are similar because finite-sized pinholes have to be used in confocal microscopy, broadening the effective PSF[105].

The resolution also depends on the intensity distribution in the back aperture of the objective and a pupil function $P(\rho)$, which needs to be included (**Fig. 3**). $P(\rho) = 1$ for uniform illumination and is $\exp(-\rho^2 / T^2)$ for a Gaussian beam (T is the fill factor $D_{\mathrm{Beam}} / D_{\mathrm{BA}}$ with D_{Beam} the $1/e^2$-intensity width and D_{BA} the back-aperture diameter).

by where intensity drops to $1/e^2$ (13.7%). With a fill factor of one, defined here as the $1/e^2$-intensity width being equal to the back-aperture diameter, power transmission is 86% (Fig. 3). The lateral and axial resolution (defined, for example, by the 1/e-width of the radial and axial profile of the focal spot[5]) are nearly unchanged in this case compared to uniform illumination (8% and 4% increases, respectively). A further reduction of beam size improves power transmission but broadens the focal volume as the 'effective' NA is reduced (Fig. 3). The resolution loss is, however, smaller than it would be for a 'top-hat' beam because for a Gaussian profile large-angle rays are still present up to the nominal NA of the objective. Note that large-angle rays are more likely to be scattered than central rays simply because they travel a longer distance to the focus, which leads to a reduction of the effective NA with increasing depth in scattering tissue.

For objects that are large compared to the focal volume, a reduction of the effective NA does not lead to a reduction in the total two-photon excited fluorescence[45]; smaller structures will, however, become dimmer. Underfilling the back aperture also lowers the peak intensity, potentially reducing photobleaching and photodamage, which have been found to have a more-than-quadratic intensity dependence in some cases[39–41]. Finally, the narrower light cone of a lower effective NA is less likely to run into obstacles (for example, blood vessels) as it penetrates the tissue.

Pulse width

A complicating factor is that ultrashort pulses are broadened ('dispersed') while propagating in material, reducing the two-photon absorption efficiency. The underlying physical principle is that longer-wavelength ('red') components of the pulse spectrum travel faster in optical materials than short-wavelength ('blue') components, so that the pulse is lengthened and 'chirped' (frequency-modulated). It is possible to compensate for the group-delay dispersion of the

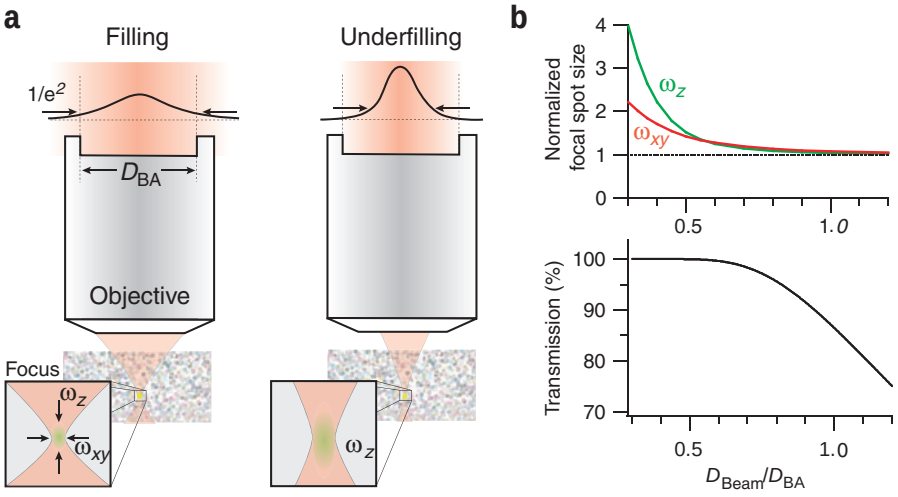

Figure 3 | Beam size adjustment relative to the objective's back aperture. (**a**) 'Matched' filling of the back aperture with an expanded beam (fill factor of one; power transmission 86%; left). In this case most of the NA is used and almost diffraction-limited resolution is reached. Underfilling of the back aperture (right). The beam is expanded less to optimize power transmission. Because a lower effective NA is used, spatial resolution is reduced. (**b**) Focal spot size and power transmission as a function of the fill factor, the ratio between D_{Beam} ($1/e^2$-width) and D_{BA}. Radial width (ω_{xy}) and axial width (ω_z) of the focal volume are normalized to the values for a uniformly filled back aperture. For fill factors around 0.7, nearly all power is transmitted with only minor losses in lateral and axial resolution.

microscope by giving the short-wavelength components a sufficient head start (negative 'prechirp') so that blue and red components arrive at the sample at the same time, restoring as-short-as-possible ('band-limited') pulses at the focus. Such compensation is useful if average power is limiting, for example, because of availability or single photon–induced damage. Prechirping can be achieved by using grating or prism arrangements, which first spatially separate the different-wavelength components, then impose different path lengths, and finally recombine the spectral components. Most commonly the laser beam double-passes a pair of prisms or gratings, the spacing of which determines the amount of negative prechirp[37,38]. A disadvantage of prechirp units is that their optical surfaces can lead to power losses.

Pulse repetition rate

The 'two-photon advantage' can also be increased by lowering f_R while maintaining average power levels. Because in mode-locked lasers f_R is determined by the optical resonator geometry (in most commercial systems around 100 MHz), it cannot easily be changed by a substantial factor. Much reduced repetition rates are provided by regenerative amplifiers, which amplify a submultiple of pulses from an oscillator. As a consequence the peak power is increased by as much as 10^8 in extreme cases at the expense of lowering the repetition rate to around 1 Hz[46]. For imaging applications at least one pulse per pixel is needed, however, limiting the reduction in f_R to about a factor of 1,000 (assuming 10-µs pixel dwell time). This approach can be used to enhance depth penetration[47] and has been demonstrated for *in vivo* imaging[14].

Correcting for tissue inhomogeneities

Signal generation is strongly affected if the focus quality is degraded by distortion of the incoming wave front. Such distortions are due to inhomogeneity of the refractive indices within the tissue, as caused for example by blood vessels or clusters of cell bodies acting as microlenses. Wavefront distortions can—if they can be measured[48]—be corrected[49] by using wave-shaping elements such as deformable mirrors.

Fluorescence collection

As important, or perhaps even more important, as the maximization of signal generation is the optimization of collection and detection efficiencies. Because scattering is more severe for shorter wavelengths, the contribution of ballistic fluorescence photons is minor beyond about one scattering mean-free-path (50–90 µm at 600 nm in brain gray matter[50,51]), and is negligible several hundred microns deep into brain tissue. Hence the confocal detection pathway becomes useless and attention has to be paid to the detection of scattered light, which emerges from the tissue surface spanning an area that is wider than the focus is deep (Fig. 2). Therefore, even with a small imaged field of view, efficient fluorescence detection requires a large detected field of view[43,44]. Because a large field of view corresponds to low magnification, special objectives that combine high NA with low magnification have particularly high collection efficiencies[43]. For a large field of view, the post-objective detection pathway has to be carefully designed to guide all light onto the detector (Fig. 1c). A large spatio-angular spread also rules out the use of certain types of detectors—such as photon-counting avalanche photodiodes, which have some of the highest detection quantum efficiency for fluorescence but a small area—and of spectrometer detectors. *In vivo* two-photon microscopes thus use photomultiplier tubes, available with large sensitive areas and reasonable quantum efficiencies.

The depth limit

The maximum achievable imaging depth is proportional to the scattering mean-free-path and depends logarithmically on available laser power, two-photon advantage and collection efficiency[43]. With a laser oscillator providing ~100-fs pulses, the maximum depth usually is limited by the available average power (1 W average power allows imaging depths of about 600–800 µm in the neocortex)[52–56]. When a regenerative amplifier is used, it is possible to image deeper (up to 1 mm in the neocortex)[14]. Eventually, however, fluorescence generated near the sample surface becomes a limiting factor[14]. The resulting contrast reduction might be impossible to overcome in samples with a wide fluorophore distribution as, for example, in transgenic mice with extensive GFP expression. The achievable imaging depth also strongly depends on other tissue properties such as microvasculature organization, cell body arrangement, collagen or myelin content, which will more-or-less degrade the laser focus and limit signal generation deep inside the tissue. If deeper structures need to be reached and if less-scattered longer wavelengths cannot be used, mechanical penetration or removal[57] of overlying tissue may be necessary. Efforts in this direction have been made using very narrow objective lenses made from gradient-index (GRIN) material[58–61].

LOOKING INSIDE LIVING TISSUE

The special advantages of 2PLSM for imaging deep within intact tissue have led to a rapid expansion of its use in various fields of biological research. 2PLSM is now used for high-resolution imaging in various organs of living animals. Here we summarize additional aspects important for *in vivo* imaging using mainly examples of cellular and subcellular imaging in the intact brain.

In vivo labeling techniques

For fluorescence imaging, structures of interest need to be labeled unless they are autofluorescent[13,62]. *In vivo* labeling techniques for staining cells in living tissues have greatly advanced. 'Traditional' synthetic dyes still are indispensable and can be introduced by a variety of methods: injection into the blood stream to label vasculature, for example, to measure blood flow in the brain[53] or the kidney[11]; filling of individual cells via recording electrodes[52,63] (Fig. 4a); uptake and anterograde transport of dextran-conjugated dyes in axons[64,65]; high-affinity binding of certain dyes to protein aggregates[66]; cell-specific spontaneous uptake of water-soluble dyes[56]; and bulk-loading of membrane-permeable calcium indicators[67]. Cells can also be labeled *ex vivo* and introduced back into mice[10].

Fluorescent proteins can be introduced using molecular genetics (for reviews see[68,69]). Widespread but cell-specific labeling can be achieved in transgenic animals expressing anatomical markers[70] or functional indicators[71,72]. Viral systems allow local expression, either short-term but less cell-specific[73,74], or long-term under control of specific promoters[75]. Different approaches can be combined to achieve multicolor labeling of various tissue elements.

Monitoring cell structure and function

Once cells of interest are labeled, various preparations and procedures can be used to study structural and functional dynamics. For short-term studies of the brain a cranial window is opened above the area of

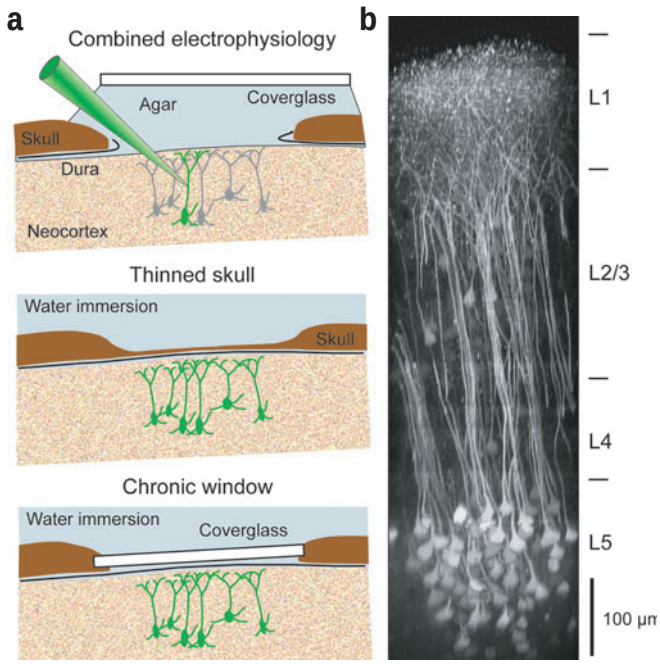

Figure 4 | *In vivo* two-photon imaging in the intact neocortex. (**a**) Different types of brain access. Open cranial window with the *dura mater* removed so that micropipettes for cell labeling and electrophysiological recordings can be inserted (top). Pulsation of the exposed brain is reduced by covering the craniotomy with agar and a coverglass. Thinned-skull (20–40 µm thickness) preparation (middle). Cellular structures are either prelabeled (for example, with fluorescent proteins in transgenic mice) or stained through a tiny hole lateral to the thinned area. Chronically implanted glass window replacing the skull (bottom). Agar is used underneath the window for stabilization. (**b**) Example of deep two-photon imaging in mouse neocortex. Maximum-intensity side projection of a fluorescence image stack, obtained in a transgenic mouse expressing Clomeleon, a genetically-encoded chloride indicator[101], under the control of the Thy1-promoter[102], preferentially in deep layer 5 (L5) pyramidal cells. Data were taken with a 10 W pumped Ti:sapphire oscillator using a 40×, NA 0.8 water-immersion lens (Zeiss). Note that nearly the entire depth of the neocortex can be imaged.

interest, which also provides access for recording electrodes (Fig. 4a). Other organs are surgically exposed in a similar manner or, as in the case of kidney, are exteriorized[11]. A general problem for *in vivo* imaging is motion induced by heart beat and breathing. Therefore, tissue pulsation should be dampened as much as possible, for example, by covering or embedding the exposed organ with agar. Tight control of the anesthesia or artificial respiration can help to alleviate pulsation. For time-lapse imaging of cell structures, we recommend acquiring small subvolumes (image stacks of 10 to 20 focal planes) in anticipation of lateral or focal drift, which can then be corrected offline using correlation methods. Image acquisition can also be synchronized to the heartbeat by triggering individual frames using a simultaneously recorded electrocardiogram, to ensure that all images have the same phase relationship to the heart beat[76].

For long-term imaging over days to months, animals are multiply reanesthetized and image stacks of the same subvolume are acquired. In the brain, these experiments are performed either through the thinned skull[66,77–79] or through a chronically implanted glass window[80–82] (Fig. 4a). In cancer research, a dorsal skin-fold chamber with a glass window is used for imaging implanted tumors[15]. To repeatedly find the same structure (for example, a cell, a blood vessel, an amyloid plaque or even a synapse), stable anatomical landmarks, such as the surface blood vessel pattern can be used.

Functional imaging from neuronal dendrites in the intact neocortex has, so far, still required the introduction of synthetic calcium indicators via electrodes[52,54,55,63,83,84], which has the advantage of providing additional *in vivo* intracellular electrophysiological data. The combination of two-photon optophysiology with electrophysiology[85] will be crucial for studying synaptic integration and single-cell computation in living animals. Great hope still rests on the *in vivo* application of genetically-encoded functional indicators[69,71,72,86,87].

Imaging cellular network dynamics

The ability to label entire cell populations with calcium indicator in living animals, using a rather generally applicable bulk dye-injection method[67], has allowed two-photon imaging of neural and glial network activity with cellular resolution. Somatic and dendritic calcium transients, for example, have revealed spontaneous and evoked activity patterns in the mammalian neocortex[67,88], now with single-spike resolution[89], as well as in the cerebellar cortex[90] and in zebrafish[91,92]. Calcium signals are also found in the neuropil, providing additional information about the input activity in afferent pathways[89,90]. Because bulk-loading does not discriminate well between cell types, specific counterstaining with synthetic or genetically encoded markers may be necessary to highlight particular cell types[56].

Imaging of population activity in neuronal networks pushes present scanning technology to its limit because fast acquisition rates are required to simultaneously measure activity in many cells. Although resonant galvanometric scanners[93] and acousto-optical deflectors[94] can achieve video-rate full-frame acquisition (30 frames/s) of a single optical plane, a further technological challenge is the equally fast recording of cells distributed in three dimensions.

Visualization of pathological states

In vivo imaging is increasingly applied to study tumorgenesis, immune responses and various brain diseases. For example, the evolution of senile Alzheimer disease plaques[66,95], their effects on neighboring neuronal structures[96] and the effectiveness of potential treatments[97] can be followed over months. The ability to image microglial cells in the neocortex opens new possibilities to study their role in a variety of brain diseases[76,98].

CONCLUSIONS AND OUTLOOK

The main strength of 2PLSM and other nonlinear microscopy techniques is the ability to maintain resolution and contrast within scattering tissue. This has permitted, in many fields for the first time, direct visualization of the normal behavior of cells in their natural environment, as well as their response to systematic manipulations. The use of 2PLSM is particularly powerful in neuroscience, where one ultimately wants to correlate cellular activity patterns with the animal's experience and behavior. Moreover, *in vivo* two-photon imaging allows longitudinal studies of structural and functional changes in the same animal over long periods of time (potentially over years). Cellular behavior thus can be put into the larger context, both spatially and temporally.

What will the near future bring? *In vivo* applications of 2PLSM will expand further into other fields, taking advantage of user-friendly laser systems and of ongoing technological developments such as the use of regenerative amplifiers, extended application of optical harmonic generation and other nonlinear effects, and microscope miniaturization. Miniaturized, fiber-based microscopes will allow imaging in freely moving animals[99]. Moreover, flexible submillimeter-sized microscope probes[58–61] may be used to reach deeper into the tissue, beyond the depth limit set by surface-generated background, albeit using a more invasive endoscopic approach. In neuroscience, the direct optical measurement of electrical potentials using two-photon excitation of voltage-sensing dyes[100] or second-harmonic signals[23,24] could have a large impact.

ACKNOWLEDGMENTS

We thank T. Kuner, G. Augustine and G. Feng for providing the Clomeleon mouse and W. Göbel for help with numerical calculations.

COMPETING INTERESTS STATEMENT

The authors declare competing financial interests (see the *Nature Methods* website for details).

Published online at http://www.nature.com/naturemethods/
Reprints and permissions information is available online at http://npg.nature.com/reprintsandpermissions/

1. Denk, W., Piston, D.W. & Webb, W.W. Two-photon molecular excitation in laser-scanning microscopy. In *Handbook of Biological Confocal Microscopy* 2nd edn. (ed. Pawley, J.B.) 445–458 (Plenum Press, New York, 1995).
2. Denk, W. & Svoboda, K. Photon upmanship: why multiphoton imaging is more than a gimmick. *Neuron* **18**, 351–357 (1997).
3. So, P.T., Dong, C.Y., Masters, B.R. & Berland, K.M. Two-photon excitation fluorescence microscopy. *Annu. Rev. Biomed. Eng.* **2**, 399–429 (2000).
4. Helmchen, F. & Denk, W. New developments in multiphoton microscopy. *Curr. Opin. Neurobiol.* **12**, 593–601 (2002).
5. Zipfel, W.R., Williams, R.M. & Webb, W.W. Nonlinear magic: multiphoton microscopy in the biosciences. *Nat. Biotechnol.* **21**, 1369–1377 (2003).
6. Campagnola, P.J. & Loew, L.M. Second-harmonic imaging microscopy for visualizing biomolecular arrays in cells, tissues and organisms. *Nat. Biotechnol.* **21**, 1356–1360 (2003).
7. Mertz, J. Nonlinear microscopy: new techniques and applications. *Curr. Opin. Neurobiol.* **14**, 610–616 (2004).
8. Denk, W., Strickler, J.H. & Webb, W.W. Two-photon laser scanning fluorescence microscopy. *Science* **248**, 73–76 (1990).
9. Cahalan, M.D., Parker, I., Wei, S.H. & Miller, M.J. Real-time imaging of lymphocytes *in vivo*. *Curr. Opin. Immunol.* **15**, 372–377 (2003).
10. Bousso, P. & Robey, E.A. Dynamic behavior of T cells and thymocytes in lymphoid organs as revealed by two-photon microscopy. *Immunity* **21**, 349–355 (2004).
11. Molitoris, B.A. & Sandoval, R.M. Intravital multiphoton microscopy of dynamic renal processes. *Am. J. Physiol. Renal Physiol.* **288**, F1084–F1089 (2005).
12. Rubart, M. Two-photon microscopy of cells and tissue. *Circ. Res.* **95**, 1154–1166 (2004).
13. Laiho, L.H., Pelet, S., Hancewicz, T.M., Kaplan, P.D. & So, P.T. Two-photon 3-D mapping of *ex vivo* human skin endogenous fluorescence species based on fluorescence emission spectra. *J. Biomed. Opt.* **10**, 024016 (2005).
14. Theer, P., Hasan, M.T. & Denk, W. Two-photon imaging to a depth of 1000 microns in living brains by use of a Ti:Al2O3 regenerative amplifier. *Opt. Lett.* **28**, 1022–1024 (2003).
15. Jain, R.K., Munn, L.L. & Fukumura, D. Dissecting tumour pathophysiology using intravital microscopy. *Nat. Rev. Cancer* **2**, 266–276 (2002).
16. Skoch, J., Hickey, G.A., Kajdasz, S.T., Hyman, B.T. & Bacskai, B.J. *In vivo* imaging of amyloid-beta deposits in mouse brain with multiphoton microscopy. *Methods Mol. Biol.* **299**, 349–363 (2005).
17. Goeppert-Mayer, M. *Über Elementarakte mit zwei Quantensprüngen* (On elementary processes with two quantum steps) *Ann. Phys.* **9**, 273–294 (1931).
18. Xu, C. & Webb, W.W. Measurement of two-photon excitation cross sections of molecular fluorophores with data from 690 to 1,050 nm. *J. Opt. Soc. Am. B* **13**, 481–491 (1996).
19. Squier, J., Muller, M., Brakenhoff, G. & Wilson, K. Third harmonic generation microscopy. *Opt. Express* **3**, 315–324 (1998).
20. Oron, D. *et al.* Depth-resolved structural imaging by third-harmonic generation microscopy. *J. Struct. Biol.* **147**, 3–11 (2004).
21. Mohler, W., Millard, A. & Campagnola, P. Second harmonic generation imaging of endogenous structural proteins. *Methods* **29**, 97–109 (2003).
22. Dombeck, D.A. *et al.* Uniform polarity microtubule assemblies imaged in native brain tissue by second-harmonic generation microscopy. *Proc. Natl. Acad. Sci. USA* **100**, 7081–7086 (2003).
23. Bouevitch, O., Lewis, A., Pinevsky, I., Wuskell, J. & Loew, L. Probing membrane-potential with nonlinear optics. *Biophys. J.* **65**, 672–679 (1993).
24. Moreaux, L., Sandre, O., Blanchard-Desce, M. & Mertz, J. Membrane imaging by simultaneous second-harmonic generation and two-photon microscopy. *Opt. Lett.* **25**, 320–322 (2000).
25. Cheng, J., Volkmer, A. & Xie, X. Theoretical and experimental characterization of coherent anti-Stokes Raman scattering microscopy. *J. Opt. Soc. Am. B* **19**, 1363–1375 (2002).
26. Wang, H., Fu, Y., Zickmund, P., Shi, R. & Cheng, J. Coherent anti-stokes Raman scattering imaging of axonal myelin in live spinal tissues. *Biophys. J.* **89**, 581–591 (2005).
27. Svoboda, K. & Block, S.M. Biological applications of optical forces. *Annu. Rev. Bioph. Biomol. Struct.* **23**, 247–285 (1994).
28. Squirrell, J.M., Wokosin, D.L., White, J.G. & Bavister, B.D. Long-term two-photon fluorescence imaging of mammalian embryos without compromising viability. *Nat. Biotechnol.* **17**, 763–767 (1999).
29. Denk, W. Two-photon scanning photochemical microscopy: mapping ligand-gated ion channel distributions. *Proc. Natl. Acad. Sci. USA* **91**, 6629–6633 (1994).
30. Svoboda, K., Tank, D.W. & Denk, W. Direct measurement of coupling between dendritic spines and shafts. *Science* **272**, 716–719 (1996).
31. Matsuzaki, M. *et al.* Dendritic spine geometry is critical for AMPA receptor expression in hippocampal CA1 pyramidal neurons. *Nat. Neurosci.* **4**, 1086–1092 (2001).
32. Pologruto, T.A., Sabatini, B.L. & Svoboda, K. ScanImage: flexible software for operating laser scanning microscopes. *Biomed. Eng. Online* **2**, 13 (2003).
33. Tsai, P.S. *et al.* Principles, design, and construction of a two-photon laser scanning microscope for *in vitro* and *in vivo* brain imaging. *In Vivo Pptical Imaging of Brain Function*. (Frostig, R.D., ed.) (CRC Press, New York, 2002).
34. Mainen, Z.F. *et al.* Two-photon imaging in living brain slices. *Methods* **18**, 231–239 (1999).
35. Majewska, A., Yiu, G. & Yuste, R. A custom-made two-photon microscope and deconvolution system. *Pflugers Arch.* **441**, 398–408 (2000).
36. Gosnell, T.R. & Taylor, A.J. (eds.) *Selected Papers on Ultrafast Laser Technology.* (SPIE Optical Engineering Press, Bellingham, 1991).
37. Treacy, E.B. Optical pulse compression with diffraction gratings. *IEEE J. Quantum Electron.* **5**, 454–458 (1969).
38. Diels, J.-C.M., Fontaine, J.J., McMichael, I.C. & Simoni, F. Control and measurement of ultrashort pulse shapes (in amplitude and phase) with femtosecond accuracy. *App. Opt.* **24**, 1270–1282 (1985).
39. Patterson, G.H. & Piston, D.W. Photobleaching in two-photon excitation microscopy. *Biophys. J.* **78**, 2159–2162 (2000).
40. Hopt, A. & Neher, E. Highly nonlinear photodamage in two-photon fluorescence microscopy. *Biophys. J.* **80**, 2029–2036 (2001).
41. Koester, H.J., Baur, D., Uhl, R. & Hell, S.W. Ca^{2+} fluorescence imaging with pico- and femtosecond two-photon excitation: signal and photodamage. *Biophys. J.* **77**, 2226–2236 (1999).
42. Kawano, H. *et al.* Attenuation of photobleaching in two-photon excitation fluorescence from green fluorescent protein with shaped excitation pulses. *Biochem. Biophys. Res. Commun.* **311**, 592–596 (2003).
43. Oheim, M., Beaurepaire, E., Chaigneau, E., Mertz, J. & Charpak, S. Two-photon microscopy in brain tissue: parameters influencing the imaging depth. *J. Neurosci. Methods* **111**, 29–37 (2001).
44. Beaurepaire, E. & Mertz, J. Epifluorescence collection in two-photon microscopy. *Appl. Opt.* **41**, 5376–5382 (2002).
45. Birge, R.R. 2-photon spectroscopy of protein-bound chromophors. *Acc. Chem. Res.* **19**, 138–146 (1986).
46. Wang, H. *et al.* Generation of 10-W average-power, 40-TW peak-power, 24-fs pulses from a Ti:sapphire amplifier system. *J. Opt. Soc. Am. B* **16**, 1790–1794 (1999).
47. Beaurepaire, E., Oheim, M. & Mertz, J. Ultra-deep two-photon fluorescence excitation in turbid media. *Opt. Comm.* **188**, 25–29 (2001).
48. Feierabend, M., Ruckel, M. & Denk, W. Coherence-gated wave-front sensing in strongly scattering samples. *Opt. Lett.* **29**, 2255–2257 (2004).
49. Booth, M., Neil, M., Juskaitis, R. & Wilson, T. Adaptive aberration correction in a confocal microscope. *Proc. Natl. Acad. Sci. USA* **99**, 5788–5792 (2002).
50. Taddeucci, A., Martelli, F., Barilli, M., Ferrari, M. & Zaccanti, G. Optical properties of brain tissue. *J. Biomed. Opt.* **1**, 117–123 (1996).

51. Yaroslavsky, A. *et al.* Optical properties of selected native and coagulated human brain tissues *in vitro* in the visible and near infrared spectral range. *Phys. Med. Biol.* **47**, 2059–2073 (2002).
52. Svoboda, K., Denk, W., Kleinfeld, D. & Tank, D.W. *In vivo* dendritic calcium dynamics in neocortical pyramidal neurons. *Nature* **385**, 161–165 (1997).
53. Kleinfeld, D., Mitra, P.P., Helmchen, F. & Denk, W. Fluctuations and stimulus-induced changes in blood flow observed in individual capillaries in layers 2 through 4 of rat neocortex. *Proc. Natl. Acad. Sci. USA* **95**, 15741–15746 (1998).
54. Svoboda, K., Helmchen, F., Denk, W. & Tank, D.W. Spread of dendritic excitation in layer 2/3 pyramidal neurons in rat barrel cortex *in vivo*. *Nat. Neurosci.* **2**, 65–73 (1999).
55. Helmchen, F., Svoboda, K., Denk, W. & Tank, D.W. *In vivo* dendritic calcium dynamics in deep-layer cortical pyramidal neurons. *Nat. Neurosci.* **2**, 989–996 (1999).
56. Nimmerjahn, A., Kirchhoff, F., Kerr, J.N. & Helmchen, F. Sulforhodamine 101 as a specific marker of astroglia in the neocortex *in vivo*. *Nat. Methods* **1**, 31–37 (2004).
57. Mizrahi, A., Crowley, J., Shtoyerman, E. & Katz, L. High-resolution *in vivo* imaging of hippocampal dendrites and spines. *J. Neurosci.* **24**, 3147–3151 (2004).
58. Jung, J. & Schnitzer, M. Multiphoton endoscopy. *Opt. Lett.* **28**, 902–904 (2003).
59. Levene, M., Dombeck, D., Kasischke, K., Molloy, R. & Webb, W. *In vivo* multiphoton microscopy of deep brain tissue. *J. Neurophysiol.* **91**, 1908–1912 (2004).
60. Jung, J., Mehta, A., Aksay, E., Stepnoski, R. & Schnitzer, M. *In vivo* mammalian brain Imaging using one- and two-photon fluorescence microendoscopy. *J. Neurophysiol.* **92**, 3121–3133 (2004).
61. Göbel, W., Kerr, J.N., Nimmerjahn, A. & Helmchen, F. Miniaturized two-photon microscope based on a flexible coherent fiber bundle and a gradient-index lens objective. *Opt. Lett.* **29**, 2521–2523 (2004).
62. Huang, S., Heikal, A.A. & Webb, W.W. Two-photon fluorescence spectroscopy and microscopy of NAD(P)H and flavoprotein. *Biophys. J.* **82**, 2811–2825 (2002).
63. Waters, J., Larkum, M., Sakmann, B. & Helmchen, F. Supralinear Ca^{2+} influx in dendritic tufts of layer 2/3 neocortical pyramidal neurons *in vitro* and *in vivo*. *J. Neurosci.* **23**, 8558–8567 (2003).
64. Wachowiak, M., Denk, W. & Friedrich, R.W. Functional organization of sensory input to the olfactory bulb glomerulus analyzed by two-photon calcium imaging. *Proc. Natl. Acad. Sci. USA* **101**, 9097–9102 (2004).
65. Kreitzer, A., Gee, K., Archer, E. & Regehr, W. Monitoring presynaptic calcium dynamics in projection fibers by *in vivo* loading of a novel calcium indicator. *Neuron* **27**, 25–32 (2000).
66. Christie, R.H. *et al.* Growth arrest of individual senile plaques in a model of Alzheimer's disease observed by *in vivo* multiphoton microscopy. *J. Neurosci.* **21**, 858–864 (2001).
67. Stosiek, C., Garaschuk, O., Holthoff, K. & Konnerth, A. *In vivo* two-photon calcium imaging of neuronal networks. *Proc. Natl. Acad. Sci. USA* **100**, 7319–7324 (2003).
68. Young, P. & Feng, G. Labeling neurons *in vivo* for morphological and functional studies. *Curr. Opin. Neurobiol.* **14**, 642–646 (2004).
69. Miesenbock, G. Genetic methods for illuminating the function of neural circuits. *Curr. Opin. Neurobiol.* **14**, 395–402 (2004).
70. Feng, G. *et al.* Imaging neuronal subsets in transgenic mice expressing multiple spectral variants of GFP. *Neuron* **28**, 41–51 (2000).
71. Hasan, M.T. *et al.* Functional fluorescent Ca^{2+} indicator proteins in transgenic mice under TET control. *PLoS Biol.* **2**, e163 (2004).
72. Wang, J.W., Wong, A.M., Flores, J., Vosshall, L.B. & Axel, R. Two-photon calcium imaging reveals an odor-evoked map of activity in the fly brain. *Cell* **112**, 271–282 (2003).
73. Kim, J. *et al.* Sindbis vector SINrep(nsP2S726): a tool for rapid heterologous expression with attenuated cytotoxicity in neurons. *J. Neurosci. Methods* **133**, 81–90 (2004).
74. Lendvai, B., Stern, E.A., Chen, B. & Svoboda, K. Experience-dependent plasticity of dendritic spines in the developing rat barrel cortex *in vivo*. *Nature* **404**, 876–881 (2000).
75. Dittgen, T. *et al.* Lentivirus-based genetic manipulations of cortical neurons and their optical and electrophysiological monitoring *in vivo*. *Proc. Natl. Acad. Sci. USA* **101**, 18206–18211 (2004).
76. Nimmerjahn, A., Kirchhoff, F. & Helmchen, F. Resting microglial cells are highly dynamic surveillants of brain parenchyma *in vivo*. *Science* **308**, 1314–1318 (2005).
77. Grutzendler, J., Kasthuri, N. & Gan, W.B. Long-term dendritic spine stability in the adult cortex. *Nature* **420**, 812–816 (2002).
78. Yoder, E.J. & Kleinfeld, D. Cortical imaging through the intact mouse skull using two-photon excitation laser scanning microscopy. *Microsc. Res. Tech.* **56**, 304–305 (2002).
79. Zuo, Y., Lin, A., Chang, P. & Gan, W.B. Development of long-term dendritic spine stability in diverse regions of cerebral cortex. *Neuron* **46**, 181–189 (2005).
80. Trachtenberg, J.T. *et al.* Long-term *in vivo* imaging of experience-dependent synaptic plasticity in adult cortex. *Nature* **420**, 788–794 (2002).
81. Majewska, A. & Sur, M. Motility of dendritic spines in visual cortex *in vivo*: changes during the critical period and effects of visual deprivation. *Proc. Natl. Acad. Sci. USA* **100**, 16024–16029 (2003).
82. Holtmaat, A.J. *et al.* Transient and persistent dendritic spines in the neocortex *in vivo*. *Neuron* **45**, 279–291 (2005).
83. Waters, J. & Helmchen, F. Boosting of action potential backpropagation by neocortical network activity *in vivo*. *J. Neurosci.* **24**, 11127–11136 (2004).
84. Charpak, S., Mertz, J., Beaurepaire, E., Moreaux, L. & Delaney, K. Odor-evoked calcium signals in dendrites of rat mitral cells. *Proc. Natl. Acad. Sci. USA* **98**, 1230–1234 (2001).
85. Margrie, T.W. *et al.* Targeted whole-cell recordings in the mammalian brain *in vivo*. *Neuron* **39**, 911–918 (2003).
86. Kerr, R. *et al.* Optical imaging of calcium transients in neurons and pharyngeal muscle of *C. elegans*. *Neuron* **26**, 583–594 (2000).
87. Reiff, D.F. *et al.* *In vivo* performance of genetically encoded indicators of neural activity in flies. *J. Neurosci.* **25**, 4766–4778 (2005).
88. Ohki, K., Chung, S., Ch'ng, Y., Kara, P. & Reid, R. Functional imaging with cellular resolution reveals precise micro-architecture in visual cortex. *Nature* **433**, 597–603 (2005).
89. Kerr, J.N., Greenberg, D. & Helmchen, F. Imaging input and output of neocortical networks *in vivo*. *Proc. Natl. Acad. Sci. USA* **102**, 14063–14068 (2005).
90. Sullivan, M.R., Nimmerjahn, A., Sarkisov, D.V., Helmchen, F. & Wang, S.S.-H. *In vivo* calcium imaging of circuit activity in cerebellar cortex. *J. Neurophysiol.* **94**, 1636–1644 (2005).
91. Brustein, E., Marandi, N., Kovalchuk, Y., Drapeau, P. & Konnerth, A. "*In vivo*" monitoring of neuronal network activity in zebrafish by two-photon Ca^{2+} imaging. *Pflugers Arch.* **446**, 766–773 (2003).
92. Niell, C.M. & Smith, S.J. Functional imaging reveals rapid development of visual response properties in the zebrafish tectum. *Neuron* **45**, 941–951 (2005).
93. Fan, G.Y. *et al.* Video-rate scanning two-photon excitation fluorescence microscopy and ratio imaging with cameleons. *Biophys. J.* **76**, 2412–2420 (1999).
94. Roorda, R.D., Hohl, T.M., Toledo-Crow, R. & Miesenbock, G. Video-rate nonlinear microscopy of neuronal membrane dynamics with genetically encoded probes. *J. Neurophysiol.* **92**, 609–621 (2004).
95. Bacskai, B.J. *et al.* Four-dimensional multiphoton imaging of brain entry, amyloid binding, and clearance of an amyloid-beta ligand in transgenic mice. *Proc. Natl. Acad. Sci. USA* **100**, 12462–12467 (2003).
96. Tsai, J., Grutzendler, J., Duff, K. & Gan, W. Fibrillar amyloid deposition leads to local synaptic abnormalities and breakage of neuronal branches. *Nat. Neurosci.* **7**, 1181–1183 (2004).
97. Lombardo, J.A. *et al.* Amyloid-beta antibody treatment leads to rapid normalization of plaque-induced neuritic alterations. *J. Neurosci.* **23**, 10879–10883 (2003).
98. Davalos, D. *et al.* ATP mediates rapid microglial response to local brain injury *in vivo*. *Nat. Neurosci.* **8**, 752–758 (2005).
99. Helmchen, F., Fee, M.S., Tank, D.W. & Denk, W. A miniature head-mounted two-photon microscope. high-resolution brain imaging in freely moving animals. *Neuron* **31**, 903–912 (2001).
100. Kuhn, B., Fromherz, P. & Denk, W. High sensitivity of Stark-shift voltage-sensing dyes by one- or two-photon excitation near the red spectral edge. *Biophys. J.* **87**, 631–639 (2004).
101. Kuner, T. & Augustine, G.J. A genetically encoded ratiometric indicator for chloride: Capturing chloride transients in cultured hippocampal neurons. *Neuron* **27**, 447–459 (2000).
102. Berglund, K., Dunbar, R.L., Psyche, L., Feng, G. & Augustine, G.J. A practical guide: Imaging synaptic inhibition with Clomeleon, a genetically encoded indicator. in *Imaging in Neuroscience and Development: a Laboratory Manual.* (Yuste, R. & Konnerth, A. eds.) (Cold Spring Harbor Press, Cold Spring Harbor, 2005).
103. Ying, J., Liu, F. & Alfano, R. Effect of scattering on nonlinear optical scanning microscopy imaging of highly scattering media. *App. Opt.* **39**, 509–514 (2000).
104. Sheppard, C.J. & Gu, M. Image formation in two-photon fluorescence microscopy. *Optik* **86**, 104–106 (1990).
105. Cox, G. & Sheppard, C.J. Practical limits of resolution in confocal and non-linear microscopy. *Microsc. Res. Tech.* **63**, 18–22 (2004).

Corrigendum: Deep tissue two-photon microscopy

Fritjof Helmchen & Winfried Denk
Nat. Methods **2,** 932–940 (2005).

The wrong reference (ref. 24) was mistakenly provided for the work on second-harmonic imaging of membrane-potential changes. The correct reference 24 is:

Moreaux, L. *et al.* Electro-optic response of second-harmonic generation membrane potential sensors. *Opt. Lett.* **28**, 625–627 (2003).

Fiber-optic fluorescence imaging

Benjamin A Flusberg, Eric D Cocker, Wibool Piyawattanametha, Juergen C Jung, Eunice L M Cheung & Mark J Schnitzer

Optical fibers guide light between separate locations and enable new types of fluorescence imaging. Fiber-optic fluorescence imaging systems include portable handheld microscopes, flexible endoscopes well suited for imaging within hollow tissue cavities and microendoscopes that allow minimally invasive high-resolution imaging deep within tissue. A challenge in the creation of such devices is the design and integration of miniaturized optical and mechanical components. Until recently, fiber-based fluorescence imaging was mainly limited to epifluorescence and scanning confocal modalities. Two new classes of photonic crystal fiber facilitate ultrashort pulse delivery for fiber-optic two-photon fluorescence imaging. An upcoming generation of fluorescence imaging devices will be based on microfabricated device components.

Fiber-optic fluorescence imaging has become increasingly versatile over the last decade as fiber-based devices have declined in size but gained in functionality. Three classes of applications in live animal and human subjects provide the primary motivations for innovation in fiber-optic imaging. First, basic research on biological and disease processes would benefit enormously from instrumentation that permits cellular imaging under conditions in which conventional light microscopy cannot be used. Many cell types reside within hollow tissue tracts or deep within solid organs that are inaccessible to optical imaging without devices that can reach such locations in a minimally invasive manner. Flexible fiber-optic devices also allow handheld imaging and imaging in freely moving animals[1]. Second, fiber devices might be implanted within live subjects for long-term imaging studies. This capability will not only benefit research on the cellular effects of aging, development or experience, but also will lead to new *in vivo* assays for testing of drugs and therapeutics. By allowing examination of cells concurrently with observation of disease symptoms and animal behavior, fiber-optic imaging will permit studies correlating cellular properties and disease outcome in individual subjects over time and could reduce the numbers of animals needed. A third set of applications concerns development of minimally invasive clinical diagnostics and surgical procedures[2]. Although much work remains, fiber-optic instrumentation has already broadened the applicability of *in vivo* fluorescence imaging.

The seeds for development of fiber optic *in vivo* imaging were planted by early uses of fiber-optics and fluorescence for chemical sensing and spectroscopy, including classic work on detection of intracellular redox states[3–5]. Use of fiber optics for remote sensing and spectroscopy remains strong today[6], and has expanded to include bioluminescence detection[7]. The recent proliferation of fluorescent probes has widened the set of potential uses for fiber-based fluorescence imaging devices, which may be classified by size into the three broad categories of microscopy, endoscopy and microendoscopy.

The simplest application of fiber-optics in microscopy is remote delivery of light[8–16], which allows the excitation light source or photodetectors to reside apart from a conventional microscope. Optical fiber also enables miniaturized or compact forms of microscopy for portable usage[1,17,18]. Flexible fiber-optic endoscopy involves optical probes that are usually a few millimeters in diameter and well suited to imaging either superficial tissues such as skin or hollow tissue cavities such as the cervix or digestive tract[19–34]. Fluorescence microendoscopy (FME) involves optical probes that are typically 0.25–1 mm in diameter for minimally invasive insertion into solid tissue. Such probes can either be mainly rigid and one to several centimeters in length, for use akin to a

James H. Clark Center for Biomedical Engineering and Sciences, Stanford University, 318 Campus Drive, Stanford, California 94305, USA. Correspondence should be addressed to M.J.S (mschnitz@stanford.edu)

PUBLISHED ONLINE 18 NOVEMBER 2005; DOI:10.1038/NMETH820

needle biopsy[35–37], or mated to flexible fiber optics[38–43]. Both types of FME have allowed cellular imaging deep within solid tissues of live mammalian subjects[2,35,37,38,42,44].

All three categories of fiber-based imaging, microscopy, endoscopy and microendoscopy, can involve the fluorescence modalities reviewed elsewhere in this issue, including one-photon epifluorescence, scanning confocal fluorescence and two-photon excited fluorescence. Many strengths and limitations of the conventional tabletop systems also characterize the corresponding fiber-optic forms (Table 1). We focus here on components and embodiments that are particular to fiber-based imaging to help readers choose and construct imaging devices best suited to their needs.

COMPONENTS

Several features of fiber-optic imaging systems are nearly universal. Optical fiber delivers illumination, and one or more lenses focus this light at the specimen plane and collect fluorescence emissions. In many cases a focusing mechanism allows adjustment of the imaging plane. For confocal and two-photon modalities, a scanning mechanism moves one or more focal spots across the field of view.

Optical fiber

Optical fiber commonly ranges from ~80 μm up to several millimeters in diameter and can perform many jobs, including light delivery and collection, as well as image transmission. How are these functions accomplished? In conventional fibers, known as step-index fibers, there are two zones with distinct indices of refraction, an outer cladding and an inner core, which enable light transmission down the fiber axis by total internal reflection[45]. A subclass of step-index fibers called single-mode fiber (SMF) guides only a single spatial mode of light (Box 1). SMF, which is widely available commercially, is well suited for illumination delivery in the scanning imaging modalities because the single spatial mode can be focused to a near diffraction-limited spot in the specimen plane, allowing high-resolution imaging. The same SMF core that delivers light can also act as a pinhole detector, rejecting out-of-focal plane fluorescence emissions[8–11,13–15,43,46,47].

Fibers that guide more than one spatial mode are called multimode fibers (Box 1). Step-index multimode fibers are better suited for fluorescence collection than SMF, because not only do they possess larger core diameters, commonly ~50 μm up to a few millimeters, but they also usually have greater numerical aperture (NA) values. All-polymer multimode fibers tend to be more flexible than their silica counterparts and are available with NA values up to ~0.5.

In a particular class of multimode fiber known as gradient refractive index (GRIN) fiber, the refractive index in the core declines approximately quadratically with radius from the central axis. Unlike in step-index multimode fibers, in GRIN fibers the different electro-

Table 1 | A comparison of fiber-optic fluorescence imaging modalities

Embodiments	Advantages	Limitations
EPIFLUORESCENCE	Ease of use, full-frame acquisition for high-speed imaging. Low-cost incoherent light source. Viewing through eyepieces or by camera.	Lack of optical sectioning, not robust to light scattering.
One-photon FME[35,79]	Proximal focusing with external objective lens.	GRIN endoscope probes are short and rigid.
Fiber-bundle epifluorescence[59]	Mechanical flexibility. Ease of handheld use.	Pixilation of image reduces resolution. Distal focusing mechanism hinders miniaturization.
CONFOCAL FLUORESCENCE	Optical sectioning. Laser source much less costly than for two-photon imaging.	Not robust to light scattering, penetration depths of ~50 μm in tissue. Distal focusing mechanism hinders miniaturization.
Single-fiber confocal[22,24,26–29,67–69]	Mechanical flexibility. Single fiber for both excitation delivery and emission collection.	Distal scanning mechanism hinders miniaturization.
Dual-axis fiber confocal[81–83]	Mechanical flexibility. High axial resolution. Long working distance optics allow post-objective scanning for large fields of view and reduced aberrations.	Distal scanning mechanism hinders miniaturization. Reduced fluorescence collection efficiency because of the low-NA collection aperture.
Fiber-bundle confocal[19,23,25,30,31,40,42]	Mechanical flexibility. Ease of handheld use. Proximal scanning mechanism facilitates miniaturization. Line scanning can enable fast frame rate imaging.	Pixilation of image reduces resolution.
TWO-PHOTON FLUORESCENCE	Optical sectioning. Reduced photobleaching and photodamage. Robustness to scattering. Penetration depths in tissue up to ~300 μm.	Cost of ultrashort-pulsed laser.
Two-photon FME[35–37]	Proximal focusing with external objective lens. Proximal scanning. Minimal pulse dispersion and SPM.	GRIN endoscope probes are short and rigid.
Single-fiber two-photon[1,38,43]	Mechanical flexibility. No pulse distortion in PBF for zero-dispersion wavelength. Reduced SPM in LMA-PCF.	Distal scanning and focusing mechanisms hinder miniaturization. Dispersion compensation may be needed.
Fiber-bundle two-photon[39]	Mechanical flexibility. Proximal scanning. Ease of handheld use.	Pixilation of image reduces resolution. Distal focusing mechanism hinders miniaturization. Dispersion compensation needed. SPM at higher pulse energies.
Multi-focal two-photon[17,18]	Mechanical flexibility. Lens array enables high-speed multi-focal imaging. No pulse distortion in PBF for zero-dispersion wavelength. Reduced SPM in LMA-PCF.	Currently too large for endoscopy. Distal scanning and focusing mechanisms hinder miniaturization. Multiple foci decrease robustness to light scattering.
Double-clad two-photon[57,58]	Mechanical flexibility. Fluorescence collection and excitation delivery achieved in one fiber. Reduced SPM in LMA-PCF.	Distal scanning and focusing mechanisms hinder miniaturization. Dispersion compensation needed.

Abbreviations: self-phase modulation (SPM); photonic bandgap fiber (PBF); large mode area photonic crystal fiber (LMA-PCF).

magnetic spatial modes comprising an image propagate at nearly the same velocity. This means that GRIN fibers can serve as lenses when cut to specific lengths (see Objective optics below), enabling remote adjustment of the focal plane in the specimen using optics placed on the opposite side of the fiber[48]. The number of guided spatial modes in a GRIN medium limits the optical resolution of the transmitted image. This situation contrasts with how a fiber bundle transmits a pixilated image composed of an array of light intensities, in which case an optical focal mechanism must reside on the fiber side proximal to the specimen (see Fiber bundles below).

Important issues arise in two-photon fiber-optic imaging concerning the remote delivery of the ultrashort optical pulses (~80–250 fs in duration) typically used for two-photon excitation (Box 1). Particularly for *in vivo* studies, it is common to use pulses of nanojoule energies for two-photon imaging up to hundreds of micrometers deep within tissue. Such brief pulses are so intense that a light-matter interaction in the glass fiber core can distort both the pulse shape and spectrum through a nonlinear process known as self-phase modulation (SPM). This effect makes it challenging to excite two-photon fluorescence efficiently using SMF[49–51]. A newly developed class of

BOX 1 OPTICAL FIBER AND ULTRASHORT PULSE DELIVERY

OPTICAL FIBER

Single mode fibers

In step-index optical fibers, the fiber core has a refractive index (n_1) that is typically 1–2% higher than that of the cladding (n_2), leading to a numerical aperture NA = $(n_1^2 - n_2^2)^{1/2}$ equal to the sine of the half-angle of the cone of light emitted from the fiber. The solutions to Maxwell's equations with boundary conditions appropriate for electromagnetic wave propagation down a cylindrically symmetric fiber dictate that a fiber with a core radius a guides only a single spatial mode of light if the wavelength λ in vacuum satisfies the inequality $V < 2.405$, where the quantity $V = (2\pi a\ \mathrm{NA})/\lambda$ is known as the 'normalized wave number'[45]. Such fibers are single-mode and have typical core diameters of ~3–7 μm for visible light.

Multimode fibers

If $V > 2.405$ the fiber can guide more than one spatial mode. The number of transmitted spatial modes increases approximately quadratically as a function of V, and so-called multimode fibers operate in the limit in which the number of guided modes is large, usually a hundred or more. Multimode fibers have core diameters of ~50 μm up to several millimeters.

GRIN fibers and lenses

In cylindrically symmetric GRIN lens and fibers the refractive index commonly varies as $n(r) = n_0(1 - g^2r^2/2)$, where r is the radius from the fiber axis, n_0 is the refractive index on axis and g is a constant parameter. In a ray description, paraxial light rays follow an approximately sinusoidal path with a period of length $P = 2\pi/g$ as they propagate down the cylindrical axis of a GRIN medium[45]. Thus, two primary determinants of the properties of a GRIN lens are the lens length and refractive index profile.

ULTRASHORT PULSE DELIVERY IN OPTICAL FIBER

Ultrashort pulses of ~80–250 fs duration and nanojoule energies are commonly used to induce two photon–excited fluorescence *in vivo*. When such pulses propagate through an optical fiber, both group velocity dispersion and self-phase modulation can distort the pulse's temporal profile and impact the efficiency of two-photon excitation, which varies inversely with pulse duration.

Group velocity dispersion

Chromatic or group velocity dispersion (GVD) occurs when different colors of light travel through optical fiber or other optical components at distinct speeds, thereby incurring differential propagation delays. In optical fiber there are two sources of GVD, known as material and waveguide dispersion. Material dispersion results from the different speeds at which each spectral component travels through silica glass[45]. Waveguide dispersion arises because a different proportion of the pulse energy at each wavelength propagates through the fiber cladding. These two components cancel at the so-called zero-GVD wavelength. Configurations of diffraction gratings[55] or prisms[56] can compensate for GVD by negatively 'pre-chirping' optical pulses—that is, giving wavelengths that travel more slowly through optical fiber a head start, so that all spectral components exit the fiber simultaneously. This counteracts GVD, which by itself yields pulses that are positively chirped and temporally broadened.

Self-phase modulation

Intense laser pulses interact with the silica core in SMF and transiently raise the local refractive index. This index rise induces a phase shift and a corresponding spectral distortion in the pulse through self-phase modulation (SPM), which occurs in a nonlinear manner that depends on the pulse's temporal profile of wavelength and intensity[45]. Because of this nonlinear dependence it is difficult to compensate for SPM, which leads to spectral narrowing and temporal broadening of negatively pre-chirped pulses propagating in SMF, for wavelengths shorter than the zero-GVD wavelength of 1.3 μm[49–51]. Hollow-core PBF (**Fig. 1a**) and LMA-PCF (**Fig. 1b**) ameliorate the problems associated with SPM and can deliver ultrashort pulses with little distortion.

Exploiting nonlinear pulse distortion

It is possible to harness nonlinear effects in optical fiber to alter the pulse spectrum for particular two-photon imaging applications[12,90,91]. Small core (~1- to 3-μm diameter) or 'highly nonlinear' photonic crystal fibers can enhance SPM-induced spectral broadening of positively chirped ultrashort pulses below the zero-GVD wavelength (**Fig. 1d**). Subsequent temporal recompression of the pulses can increase the two-photon fluorescence excitation efficiency by up to almost an order of magnitude[91]. The spectral broadening created by SPM can also enable the excitation of dyes, such as fura-2, whose two-photon absorption spectra are below the wavelength range of most common ultrashort laser sources[90].

Measurements of pulse width

A simple means of characterizing the temporal width of ultrashort pulses is to use an autocorrelator, which splits the beam between two paths and then recombines these on a nonlinear detector. Because the two pulses from the separate paths must arrive almost coincidentally at the nonlinear detector to register the maximum amplitude signal, pulse duration can be inferred from how the detector signal changes as the relative path length between the two paths varies. Other pulse diagnostics, such as frequency-resolved optical gating, can provide information about both the intensity and wavelength temporal profiles.

optical fiber known as photonic crystal or microstructured fiber can be used either to circumvent or harness SPM.

Photonic crystal fiber is named after the periodic arrays of air holes and silica glass these fibers exhibit within their internal structure (Fig. 1). Many forms of silica-core microstructured fiber guide light by a modified form of total internal reflection, in which the effective refractive index of the air-silica array in the cladding is less than that of the core. Photonic bandgap fiber (PBF) is a form of microstructured fiber that does not rely on total internal reflection for guiding light (Fig. 1a).

PBF uses diffractive effects that arise from interactions between light and internal air-silica arrays with structure at the same length scale as the wavelength. A carefully designed air-silica lattice creates a photonic bandgap analogous to an electronic bandgap in crystalline solids, which prevents light within a certain wavelength range from propagating in the cladding. An air core within such a PBF can act as a lattice defect, localizing light to the core, much as crystalline solid defects create localized electronic states. Wavelengths within the bandgap are thus contained and transmitted within the core, with the lowest-order mode typically having a Gaussian-like spatial profile[52]. PBF has transformed the possibilities for fiber-based two-photon excited fluorescence and other nonlinear optical imaging modalities, because even high-energy pulses do not undergo SPM in an air core. Moreover, within the transmission window of PBF, which is called the bandgap and usually covers a spectral range of several tens to over a hundred nanometers, there is usually a wavelength at which group velocity (chromatic) dispersion vanishes (Box 1). Pulses centered at this wavelength scarcely suffer any broadening, making PBF an excellent choice for pulse delivery[16,17,38,53,54]. For other transmitted wavelengths only tens of nanometers away, however, dispersive pulse broadening can be more severe than in conventional SMF. Application of basic methods for dispersion compensation[55] can alleviate much of such broadening (Box 1), but for fiber lengths greater than a few meters additional compensation for 'higher-order' dispersion might also be required[38,56].

A good alternative means for delivery of ultrashort pulses involves a class of microstructured fiber known as large mode area photonic crystal fiber (LMA-PCF; Fig. 1b). These low-NA fibers not only have a large core of up to ~35 μm in diameter, in which pulse intensity is much reduced compared to the ~5–6 μm core of SMF, but also are 'endlessly single mode' in that only one spatial mode propagates regardless of wavelength within the silica transparency window. The reduced intensity diminishes, but does not eliminate SPM. Group velocity dispersion can be compensated using basic approaches because higher order dispersion appears to be much less important than in current forms of PBF. An especially interesting LMA-PCF for two-photon imaging is a 'double-clad' fiber that is essentially two fibers in one and can accomplish both excitation pulse delivery and fluorescence emission collection[57,58]. An inner LMA core delivers ultrashort pulses, and together with an inner cladding also serves as the core for a surrounding multimode fluorescence collection fiber (Fig. 1c). An outer multimode fiber cladding is composed almost entirely of air, leading to a high NA for visible light collection up to ~0.6. Use of such double-clad fiber for two-photon microscopy has been demonstrated[57,58]. All types of photonic crystal fiber discussed here are commercially available.

Fiber bundles

Fiber-optic bundles consist of up to ~100,000 individual step-index fibers in a closely packed arrangement, hundreds of micrometers to a few millimeters in total diameter. Image-guiding bundles maintain the relative arrangements of the individual fibers throughout the length of the bundle, allowing transmission of an intensity image in pixilated form. Such bundles are commercially available and are commonly used for both epifluorescence[59] and scanning confocal or two-photon imaging[19,23,25,30,31,39,40,42,60–62]. However, unlike in lenses or GRIN fibers, only intensity information is transmitted. This limitation can hinder miniaturization if one desires a built-in focusing mechanism that does not require moving the entire imaging head, because such a mechanism has to be engineered within the optics proximal to the specimen[25,30,31]. Many devices based on fiber bundles lack such focal capability, sacrificing functionality for size reduction[39,40,42]. On the other hand, use of a fiber bundle facilitates miniaturization of laser-scanning modalities by allowing scanning mechanisms to reside on the side of the bundle distal to the specimen for sequential illumination of the individual fibers (Fig. 2a–c).

The main disadvantage of fiber bundles is that pixilation reduces the lateral optical resolution in the specimen plane to about twice the average core-to-core distance between fibers divided by the optical magnification of the imaging lenses. Furthermore, the thin layer of cladding between adjacent fiber cores leads to optical cross talk in which light from neighboring image pixels can leak into one another, reducing contrast. In scanning confocal imaging this problem may be reduced by use of a nonordered bundle, in which the relative fiber positions are randomized and not maintained throughout the bundle. This approach requires having to reconstruct the sample image based on knowledge of the scrambled fiber arrangement, but helps to reduce cross talk. Nonordered bundles are especially useful for laser line-scanning forms of fast confocal imaging, in which adjacent fibers at one side of the bundle are illuminated concurrently but the resulting fluorescence originates from physically separate locations in the sample[62]. In all fiber-bundle applications, calibration of the intrinsic

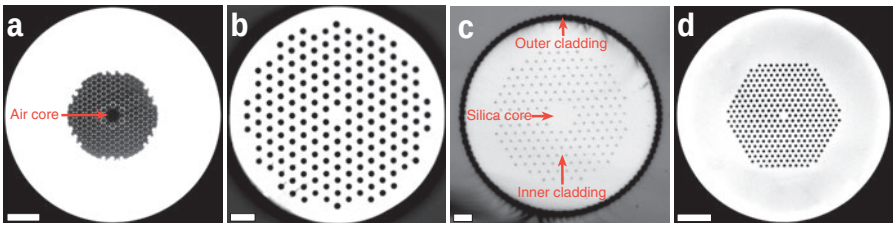

Figure 1 | Photographs of photonic crystal fibers. (**a**) Hollow-core PBF. Wavelengths within the transmission band are localized to the air core, virtually eliminating SPM. (**b**) Large-mode area photonic crystal fiber (LMA-PCF). Light guidance in the silica core is 'endlessly single mode' and the large mode area reduces SPM. (**c**) Double-clad photonic crystal fiber. A silica LMA core and a surrounding air-silica inner cladding comprise an inner lower-NA fiber that can guide ultrashort pulses with reduced SPM. An outer cladding composed nearly exclusively of air creates a higher-NA fiber that can collect fluorescence efficiently. Acrylate structural support surrounds the outer cladding and is not fully shown. (**d**) Highly nonlinear photonic crystal fiber. The small silica core can be used to harness SPM for broadening the spectrum of ultrashort excitation pulses. Scale bars, 20 μm. Photographs kindly provided by R. Kristiansen (Crystal Fibre A/S).

autofluorescence, precise position and optical throughput for each fiber in the bundle can facilitate postacquisition image processing and substantially improve image quality[42].

Objective optics

For applications without severe size constraints, a conventional microscope objective lens nearly always provides superior optical resolution and fluorescence detection efficiency. When miniaturization is required, custom high-NA (0.46–1.0)[19,23,30,31] objective lenses can be designed with outer diameters as small as 3–7 mm. Use of injection-molded plastic lenses to construct a custom objective is a particularly lightweight and economical approach[23].

The creation of minimally invasive microendoscope probes has benefited greatly from recent advances in the fabrication of GRIN microoptics. GRIN microlenses ranging from 350–1,000 μm in diameter have been used for one-photon, confocal and two-photon FME[35–40,43]. As in GRIN fiber, cylindrical GRIN lenses exhibit a refractive index that declines approximately quadratically with radius (Box 1). Compound GRIN microendoscope probes usually measure one or more centimeters in length and combine two or more GRIN lenses with different characteristics[35–37]. These are typically a 0.4–0.6 NA objective lens that enables micrometer-scale resolution and a longer relay lens that projects a real image of the specimen plane and supplies sufficient length for reaching deep tissue[35–37]. Optical aberrations in current GRIN lenses limit the resolving power to approximately twice the diffraction limit[35–38]. A detailed description of GRIN endoscope probes is available in ref. 35, and custom GRIN lenses are available from multiple vendors.

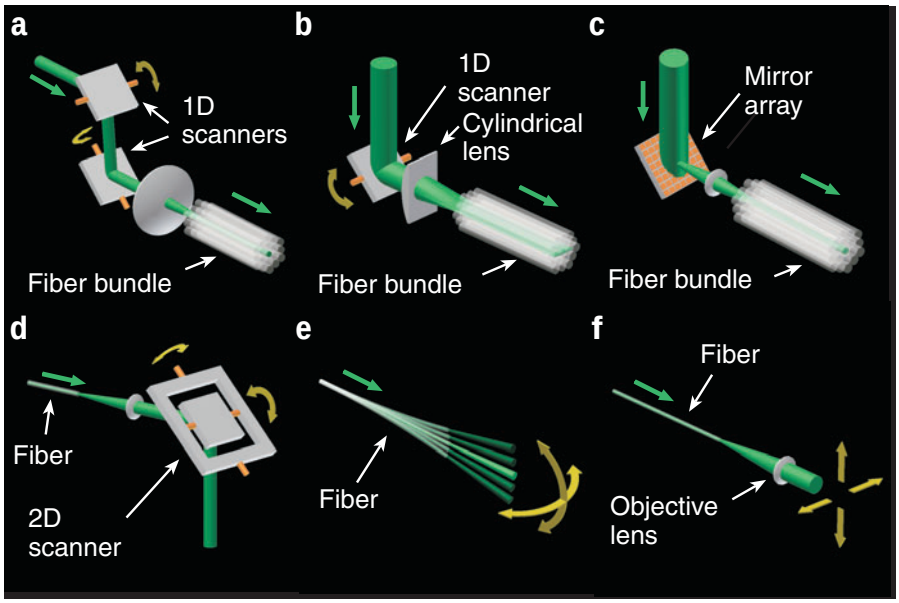

Figure 2 | Scanning mechanisms. (**a**) Proximal scanning. Cascaded galvanometer-mounted mirrors scan the excitation beam across the proximal end of a fiber bundle. (**b**) Proximal line-scanning. A cylindrical lens focuses the illumination to a line that is scanned across the face of a fiber bundle in one dimension. (**c**) Proximal scanning with a spatial light modulator, which can illuminate pixels sequentially without sweeping the beam. (**d**) Distal 2D mirror scanning. A piezoelectric driven tip-tilt mirror or a miniaturized MEMS mirror pivots in two angular dimensions. (**e**) Distal fiber tip scanning. The tip of the excitation delivery fiber is vibrated at resonance by an actuator (not shown). (**f**) Distal fiber-objective scanning. Both the fiber and the objective lens are mounted together on a cantilever (not shown) that is vibrated at resonance by an actuator.

Scanning mechanisms

It is common to speak of scanning mechanisms as being either proximal or distal to the light source. Proximal scanners are located in the illumination pathway upstream of the fiber and are used with a fiber bundle. Distal scanners are located on the fiber side distal to the light source and usually scan illumination from a single fiber over the specimen. Proximal scanning offers the benefit of separating bulky scanners from a miniaturized imaging head and typically involves a pair of galvanometer-mounted scanning mirrors (Fig. 2a)[19,23,25,30,31,39,40,42,61,62]. These can provide high image-acquisition rates (up to ~1 kHz per image line), particularly in a fast line-scanning approach that can allow video-rate imaging (Fig. 2b), and optical deflection angles up to ~40°. However, because the galvanometer approach involves sweeping the illumination across the bundle, light enters the cladding between adjacent cores during much of the scanning cycle, potentially diminishing image contrast.

Use of a spatial light modulator such as a pixilated micromirror array to illuminate each fiber sequentially, without sweeping the beam, can reduce errant excitation light (Fig. 2c)[60]. Nonetheless, much of the excitation power is lost, because although the entire modulator is illuminated with light, only a fraction of the pixels will be activated at any given moment during a scan. This loss may not pose much problem for imaging at superficial tissue depths. Both one-dimensional (1D) and two-dimensional (2D) spatial light modulators are available commercially.

The use of a single fiber for illumination delivery necessitates a distal scanning mechanism. Portable microscopy can rely on a piezoelectric-driven, 2D tip-tilt mirror (Fig. 2d), which has a lower bandwidth (~200 Hz) but a smaller footprint than cascaded galvanometers[17,18,63]. However, endoscopy and microendoscopy require more compact scanning mechanisms. One approach relies on either a piezoelectric[1,38,64] or an electromagnetically excited[65,66] actuator to drive mechanical resonance vibrations of the fiber tip (Fig. 2e). Although fiber tip scanning allows stationary imaging optics to be inserted into solid tissue[38], it can also introduce off-axis aberrations that might limit the achievable resolution. To preclude such aberrations, one can attach both the fiber and the imaging lens to a resonant cantilever and scan them together using electrostatic forces[67] or piezoelectric actuators[20,24] (Fig. 2f). Although this method needs an actuator that delivers more force, the required angular scanning range is reduced because the scanned focal spot is not further demagnified. A disadvantage of resonant scanning is that it is usually not possible to offset the center of the image field from the main optical axis without addition of another deflector.

In recent years, microfabricated microelectromechanical systems (MEMS) torsion scanning mirrors ~0.5–2 mm in diameter have emerged as versatile miniaturized scanning mechanisms (Figs. 2d and 3)[68–70]. MEMS scanners are created through sequential material etch-

ing and deposition processes analogous to those used for integrated circuit fabrication; 2D scanning involves cascaded 1D scanners or a single 2D scanner. The latter simplifies the optical design and reduces overall size. MEMS scanners that rely on electrostatic actuation are the most commonly used owing to the small size, low power consumption and high force that can be achieved. Among the electrostatic actuators, vertical comb actuators[71–73] offer greater force and angular range than parallel plate actuators[68,69]. These interdigitated silicon comb actuators provide electrostatic torque to rotate the mirror in one direction, and torsional springs supply a restoring torque (Fig. 3). Operating such scanners in DC mode permits static offsets of the field of view and mechanical angular rotations of up to ~6° (ref. 71). Alternatively, because ~1-mm-diameter MEMS mirrors have mechanical resonance frequencies in the kHz range, resonance scanning can enable video-rate imaging with large angular mirror rotations (>30°)[72], albeit at the expense of not being able to make lateral offsets in the field of view. A disadvantage of MEMS scanners is that although they are ideal for miniaturization, their fabrication requires much expertise. However, MEMS scanning mirrors are becoming commercially available.

Focusing mechanisms

Many applications benefit from having a built-in mechanism for altering the image focus without having to move the entire imaging probe. As with scanners, such mechanisms are positioned either proximal or distal to the light source relative to the fiber. Distal focusing mechanisms tend to hinder miniaturization because they are integrated with the objective optics, whereas proximal mechanisms are of conventional size and do not enter the specimen. For instance, it can be helpful to leave a GRIN microendoscope probe stationary within tissue while adjusting the image plane by moving the external microscope objective lens that also delivers illumination into the probe[35,37,74]. Because of optical demagnification between image and object planes, a focal shift of ~100 micrometers in the tissue often requires movement of focusing optics over millimeter-sized distances, beyond the range of small piezoelectric actuators. For flexible modalities that require distal focusing, one can use a hydraulic or pneumatic system to move the end of a fiber with respect to the objective optics when a fluid is injected into or withdrawn from a reservoir[25,30,31]. Another lightweight approach relies on a miniature motor to alter the distance between the fiber and the imaging optics[38]. In the future, millimeter-sized liquid lenses that alter their focus via electrowetting, will allow fast, remotely controlled distal focusing and beam steering for endoscopy and FME[75–77].

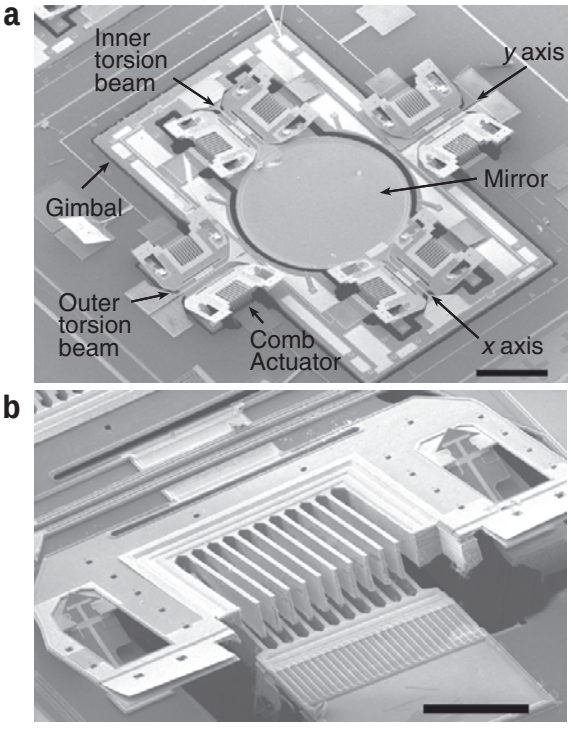

Figure 3 | An MEMS scanner. (**a**) Scanning electron micrograph of 2D MEMS vertical comb scanner. Electrostatically driven angular vertical comb actuators rotate the 1-mm-diameter mirror about the torsion beams. Gimbal mounting of the mirror and actuators allows 2D scanning. Scale bar, 500 μm. (**b**) Scanning electron micrograph of vertical comb actuators. Scale bar, 100 μm. Material is this figure is based on work by Piyawattanametha *et al.*[71]

Design and integration

As imaging systems have become increasingly miniaturized, optical and mechanical designs have grown increasingly intricate. Zemax and Code V are optical ray-tracing software programs that are commonly used for optical design and tolerance analysis. Computer-aided design programs such as SolidWorks and AutoCad can generate 3D models and technical drawings of mechanical configurations. We have found such software invaluable for designing complex imaging systems.

EMBODIMENTS

Fiber-optic epifluorescence, scanning confocal and two-photon imaging each has distinct sets of strengths and limitations[78] (Table 1). The latter two forms offer 3D optical sectioning, important for many applications, but sectioning is not always needed or desired. For example, *in vivo* epifluorescence microendoscopy readily allows viewing, by eye or with video-rate recordings, of red blood cell flow, without the need for laser sources or fast scanners[35,44]. Further, lack of sectioning may facilitate faster imaging speeds in some applications by aggregating fluorescence signals acquired simultaneously from adjacent tissue depths. The key advantage of two-photon imaging is robustness to scattering and increased penetration depths, but the high cost of an ultrashort-pulse laser is a distinct disadvantage. Nonetheless, when using epifluorescence or confocal modalities to image through more than ~50 μm of tissue, image contrast declines sharply with depth due to scattering. Additionally, these two modalities are more vulnerable to photobleaching and phototoxicity, which unlike in two-photon imaging occur not only at the focus but also in out-of-focus planes.

Epifluorescence imaging modalities

One-photon epifluorescence imaging can involve a compound GRIN microendoscope probe, a flexible fiber bundle or both. Unlike existing forms of either fiber-optic confocal or two-photon imaging, one-photon endoscopy and microendoscopy are currently the only fiber imaging varieties that enable images to be directly viewed by eye.

In the simplest form of one-photon FME (Fig. 4a), a conventional microscope is equipped with a GRIN endoscope probe ≤1 mm in diameter. The microscope objective directs illumination light into the probe and adjustment of the objective position provides a noninvasive focusing mechanism for altering the image plane in the tissue[35,36].

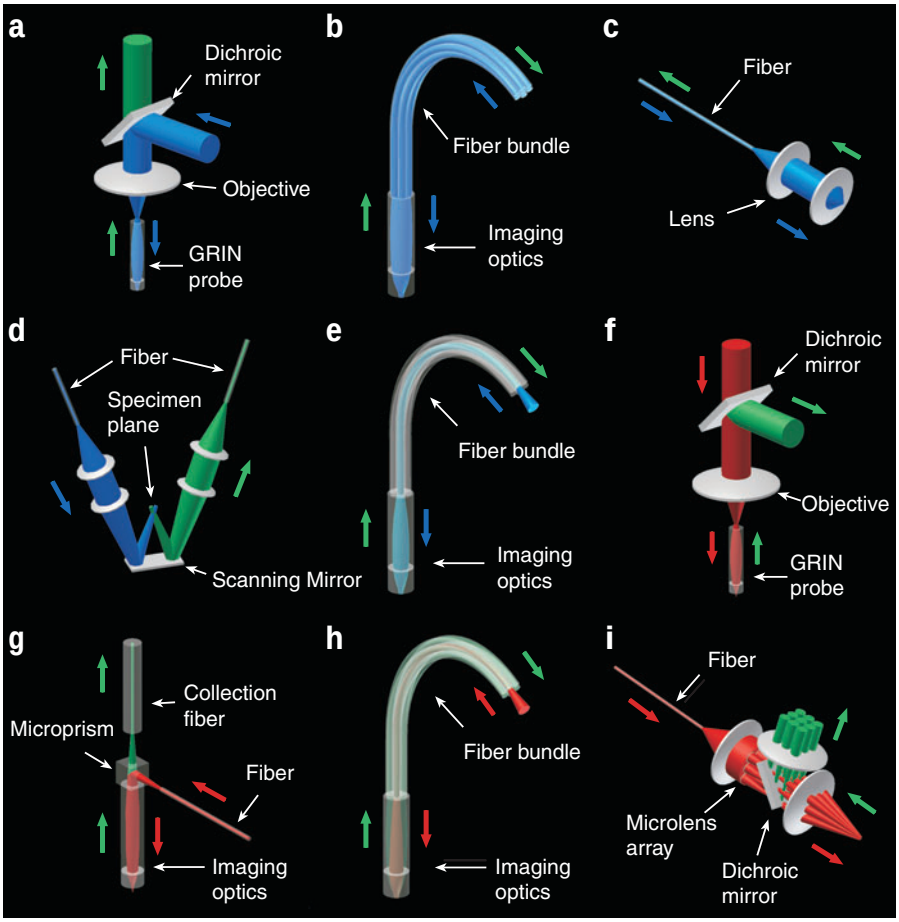

Figure 4 | Fiber-optic fluorescence imaging embodiments. (**a**) One-photon FME using a GRIN microendoscope probe. Visible illumination is coupled into the probe, which focuses the light onto the sample. Fluorescence returns through the probe. (**b**) One-photon epifluorescence imaging using a fiber bundle. Illumination travels through the fiber bundle to a small objective or GRIN lens, which focuses the light onto the sample. Fluorescence returns through the bundle. (**c**) Confocal imaging using SMF. The SMF delivers illumination to lenses that collimate and focus the light onto the specimen. The SMF core also serves as a pinhole for collecting in focus but rejecting out-of-focus fluorescence emissions. For microscopy, this embodiment generally relies on galvanometer scanning mirrors, which would be located between the fiber and lenses. For flexible endoscopy, the miniaturized distal scanning mechanisms are appropriate. (**d**) Dual-axis confocal microscopy. One SMF delivers excitation light and a second SMF, mounted at an angle with respect to the first, collects fluorescence from the overlapping region of the two fiber apertures. (**e**) Fiber bundle confocal imaging. Visible excitation light is scanned across a fiber bundle. A miniaturized objective or GRIN lens focuses the light onto the sample. Fluorescence returns through the probe and is routed to a pinhole detector. (**f**) Two-photon FME with a GRIN microendoscope probe. Ultrashort pulses are coupled into the probe, which focuses the light onto the sample. Fluorescence returns back through the probe and is routed to a photodetector. (**g**) Single-fiber two-photon imaging. Ultrashort pulses exiting a single fiber are scanned in 2D before entering a miniaturized objective or GRIN lens, which focuses the near-infrared excitation pulses onto the sample. A coated microprism can serve as a dichroic mirror. A large-core multimode fiber collects fluorescence. (**h**) Fiber bundle two-photon imaging. Ultrashort pulses are scanned across the proximal end of a fiber bundle. A miniature objective or GRIN lens focuses the light onto the sample. Fluorescence returns through the bundle to a detector. (**i**) Multifocal two-photon imaging. A single fiber delivers the excitation light to a collimating lens. A micro-lens array divides the beam into multiple 'beamlets', which are scanned in 2D and focused onto the sample. In all panels, blue represents visible fluorescence excitation light, red represents ultrashort-pulsed near-infrared light for two-photon excitation, and green represents visible fluorescence emission. Arrows show the directions of light propagation. Detectors and cameras are omitted. Scanners and dichroic mirrors are not shown except where explicitly labeled.

This approach has enabled imaging of neuronal activity and blood flow in deep brain regions of live rodents[2,35,79], but the use of short, rigid microendoscope probes coupled to a full-sized microscope restricts applications to immobilized specimens.

The use of fiber bundles alleviates this stipulation and provides mechanical flexibility while imaging in deep tissue[59] (Fig. 4b). Similar approaches have been used for reflectance imaging in freely moving cats[80]. With a bare fiber bundle, only objects in direct contact with the tip of the bundle are in focus, but addition of a miniature lens to the distal end of the bundle can add optical working distance. As with conventional epifluorescence microscopy, out-of-focus and scattered fluorescence photons reduce image contrast.

Confocal imaging modalities

Fiber-optic confocal imaging can involve one SMF, two SMFs for dual-axis imaging or a fiber bundle. SMFs are used in confocal microscopy for remote light delivery, but their main application is in flexible endoscopy. Miniaturized optics and compact distal scanning mechanisms, such as fiber-tip scanning[22,65] (Fig. 2e), fiber-objective lens scanning[20,24,67] (Fig. 2f) or MEMS mirror–based scanning (Figs. 2d and 3)[68,69], have enabled SMF-based confocal endoscopes with an outer diameter as small as 3.5 mm (Fig. 4c)[24]. Nonetheless, reduction of imaging and scanning optics to the millimeter scale nearly always compromises some combination of resolution, field of view and working distance. With confocal endoscopy based on one SMF (Fig. 4c), design pressures tend to center on the choice of high NA objective optics, which are a key determinant of image quality and fluorescence collection efficiency.

Dual-axis confocal imaging provides an alternate set of compromises, reducing ease of alignment and efficiency of fluorescence collection to gain longer optical working distance, immunity to off-axis aberrations, and good axial resolution using economical objective lenses. Two SMFs mounted at an angle to one another deliver light and collect fluorescence, respectively (Fig. 4d). Axial resolution is determined by the angle between the fibers and the transverse size of the illumination beam. Thus, two low-NA, long-working-distance objectives can provide an effective high-NA for axial sectioning, although the fluorescence collection NA remains low. A compact postobjective scanning

mechanism, such as a 2D tip-tilt mirror (Fig. 2d), offers broad fields of view up to ~500 μm[81–83]. To date, dual-axis imaging has been demonstrated in microscopy, but dual-axis endoscopy should emerge soon.

Fiber bundle confocal imaging facilitates miniaturization by use of conventional scanners proximal to the light source but reduces resolution through image pixilation (Fig. 4e). Many fiber bundle confocal designs also forgo a focusing mechanism to reduce size. For example, simply fusing a compound GRIN micro-lens onto the tip of a bundle enables handheld confocal FME probes with diameters as small as 300 μm[40,42]. Such probes and accompanying imaging systems are now commercially available. By comparison, fiber bundle confocal endoscopes with remotely controlled distal focusing and miniature objective lenses exist with outer diameters as small as 3 mm[30]. With either variety, a descanning pinhole rejects out-of-focus fluorescence to achieve optical sectioning. Scanning a line of excitation light across the bundle (Fig. 2b) boosts the image-acquisition rate, enabling video-rate imaging, although one must then use a descanning slit that does not reject out-of-focus light along the slit's linear dimension[25,30,31].

Two-photon fluorescence imaging modalities

For two-photon FME, a conventional two-photon microscope can be furnished with a GRIN microendoscope probe for insertion into tissue (Fig. 4f). As in one-photon FME, adjustment of the microscope objective position alters image focus. Although image frame rates have been lower (up to several Hz) than in one-photon FME, localized two-photon excitation provides inherent optical sectioning up to hundreds of micrometers from the tip of the endoscope probe. Two-photon FME has enabled *in vivo* imaging of individual neurons and blood vessels deep in the brain[35,37].

As with one-photon endoscopy, the combination of a short endoscope probe and a flexible fiber removes the requirement for specimens to be immobilized (Fig. 4g). A two-photon FME system based on a PBF for delivery of ultrashort pulses and a GRIN microendoscope probe has been created with an imaging head that is ~3.5 cm × 1.2 cm × 1.5 cm in size and 3.9 g in mass[38]. This device uses resonant fiber tip scanning[1], DC micromotor–based focusing and collection of fluorescence using a large-core multimode fiber. By comparison, fiber-optic two-photon microscopy based on a small microscope objective provides finer resolution and higher collection efficiency but does not allow the same degree of miniaturization[1].

For both flexibility and superior miniaturization, a fiber bundle based approach to two-photon FME has been realized (Fig. 4h)[39]. Because fluorescence excitation is localized to the focal spot, the descanning pinhole of confocal modalities is unnecessary, enabling whole-area detection in which fluorescence is collected across the entire bundle. Nonlinear distortion of the excitation pulses in each fiber (Box 1) currently limits fiber-bundle two-photon imaging to applications in surface tissue that do not require nanojoule energy pulses[39]. Unfortunately, arrays of hollow core PBF or LMA-PCF do not yet exist with sufficiently large numbers of pixels for imaging.

The combination of a single PBF for light delivery, a micro-lens array for generating multiple foci and a small 2D scanning mirror has enabled high-speed, handheld two-photon microscopy (Fig. 4i)[17,18]. Because multiple laser foci exist within the sample it is necessary to use a camera or multianode photomultiplier tube for signal detection. When the field of view is small and imaging is performed deep within tissue, scattering of fluorescence emissions can lead to cross talk between pixels and reduced contrast. To date, multifocal, two-photon imaging has been demonstrated for portable microscopy[17,18], but further miniaturization might enable endoscopy.

FUTURE DIRECTIONS

Fiber-optic fluorescence imaging will continue to benefit from progress in miniaturized and microfabricated components. There is also growing interest in other nonlinear optical modalities, such as second harmonic generation (SHG)[84] and Coherent Anti-Stokes Raman Scattering (CARS)[85], that provide inherent optical sectioning as in two-photon imaging but with intrinsic contrast generation mechanisms that do not require a dye label. Fiber-optic SHG and CARS imaging will benefit from the same trends towards miniaturization that are driving progress in fiber-optic fluorescence imaging.

Future fiber-optic systems will likely use microfabricated components in addition to scanning mirrors. Electrostatically actuated lenses are an alternative to MEMS mirrors for miniaturized scanning[86]. In addition, optical fibers and small lenses can be integrated by micromachining a v-groove or optical benches directly into a silicon wafer[68,87,88]. Optical fibers for light delivery and collection may eventually become unnecessary with the advent of integrated semiconductor laser sources and photodetectors[89]. Imaging systems in which all components are fabricated monolithically would provide a new degree of miniaturization, inherent alignment and potential for highly parallel imaging. Together, such advances will propel imaging applications that require both portability and a high degree of functionality.

ACKNOWLEDGMENTS

Our work on fiber-optic imaging is supported by grants to M.J.S from the Human Frontier Science Program, the US National Institute on Drug Abuse, the US National Institute of Neurological Disorders and Stroke, the US National Science Foundation, the US Office of Naval Research, the Arnold & Mabel Beckman Foundation and the David & Lucille Packard Foundation. B.A.F is a National Science Foundation Graduate Research Fellow. E.D.C. is a member of the Stanford Biotechnology Program. W.P. is an affiliate of the National Electronics and Computer Technology Center of Thailand. E.L.M.C. is supported in part by a Dean's Fellowship, Stanford School of Medicine. We thank R. Kristiansen of C. Fibre for providing images of photonic crystal fiber.

COMPETING INTERESTS STATEMENT

The authors declare that they have no competing financial interests.

Published online at http://www.nature.com/naturemethods/
Reprints and permissions information is available online at http://npg.nature.com/reprintsandpermissions/

1. Helmchen, F., Fee, M.S., Tank, D.W. & Denk, W. A miniature head-mounted two-photon microscope. high-resolution brain imaging in freely moving animals. *Neuron* **31**, 903–912 (2001).
2. Monfared, A. *et al. In vivo* imaging of mammalian cochlear blood flow using fluorescence microendoscopy. *Otol. Neurotol.* (in the press) .
3. Bashford, C.L., Barlow, C.H., Chance, B., Haselgrove, J. & Sorge, J. Optical measurements of oxygen delivery and consumption in gerbil cerebral cortex. *Am. J. Physiol.* **242**, C265–C271 (1982).
4. Chance, B., Cohen, P., Jobsis, F. & Schoener, B. Intracellular oxidation-reduction states *in vivo*. *Science* **137**, 499–508 (1962).
5. Mayevsky, A. & Chance, B. Intracellular oxidation-reduction state measured *in situ* by a multichannel fiber-optic surface fluorometer. *Science* **217**, 537–540 (1982).
6. Epstein, J.R. & Walt, D.R. Fluorescence-based fibre optic arrays: a universal platform for sensing. *Chem. Soc. Rev.* **32**, 203–214 (2003).
7. Yamaguchi, S. *et al.* View of a mouse clock gene ticking. *Nature* **409**, 684 (2001).
8. Bird, D. & Gu, M. Fibre-optic two-photon scanning fluorescence microscopy. *J. Microsc.* **208**, 35–48 (2002).
9. Ghiggino, K.P., Harris, M.R. & Spizzirri, P.G. Fluorescence lifetime measurements using a novel fiber-optic laser scanning confocal microscope. *Rev. Sci. Instrum.*

63, 2999–3002 (1992).
10. Dabbs, T. & Glass, M. Fiber optic confocal microscope: FOCON. *Appl. Opt.* **31**, 3030–3035 (1992).
11. Bird, D. & Gu, M. Compact two-photon fluorescence microscope based on a single-mode fiber coupler. *Opt. Lett.* **27**, 1031–1033 (2002).
12. Bird, D. & Gu, M. Resolution improvement in two-photon fluorescence microscopy with a single-mode fiber. *Appl. Opt.* **41**, 1852–1857 (2002).
13. Delaney, P.M., Harris, M.R. & King, R.G. Novel microscopy using fibre optic confocal imaging and its suitability for subsurface blood vessel imaging *in vivo*. *Clin. Exp. Pharmacol. Physiol.* **20**, 197–198 (1993).
14. Delaney, P.M., Harris, M.R. & King, R.G. Fiber-optic laser scanning confocal microscope suitable for fluorescence imaging. *Appl. Opt.* **33**, 573–577 (1994).
15. Delaney, P.M., King, R.G., Lambert, J.R. & Harris, M.R. Fibre optic confocal imaging (FOCI) for subsurface microscopy of the colon *in vivo*. *J. Anat.* **184**, 157–160 (1994).
16. Tai, S.P. *et al.* Two-photon fluorescence microscope with a hollow-core photonic crystal fiber. *Opt. Express* **12**, 6122–6128 (2004).
17. Kim, D., Kim, K.H., Yazdanfar, S. & So, P.T.C. Optical biopsy in high-speed handheld miniaturized multifocal multiphoton microscopy. *Proceedings of SPIE* **5700**, 14–22 (2005).
18. Kim, D., Kim, K.H., Yazdanfar, S. & So, P.T.C. High speed handheld multiphoton multifoci microscopy. *Proceedings of SPIE* **5323**, 267–272 (2004).
19. Carlson, K. *et al. In vivo* fiber-optic confocal reflectance microscope with an injection-molded miniature objective lens. *Appl. Opt.* **44**, 1792–1796 (2005).
20. Giniunas, L., Juskaitis, R. & Shatalin, S.V. Scanning fibre-optic microscope. *Electronics Lett.* **27**, 724–726 (1991).
21. Giniunas, L., Juskaitis, R. & Shatalin, S.V. Endoscope with optical sectioning capability. *Appl. Opt.* **32**, 2888–2890 (1993).
22. Kiesslich, R. *et al.* Confocal laser endoscopy for diagnosing intraepithelial neoplasias and colorectal cancer *in vivo*. *Gastroenterology* **127**, 706–713 (2004).
23. Liang, C., Sung, K.B., Richards-Kortum, R. & Descour, M.R. Design of a high-numerical aperture miniature microscope objective for an endoscopic fiber confocal reflectance microscope. *Appl. Opt.* **41**, 4603–4610 (2002).
24. Ota, T., Fukuyama, H., Ishihara, Y., Tanaka, H. & Takamatsu, T. *In situ* fluorescence imaging of organs through compact scanning head for confocal laser microscopy. *J. Biomed. Opt.* **10**, 1–4 (2005).
25. Rouse, A.R. & Gmitro, A.F. Multispectral imaging with a confocal microendoscope. *Opt. Lett.* **25**, 1708–1710 (2000).
26. Swindle, L.D., Thomas, S.G., Freeman, M. & Delaney, P.M. View of normal human skin *in vivo* as observed using fluorescent fiber-optic confocal microscopic imaging. *J. Invest. Dermatol.* **121**, 706–712 (2003).
27. Anikijenko, P. *et al. In vivo* detection of small subsurface melanomas in athymic mice using noninvasive fiber optic confocal imaging. *J. Invest. Dermatol.* **117**, 1442–1448 (2001).
28. Bussau, L.J. *et al.* Fibre optic confocal imaging (FOCI) of keratinocytes, blood vessels and nerves in hairless mouse skin *in vivo*. *J. Anat.* **192**, 187–194 (1998).
29. Papworth, G.D., Delaney, P.M., Bussau, L.J., Vo, L.T. & King, R.G. *In vivo* fibre optic confocal imaging of microvasculature and nerves in the rat vas deferens and colon. *J. Anat.* **192**, 489–495 (1998).
30. Rouse, A.R., Kano, A., Udovich, J.A., Kroto, S.M. & Gmitro, A.F. Design and demonstration of a miniature catheter for a confocal microendoscope. *Appl. Opt.* **43**, 5763–5771 (2004).
31. Sabharwal, Y.S., Rouse, A.R., Donaldson, K.A., Hopkins, M.F. & Gmitro, A.F. Slit-scanning confocal microendoscope for high-resolution *in vivo* imaging. *Appl. Opt.* **38**, 7133–7144 (1999).
32. McLaren, W., Anikijenko, P., Barkla, D., Delaney, T.P. & King, R. *In vivo* detection of experimental ulcerative colitis in rats using fiberoptic confocal imaging (FOCI). *Dig. Dis. Sci.* **46**, 2263–2276 (2001).
33. McLaren, W.J., Anikijenko, P., Thomas, S.G., Delaney, P.M. & King, R.G. *In vivo* detection of morphological and microvascular changes of the colon in association with colitis using fiberoptic confocal imaging (FOCI). *Dig. Dis. Sci.* **47**, 2424–2433 (2002).
34. Vo, L.T. *et al.* Autofluorescence of skin burns detected by fiber-optic confocal imaging: evidence that cool water treatment limits progressive thermal damage in anesthetized hairless mice. *J. Trauma* **51**, 98–104 (2001).
35. Jung, J.C., Mehta, A.D., Aksay, E., Stepnoski, R. & Schnitzer, M.J. *In vivo* mammalian brain imaging using one- and two-photon fluorescence microendoscopy. *J. Neurophysiol.* **92**, 3121–3133 (2004).
36. Jung, J.C. & Schnitzer, M.J. Multiphoton endoscopy. *Opt. Lett.* **28**, 902–904 (2003).
37. Levene, M.J., Dombeck, D.A., Kasischke, K.A., Molloy, R.P. & Webb, W.W. *In vivo* multiphoton microscopy of deep brain tissue. *J. Neurophysiol.* **91**, 1908–1912 (2004).
38. Flusberg, B.A., Jung, J.C., Cocker, E.D., Anderson, E.P. & Schnitzer, M.J. *In vivo* brain imaging using a portable 3.9 gram two-photon fluorescence microendoscope. *Opt. Lett.* **30**, 2272–2274 (2005).
39. Gobel, W., Kerr, J.N., Nimmerjahn, A. & Helmchen, F. Miniaturized two-photon microscope based on a flexible coherent fiber bundle and a gradient-index lens objective. *Opt. Lett.* **29**, 2521–2523 (2004).
40. Knittel, J., Schnieder, L., Buess, G., Messerschmidt, B. & Possner, T. Endoscope-compatible confocal microscope using a gradient index-lens system. *Opt. Commun.* **188**, 267–273 (2001).
41. D'Hallewin, M-A., Khatib, S.E., Leroux, A., Bezdetnaya, L. & Guillemin, F. Endoscopic confocal fluorescence microscopy of normal and tumor bearing rat bladder. *J. Urol.* **174**, 736–740 (2005).
42. Laemmel, E. *et al.* Fibered confocal fluorescence microscopy (Cell-viZio™) facilitates extended imaging in the field of microcirculation. A comparison with intravital microscopy. *J. Vasc. Res.* **41**, 400–411 (2004).
43. Bird, D. & Gu, M. Two-photon fluorescence endoscopy with a micro-optic scanning head. *Opt. Lett.* **28**, 1552–1554 (2003).
44. Mehta, A.D., Jung, J.C., Flusberg, B.A. & Schnitzer, M.J. Fiber optic *in vivo* imaging in the mammalian nervous system. *Curr. Opin. Neurobiol.* **14**, 617–628 (2004).
45. Saleh, B.E.A. & Teich, M.C. *Fundamentals of photonics* (John Wiley & Sons, Inc., New York, USA, 1991).
46. Harris, M.R. (US patent 5120953, 1992).
47. Fu, L., Gan, X. & Gu, M. use of a single-mode fiber coupler for second-harmonic-generation microscopy. *Opt. Lett.* **30**, 385–387 (2005).
48. Yariv, A. Three-dimensional pictorial transmission in optical fibers. *Appl. Phys. Lett.* **28**, 88–89 (1976).
49. Helmchen, F., Tank, D.W. & Denk, W. Enhanced two-photon excitation through optical fiber by single-mode propagation in a large core. *Appl. Opt.* **41**, 2930–2934 (2002).
50. Myaing, M.T., Urayama, J., Braun, A. & Norris, T.B. Nonlinear propagation of negatively chirped pulses: Maximizing the peak intensity at the output of a fiber probe. *Opt. Express* **7**, 210–214 (2000).
51. Ouzounov, D.G. *et al.* Delivery of nanojoule femtosecond pulses through large-core microstructured fibers. *Opt. Lett.* **27**, 1513–1515 (2002).
52. Knight, J.C. Photonic crystal fibres. *Nature* **424**, 847–851 (2003).
53. Gobel, W., Nimmerjahn, A. & Helmchen, F. Distortion-free delivery of nanojoule femtosecond pulses from a Ti:sapphire laser through a hollow-core photonic crystal fiber. *Opt. Lett.* **29**, 1285–1287 (2004).
54. Tai, S.-H., Chan, M.-C., Tsai, T.-H., Guol, S.-H., Chen, L.-J. & Sun, C.-K. Two-photon fluorescence microscope with a hollow-core photonic crystal fiber. *Proceedings of SPIE* **5691**, 146–152 (2005).
55. Treacy, E.B. Optical pulse compression with diffraction gratings. *IEEE J. Quantum Electron.* **QE-5**, 454–458 (1969).
56. Fork, R.L., Brito Cruz, C.H., Becker, P.C. & Shank, C.V. Compression of optical pulses to six femtoseconds by using cubic phase compensation. *Opt. Lett.* **12**, 483–485 (1987).
57. Ye, J.Y. *et al*. Development of a double-clad photonic-crystal-fiber based scanning microscope. *Proceedings of SPIE* **5700**, 23–27 (2005).
58. Fu, L., Gan, X. & Gu, M. Nonlinear optical microscopy based on double-clad photonic crystal fibers. *Opt. Express* **13**, 5528–5534 (2005).
59. Hirano, M., Yamashita, Y. & Miyakawa, A. *In vivo* visualization of hippocampal cells and dynamics of Ca2+ concentration during anoxia: feasibility of a fiber-optic plate microscope system for *in vivo* experiments. *Brain Res.* **732**, 61–68 (1996).
60. Lane, P.M., Dlugan, A.L.P., Richards-Kortum, R. & MacAulay, C.E. Fiber-optic confocal microscopy using a spatial light modulator. *Opt. Lett.* **25**, 1780–1782 (2000).
61. Gmitro, A.F. & Aziz, D. Confocal microscopy through a fiber-optic imaging bundle. *Opt. Lett.* **18**, 565–567 (1993).
62. Lin, C.H. & Webb, R.H. Fiber-coupled multiplexed confocal microscope. *Opt. Lett.* **25**, 954–957 (2000).
63. Dong, C.Y., Koenig, K. & So P. Characterizing point spread functions of two-photon fluorescence microscopy in turbid medium *J. Biomed. Opt.* **8**, 450–459 (2003).
64. Seibel, E.J. & Smithwick, Q.Y. Unique features of optical scanning, single fiber endoscopy. *Lasers Surg. Med.* **30**, 177–183 (2002).
65. Delaney, P.M. & Harris, M.R. In *Handbook of Biological Confocal Microscopy* (ed. Pawley, J. B.) 515–523 (Plenum Press, New York, 1995).
66. Harris, M.R. (UK patent W09904301, 1999).
67. Dickensheets, D. & Kino, G.S. Scanned optical fiber confocal microscope. *Proceedings of SPIE* **2184**, 39–47 (1994).
68. Dickensheets, D.L. & Kino, G.S. Micromachined scanning confocal optical microscope. *Opt. Lett.* **21**, 764–766 (1996).
69. Hofmann, U., Muehlmann, S., Witt, M., Dorschel, K., Schutz, R. & Wagner, B. Electrostatically driven micromirrors for a miniaturized confocal laser scanning microscope. *Proceedings of SPIE* **3878**, 29–38 (1999).
70. Piyawattanametha, W., Toshiyoshi, H., LaCosse, J. & Wu, M.C. Surface

micromachined confocal scanning optical microscope. In *Technical Digest Series of Conference on Lasers and Electro-Optics (CLEO)*, 447–448 (San Francisco, 2000).
71. Piyawattanametha, W., Patterson, P., Hah, D., Toshiyoshi, H. & Wu, M.C. A 2D scanner by surface and bulk micromachined angular vertical comb actuators. In *IEEE/LEOS International Conference on Optical MEMS,* 93–94 (Waikoloa, Hawaii, 2003).
72. Schenk, H. *et al.* Large deflection micromechanical scanning mirrors for linear scans and pattern generation. *J. Select. Topics in Quantum Electronics* **6**, 715–722 (2000).
73. Lee, D. Solgaard, O. T. Two-axis gimbaled microscanner in double SOI layers actuated by self-aligned vertical electrostatic combdrive. In *Proceedings of the Solid-State Sensor and Actuator Workshop,* 352–355 (Hilton Head, South Carolina, 2004).
74. Rector, D.M., Rogers, R.F. & George, J.S. A focusing image probe for assessing neural activity *in vivo*. *J. Neurosci. Methods* **91**, 135–145 (1999).
75. Kuiper, S. & Hendriks, B.H.W. Variable-focus liquid lens for miniature cameras. *Appl. Phys. Lett.* **85**, 1128–1130 (2004).
76. Berge, B. & Peseux, J. Variable focal lens controlled by an external voltage: an application of electrowetting. *Eur. Phys. J. E* **3**, 159–163 (2000).
77. Kuiper, S., Hendriks, B.H.W., Hayes, R.A., Feenstra, B.J. & Baken, J.M.E. Electrowetting-based optics. *Proceedings of SPIE* **5908**, 5908OR-1–5908OR-7 (2005).
78. George, M. Optical methods and sensors for *in situ* histology in surgery and endoscopy. *Min. Invas. Ther. & Allied. Technol.* **13**, 95–104 (2004).
79. Fisher, J.A.N., Civillico, E.F., Contreras, D. & Yodh, A.G. *In vivo* fluorescence microscopy of neuronal activity in three dimensions by use of voltage-sensitive dyes. *Opt. Lett.* **29**, 71–73 (2004).
80. Poe, G.R., Rector, D.M. & Harper, R.M. Hippocampal reflected optical patterns during sleep and waking states in the freely behaving cat. *J. Neurosci.* **14**, 2933–2942 (1994).
81. Wang, T.D., Contag, C.H., Mandella, M.J., Chan, N.Y. & Kino, G.S. Dual-axes confocal microscopy with post-objective scanning and low-coherence heterodyne detection. *Opt. Lett.* **28**, 1915–1917 (2003).
82. Wang, T.D., Contag, C.H., Mandella, M.J., Chan, N.Y. & Kino, G.S. Confocal fluorescence microscope with dual-axis architecture and biaxial postobjective scanning. *J. Biomed. Opt.* **9**, 735–742 (2004).
83. Wang, T.D., Mandella, M.J., Contag, C.H. & Kino, G.S. Dual-axis confocal microscope for high resolution *in vivo* imaging. *Opt. Lett.* **28**, 414–416 (2003).
84. Brown, E. *et al.* Dynamic imaging of collagen and its modulation in tumors *in vivo* using second-harmonic generation. *Nat. Med.* **9**, 796–800 (2003).
85. Cheng, J.-X., & Xie, X.S. Coherent anti-Stokes Raman scattering microscopy: instrumentation theory, and applications. J. Phys. Chem. B 108, 827–840 (2004).
86. Kwon, S. & Lee, L.P. Micromachined transmissive scanning confocal microscope. *Opt. Lett.* **29**, 706–708 (2004).
87. Lee, K.-N., Jang, Y.-H., Choi, J. & Kim, H. Silicon scanning mirror with 54.74° slanted reflective surface for fluorescence scanning system. *Proceedings of SPIE* **5641**, 56–66 (2004).
88. Sheard, S., Suhara, T. & Nishihara, H. Integrated-optic implementation of a confocal scanning optical microscope. *Journal of Lightwave Technology* **11**, 1400–1403 (1993).
89. Thrush, E. *et al.* Integrated semiconductor verticle-cavity surface-emitting lasers and PIN photodetectors for biomedical fluorescence sensing. *IEEE J. Quantum Electron.* **40**, 491–498 (2004).
90. McConnell, G. & Riis, E. Photonic crystal fibre enables short-wavelength two-photon laser scanning fluorescence microscopy with fura-2. *Phys. Med. Biol.* **49**, 4757–4763 (2004).
91. McConnell, G. & Riis, E. Two-photon laser scanning fluorescence microscopy using photonic crystal fiber. *J. Biomed. Opt.* **9**, 922–927 (2004).